UiO : University of Oslo

Ole Marius Hoel Rindal

Software Beamforming in Medical Ultrasound Imaging - a blessing and a curse

Thesis submitted for the degree of Philosophiae Doctor

Department of Informatics
The Faculty of Mathematics and Natural Sciences

2019

Series of dissertations submitted to the
Faculty of Mathematics and Natural Sciences, University of Oslo
No. 2198

ISSN 1501-7710

Cover: Hanne Baadsgaard Utigard.
Print production: Reprosentralen, University of Oslo.

The highest activity a human being can attain is learning for understanding, because to understand is to be free.
- Baruch Spinoza

Acknowledgement

This PhD is not a work done in solitude. I have greatly benefited from cooperation with people smarter than myself. Working together with Alfonso Rodriquez-Molares has been a joy. I am quite proud of the insight we have gained in adaptive beamforming and especially the development of the USTB where you have been an inspiring ideal.

Professor Andreas Austeng, my supervisor, should be the role model for all PhD supervisors. Andreas is genuinely interested in your academic work, but first and foremost seems to care about you as a person. He always has time for a question or a discussion. The other members of the research group on Digital Signal Processing and Image Analysis(DSB) at the University of Oslo have provided an excellent creative, friendly, and inspiring working environment. I want to thank the professors in our research group, Sverre, Fritz, Roy, and Anne, for support and fruitful discussions. Also, I should especially thank the people fortunate enough, open for debate, to share an office with me for persevering discussions on topics not always relevant to our actual work.

I am also very grateful for Professor Muyinatu Lediju Bell, director of the Photoacoustic and Ultrasonic Systems Engineering (PULSE) lab at the Johns Hopkins University. She quite spontaneously accepted my request to visit her lab for several months, after a lunch discussion at the IUS conference in 2017. The PULSE lab provided a very friendly, motivating, and inspiring work environment provided by the members of the time Josh, Derek, Arun, and Michelle.

I want to thank family and friends for their support, and for actually appearing interested when I am describing what my research is on. My wife, Tuva, deserves my deepest gratitude. Tuva has, after some years of training, developed and excellent image metric and usually recognizes what images “my suggested method” has produced. She almost always agrees that my results are superior to the comparison. I am very grateful for her love and support for everything I do. Tuva makes sure I have a social life, even when the oversized workload makes me shut down my social abilities. Kari Louise, our daughter, is an unstoppable source of joy. An unproductive day is transformed into the most productive day after spending one minute together with you. I look forward to everything you will bring to my life.

Ole Marius Hoel Rindal
Oslo, June 2019

Abstract

Medical ultrasound (US) imaging is a non-invasive imaging modality. Smaller and cheaper US systems make US imaging available to more people, leading to a democratization of medical US imaging. The improvements of general processing hardware allow the reconstruction of US images to be done in software. These implementations are known as software beamforming and provide access to the US data earlier in the processing chain. Adaptive beamforming exploits the early access to the full US data with algorithms adapting the processing to the data. Adaptive beamforming claims improved image quality. The improved image will potentially result in an improved diagnosis.

Adaptive beamformers have seen enormous popularity in the research community with exponential growth in the number of papers published. However, the complexity of the algorithms makes them hard to re-implement, making a thorough comparison of the algorithms difficult. The UltraSound ToolBox (USTB https://www.USTB.no) is an open source processing framework facilitating the comparison of imaging techniques and the dissemination of research results. The USTB, including the implementation of several state-of-the-art adaptive beamformers, has partly been developed in this thesis and used to produce most of the results presented. The results show that some of the contrast improvements reported in the literature turn out to be from secondary effects of adaptive processing. More specifically, we show that many state-of-the-art algorithms alter the dynamic range. These dynamic range alterations are invalidating the conventional contrast metrics. Said differently; many adaptive algorithms are so flexible that they instead of improving the image quality are merely optimizing the metrics used to evaluate the image quality. We suggest a dynamic range test, compromising data, and code, to assess whether an algorithm alters the dynamic range. A thorough review of the contrast metrics used in US imaging shows there is no consensus on the metrics used in the research literature. Therefore, our introduction of the generalized contrast to noise ratio (GCNR) is essential since this is a contrast metric immune to dynamic range alterations. The GCNR is a remedy for the *curse* of the metric breaking abilities of software beamforming.

Software beamforming also has its *blessings*. The flexible implementations made possible by software beamforming does lead to improved image quality. The improved resolution of the minimum variance adaptive beamformer does lead to enhanced visualization of the interventricular septum in the human heart. The ability to do beamforming in software allows the implementation of the full reconstruction chain from raw data to the final rendered images on an iPhone.

As well as the results presented in the published papers, this thesis does a thorough review of the software beamforming processing chain as implemented in the USTB.

List of Papers

Paper I

Rodriguez-Molares*, A., Rindal*, O. M. H., Bernard, O., Nair, A., Lediju Bell, M. A., Liebgott, H., Austeng, A., and Løvstakken, L. 2017 "The Ultra-Sound ToolBox". *IEEE International Ultrasonics Symposium, IUS:* 1–4. doi: 10.1109/ULTSYM.2017.8092389

Paper II

Rindal, O. M. H., Rodriguez-Molares, A., and Austeng, A. 2018. "A simple, artifact-free, virtual source model". *IEEE International Ultrasonics Symposium, IUS*: 1–4. doi:10.1109/ULTSYM.2018.8579944

Paper III

Palmer*, C. L. and Rindal*, O. M. H. 2019. "Wireless, Real-Time Plane-Wave Coherent Compounding on an iPhone - a feasibility study". *IEEE Transactions on Ultrasonics, Ferroelectrics, and Frequency Control* (PP): 1–11. doi: 10.1109/TUFFC.2019.2914555

Paper IV

Rindal, O. M. H. and Austeng, A. 2016. "Double Adaptive Plane-Wave Imaging". *IEEE International Ultrasonics Symposium, IUS*: 1–4. doi:10.1109/ULTSYM.2016.7728906

Paper V

Prieur, F., Rindal, O. M. H., and Austeng, A. 2018. "Signal Coherence and Image Amplitude With the Filtered Delay Multiply and Sum Beamformer". *IEEE Transactions on Ultrasonics, Ferroelectrics, and Frequency Control* 65 (7): 1133–1140. doi:10.1109/TUFFC.2018.2831789

Paper VI

Rindal, O. M. H., Rodriguez-Molares, A., and Austeng, A. 2017. "The Dark Region Artifact in Adaptive Ultrasound Beamforming". *IEEE International Ultrasonics Symposium, IUS*: 1–4. doi:10.1109/ULTSYM.2017.8092255

Paper VII

Rindal, O. M. H., Austeng, A., Fatemi, A., and Rodriguez-Molares, A. 2019. "The Effect of Dynamic Range Alterations in the Estimation of Contrast". *IEEE Transactions on Ultrasonics, Ferroelectrics, and Frequency Control* PP:1–11. doi:10.1109/TUFFC.2019.2911267

Paper VIII

Hverven, S. M., Rindal, O. M. H., Rodriguez-Molares, A., and Austeng, A. 2017b. "The Influence of Speckle Statistics on Contrast Metrics in Ultrasound Imaging". *IEEE International Ultrasonics Symposium, IUS*: 1–4. doi:10.1109/ULTSYM.2017.8091875

Paper IX

Rodriguez-Molares, A., Rindal, O. M. H., D'hooge, J., Måsøy, S.-E., Austeng, A., Lediju Bell, M. A., and Torp, H. 2019. "The Generalized Contrast-to-Noise ratio". *Prepared for submission to IEEE Transactions on Ultrasonics, Ferroelectrics, and Frequency Control*: 1–12

Paper X

Rindal, O. M. H., Aakhus, S., Holm, S., and Austeng, A. 2017. "Hypothesis of Improved Visualization of Microstructures in the Interventricular Septum with Ultrasound and Adaptive Beamforming". *Ultrasound in Medicine and Biology* 43 (10): 2494–2499. doi:10.1016/j.ultrasmedbio.2017.05.023

*These authors are shared first authors with equal contributions.

Related Publications

Paper XI

Wiacek, A., Rindal, O. M. H., Falomo, E., Myers, K., Fabrega-Foster, K., Harvey, S., and Bell, M. A. L. 2018b. "Robust Short-Lag Spatial Coherence Imaging of Breast Ultrasound Data: Initial Clinical Results". *IEEE Transactions on Ultrasonics, Ferroelectrics, and Frequency Control* 66 (3): 527–540. doi:10.1109/TUFFC.2018.2883427

Paper XII

Wiacek, A., Falomo, E., Myers, K., Rindal, O. M. H., Fabrega-foster, K., Harvey, S., and Bell, M. A. L. 2018a. "Clinical Feasibility of Coherence-Based Beamforming to Distinguish Solid from Fluid Hypoechoic Breast Masses". *IEEE International Ultrasonics Symposium, IUS*: 1–4. doi:10.1109/ULTSYM.2018.8579846

Paper XIII

Bernard, O., Hansen, H. H. G., Kruizinga, P., Mc, E., Ricci, S., Rindal, O. M. H., Rodriguez-molares, A., Stuart, M. B., and Dos Santos, P. F. V. 2018. "The Ultrasound File Format (UFF) - First draft". *IEEE International Ultrasonics Symposium, IUS*. doi:10.1109/ULTSYM.2018.8579642

Paper XIV

Rodriguez-Molares, A., Rindal, O. M. H., D'hooge, J., Måsøy, S.-E., Austeng, A., and Torp, H. 2018. "The Generalized Contrast-to-Noise Ratio". *IEEE International Ultrasonics Symposium, IUS*, no. 6: 1–4. doi:10.1109/ULTSYM.2018.8580101

Paper XV

Hverven, S., Rindal, O. M. H., Hunter, A., and Austeng, A. 2017a. "Point scatterer enhancement in ultrasound by wavelet coefficient shrinkage". In *IEEE International Ultrasonics Symposium, IUS*, 1–4. doi:10.1109/ULTSYM.2017.8091972

Paper XVI

Prieur, F., Rindal, O. M. H., Holm, S., and Austeng, A. "Influence of the Delay-Multiply-And-Sum beamformer on the ultrasound image amplitude". *IEEE International Ultrasonics Symposium, IUS*: 1–4. doi:10.1109/ULTSYM.2017.8092637

Paper XVII

Rindal, O. M. H., Austeng, A., Torp, H., Holm, S., and Rodriguez-Molares, A. 2016. "The dynamic range of adaptive beamformers". *IEEE International Ultrasonics Symposium, IUS*, no. 1: 1–4. doi:10.1109/ULTSYM.2016.7728717

Paper XVIII

Palmer, C. L., Rindal, O. M. H., Holm, S., and Austeng, A. 2016. "Realtime plane-wave software beamforming with an iPhone". *IEEE International Ultrasonics Symposium, IUS*: 1–4. doi:10.1109/ULTSYM.2016.7728408

Paper XIX

Rindal, O. M. H., Åsen, J. P., Holm, S., and Austeng, A. 2014. "Understanding Contrast Improvements from Capon Beamforming". *IEEE International Ultrasonics Symposium, IUS*, no. 1: 1694–1697. doi:10.1109/ULTSYM.2014.0420

Contents

Chapter 1

Introduction

The possibility to do medical ultrasound image reconstruction in software, known as software beamforming, has revolutionized the flexibility of the methods used to create an ultrasound image. Software beamforming is possible due to the improvements in the processing power of available hardware, especially in GPUs (Graphical Processing Units). GPUs allow the latest high-end medical ultrasound systems to utilize software beamforming. Within the research field, software beamforming has, for some time, received increased attention, especially within the more specific topic of adaptive beamforming. According to the Scopus database (Scopus 2018), the number of publications on adaptive beamforming in ultrasound has doubled in the last five years, as shown in Figure 1.1. Many of the published papers are claiming unprecedented improvements of the image quality, reporting contrast improvements of 78% (Nguyen and Prager 2018), 81% (Zhao et al. 2017), 85% (Zhuang, Rohling, and Abolmaesumi 2018), 91% (Shin and Huang 2017), 110% (Ozkan, Vishnevsky, and Goksel 2018) and 183% (Szasz, Basarab, and Kouamé 2016a) with respect to the conventional non-adaptive delay-and-sum algorithm. Such unprecedented improvements need to be thoroughly examined, raising some relevant research questions.

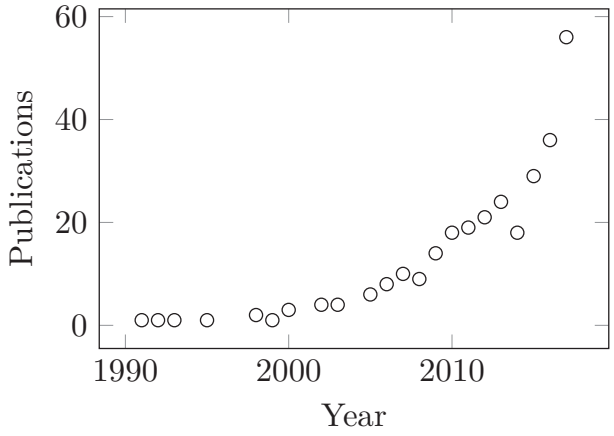

Figure 1.1: Number of publications in (Scopus 2018) presenting adaptive beamforming techniques in ultrasound. Credits to Alfonso Rodriguez-Molares for creating this figure intended for **Paper VII**.

1.1 Research questions

- Can beamforming implemented in software, in comparison to in hardware, improve the image quality of medical ultrasound images?
- Is there a fair and thorough comparison between adaptive beamforming algorithms in the research literature?
- Can adaptive beamforming introduce unwanted artifacts?
- Is there a consensus on metrics used to evaluate image quality in medical ultrasound imaging?
- Is adaptive beamforming clinically relevant?

1.2 Claims

With a foundation in the research questions above, this thesis explores various aspects of the medical ultrasound processing chain, from a software beamforming perspective, with the overall aim of improving the quality of the ultrasound images. Software beamforming is a *blessing* for the image quality since it provides access to the raw data early in the processing chain. Early access to the data means that it can be better exploited in the image reconstruction through, for example, adaptive beamforming. Many adaptive methods are compared and evaluated thoroughly in this thesis, exploring some of the benefits. Perhaps the main benefit of software beamforming is that image reconstruction can be implemented on general processing devices. We demonstrate that iPhones have the processing power to implement the full ultrasound software processing chain. However, software beamforming can also be considered a *curse*. A curse since the flexibility leads to algorithms that invalidate the metrics used to evaluate the image quality quantitatively. Much of this thesis is, therefore, spent evaluating the effects modern beamformers have on the ultrasound images. With an emphasis on how adaptive beamformers influences, and actually invalidates the conventional contrast metrics. An improved contrast metric, the Generalized Contrast-to-Noise Ratio, which is immune to some of the unwanted effects, is suggested. Clinical relevance is hypothesized through an investigation on how the improved resolution of one adaptive beamformer, Capon's minimum variance, improves the visualization of the interventricular septum in the heart.

1.3 Scope

The scope of the published work in this thesis is within the medical ultrasound processing chain. The publications are ranging from the fundamental delay calculations of the *time of flight* of ultrasound signals to the evaluation of contrast metrics. A graphical illustration of the major parts of the medical ultrasound processing chain, from a software perspective, is shown in Figure 1.2.

The figure highlights which part of the processing chain the publications in this thesis relate.

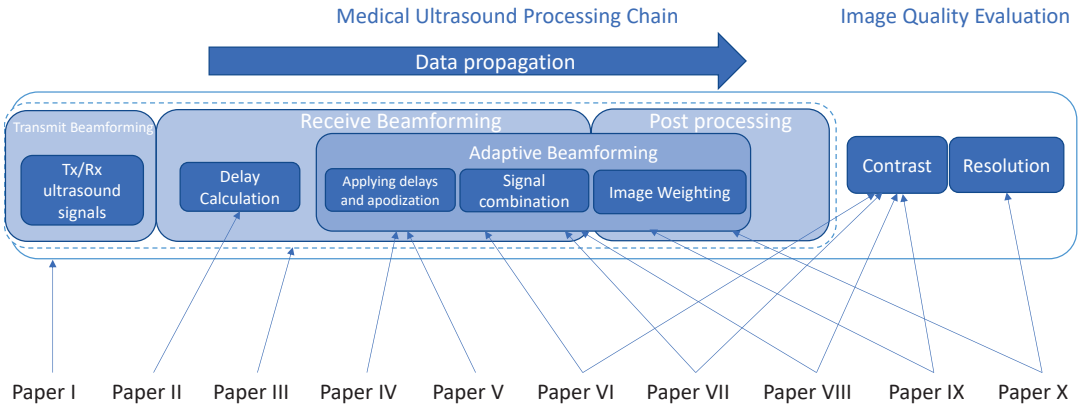

Figure 1.2: Graphical illustration of the software beamforming processing chain, also illustrating which area of the processing chain the publications in this thesis relate.

1.4 Thesis outline

The background chapter, **Chapter 2**, briefly presents the reader to the ultrasound processing chain from a software beamforming perspective as well as tying together the published papers. **Chapter 3** is a summary of the publications, while **Chapter 4** is a discussion based on the results presented in the publications, and **Chapter 5** presents some concluding remarks and some suggestion for further studies. **Paper I** presents an open source framework, the UltraSound ToolBox, for processing of ultrasound signals, to facilitate the comparison of imaging techniques and the dissemination of research results. **Paper II** presents a novel delay model for retrospective and multiple line acquisition beamforming, removing an unwanted artifact created by the conventional delay model. **Paper III** shows one of the major benefits of software beamforming; that the ultrasound processing chain, from raw channel data to final rendered image, can be implemented on an off the shelf device such as an iPad or iPhone. **Paper IV** shows the flexibility of software beamforming, allowing a *double adaptive* beamformer first applying adaptive weights over the receive channels, followed by an adaptive weighting in the coherent compounding of plane-wave images. **Paper V** does a thorough statistical analysis of a popular adaptive beamforming technique, the filtered delay multiply and sum, and shows that this beamformer is actually dependent on the coherence of the signal. **Paper VI** identifies an unwanted artifact present in many adaptive beamformers and coins the term *dark region artifact*. **Paper VII** shows that some of the claimed benefits of many adaptive beamformers, increased contrast, is highly correlated with an alternation of the dynamic range. It also shows that this dynamic range alteration means that some

of the adaptive beamformers are invalidating the conventional contrast metrics, and calls for an improved contrast metric immune to dynamic range alterations. The paper also introduces a *dynamic range test* compromising data and code to test whether a beamformer is alternating the dynamic range. **Paper VIII** shows that many adaptive beamformers alter the statistical distributions of speckle and noise and discuss how this influences the conventional contrast metrics. **Paper IX** is an answer to the call for an improved contrast metrics in paper VII, and presents the generalized contrast to noise ratio (GCNR), a contrast metric immune to dynamic range alterations and alternated speckle statistics. The GCNR is a quantitative measure of contrast indicating the proportion of pixels inside a cyst correctly classified. **Paper X** presents an in-vivo study of the adaptive minimum variance beamformer, hypothesizing how the improved resolution improves the visualization of the interventricular septum in the heart.

Chapter 2

Scientific Background: Software Beamforming Methodology

2.1 A brief history of medical ultrasound imaging

Prototype systems

According to (Szabo 2013) ”the imaginative leap to” ultrasound imaging came with an ultrasound image of the brain. The image was created by the Austrian psychiatrist and neurologist Dr Karl Dussik in 1942. During the pioneering work done in the 1940s and 1950s most of the systems must be considered research prototypes. Worth mentioning are the systems created by Dr. John J. Wild, who modified radar equipment to produce ultrasound images (Szabo 2013). As well as the ”somascope”, an immersion water tank ultrasound system, created by Douglass Howry and Joseph Holmes (Szabo 2013). A full immersion into a water thank must have been an interesting experience for, hopefully volunteering, patients.

The pioneering work from Inge Edler and Carl Hellmuth Hertz on echocardiography, done at the Lund University in Sweden, also needs to be credited. Through Hertz's contacts at Siemens (Munich, Germany) they got hold of a modified Siemens reflectoscope, originally created to do material testing (Siemens Healthineers 2019). They quickly adapted the reflectoscope and applied it to obtain echoes moving synchronously with the heart. The first ultrasound image of a beating heart credited Edler and Hertz was taken on October 1st, 1953. The further development of medical ultrasound scanners accompanied the developments of microelectronics, primarily the breakthrough of integrated circuits and transistors in the late 1940s and 1950s (Szabo 2013). The improvements in electronics allowed a shift from prototype systems to commercially available systems.

Commercial systems

The first real-time mechanical commercial scanner, the Vidoson from Siemens shown in Figure 2.1, became available in 1964. This scanner quickly became a standard component of assessing pregnant women (Soni, Arntfield, and Kory 2014). Further improvements of the image quality were perhaps, first and foremost, driven by improvements of the transducer arrays such as the introduction of a 16-channel phased array, the Thaumascan, developed by Von Ramm and Thurstone from Duke University in 1975.

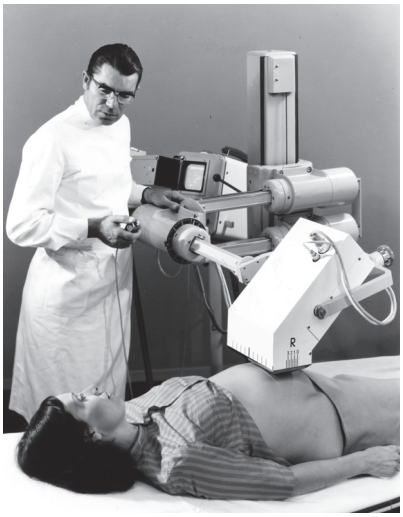

Figure 2.1: The Siemens Vidoson, press image from Siemens AG, all rights reserved © www.siemens.com/press.

Digital systems

Early array systems used analog delay lines to apply the delays to the received signals. However, in the 1990s more powerful microprocessors as well as low-cost analog to digital converters lead the way to replace the complex analog circuitry with digital beamformers. Digital implementations allowed the discovery and development of tissue harmonic imaging which, in some cases, provide superior contrast and detail (Szabo 2013).

Hand-held systems

The introduction of digital beamformers and general miniaturization of sophisticated electronics paved the way for hand-held systems, now provided by all major ultrasound manufacturers. An exciting development is the introduction of capacitive micromachined ultrasonic transducer (CMUT). CMUT can be printed in silicon together with the electronics to process the signals. The flexibility of CMUT makes a recent manufacturer (Butterfly Technologies, Guildford, CT, USA) claim that one probe can provide ”full body ultrasound”. The images are reconstructed in specialized electronics in the probe, while an iPhone is used to display the final images. The ability to do large scale production of CMUT transducers on the same ship as the processing, allows Butterfly to sell their hand-held systems at a very low price. Cheaper and more accessible ultrasound systems are aiding in the democratization of ultrasound imaging (McNeil Jr. 2019).

Software systems

Today, we are at the brink of what can be claimed is another revolution to the ultrasound processing chain: software beamforming. High-end medical

ultrasound systems are now utilizing the improvements in the processing power of general hardware and have incorporated software beamforming. To the author's knowledge, only two clinical medical ultrasound vendors utilize software beamforming today; namely the GE Vingmed Ultrasound Vivid systems using the cSound software based beamforming reconstruction platform (Kulina et al. 2016), and the Supersonic Imagine Aixplorer systems (SuperSonic Imagine 2019). However, extensive publications and many research ultrasound systems are doing software beamforming (Boni et al. 2018) – but only recently has it been brought to the clinic.

2.1.1 The motivation behind the UltraSound ToolBox

The flexibility of software beamforming provides unprecedented freedom when creating medical ultrasound images. This can be viewed as a *blessing* for the image quality, but a *curse* to the research community. A *curse* since the comparison of methods and research results are becoming more and more challenging with more complex methods published in the literature. The growing number of complex methods makes it hard to make a fair comparison between methods since the re-implementation of a method can be quite challenging. There is no guarantee that the re-implemented method performs as well as the original. To remedy this curse we presented, in **Paper I** the UltraSound ToolBox (USTB)[1] which is

> a processing framework for ultrasound signals. USTB aims to facilitate the comparison of imaging techniques and the dissemination of research results. It fills the void of tools for algorithm sharing and verification, and enables a solid assessment of the correctness and relevance of new approaches. It also aims to boost research productivity by cutting down implementation time and code maintenance. USTB is a MATLAB toolbox for processing 2D and 3D ultrasound data, supporting both MATLAB and C++ implementations. Channel data from any origin, simulated and experimental, and using any kind of sequence, e.g. synthetic transmit aperture imaging (STAI) or coherent plane-wave compounding (CPWC), can be processed with USTB.

Most of the work in this thesis was implemented using USTB. The data and implementations to reproduce the results in the publications are presented through www.USTB.no. More specifically;

Paper II at http://www.ustb.no/publications/paper_II,

Paper V at http://www.ustb.no/publications/paper_V,

Paper VI at http://www.ustb.no/publications/paper_VI,

Paper VII at http://www.ustb.no/publications/paper_VII.

[1] Alfonso Rodriquez-Molares deserves credits for most of the heavy lifting in the development of USTB.

In the current chapter, the medical ultrasound processing chain will be presented, from a software beamforming point of view, as well as pointing to the published work in this thesis where suitable. USTB is used to generate all examples. First, however, we will have a brief look at the physics behind medical ultrasound imaging.

2.2 The physics behind an ultrasound image

Ultrasound waves are longitudinal pressure waves that, by definition, are above the hearable range, meaning higher than ≈ 20 kHz. Medical ultrasound imaging is most often done using frequencies in the range of 2 to 18 MHz. Very shallow imaging, for example, imaging of small animals, is done using higher frequency probes up to ≈ 30 MHz. Higher frequency results in lower penetration depth because of the frequency-dependent attenuation of tissue. The benefit of higher frequency is improved resolution. Thus, ultrasound imaging results in a trade-off between penetration depth and resolution.

The wave equation describes the propagation of a wave. The lossless wave equation is, see e.g. (Holm 2019)

$$\Delta^2 u - \frac{1}{c^2}\frac{\partial^2 u}{\partial t^2} = \frac{\partial^2 u}{\partial x} + \frac{\partial^2 u}{\partial y} + \frac{\partial^2 u}{\partial z} - \frac{1}{c^2}\frac{\partial^2 u}{\partial t^2} = 0 \tag{2.1}$$

where Δ is the Laplacian operator, c is the speed of sound, x, y, z is the spatial coordinates, t is time, u is the displacement vector. The displacement vector u can also be replaced with the scalar pressure p.

The wave equation comes in many adaptations. One of them is the viscous wave equation which includes a term to model the frequency-dependent attenuation, see e.g. (Holm 2019)

$$\Delta^2 u - \frac{1}{c^2}\frac{\partial^2 u}{\partial t^2} + \tau c^2 \frac{\partial}{\partial t}\Delta^2 u = 0. \tag{2.2}$$

Here $\tau = \frac{\eta}{E}$, with E being the elastic modulus and η the viscosity. The frequency dependence of the absorption can be derived from the last term. The frequency-dependent absorption results in limitations on which frequency can be used to image deeper parts and organs in the body.

The high-frequency wave transmitted into the body will propagate according to the wave equation as long as the medium has similar acoustic properties. If the properties change, a part of the wave will be reflected, while another part will continue to propagate through the medium. The pressure reflection coefficient is given by

$$R = \frac{Z_1 - Z_2}{Z_1 + Z_2} = \frac{\rho_1 c_1 - \rho_2 c_2}{\rho_1 c_1 + \rho_2 c_2}, \tag{2.3}$$

where Z is the acoustic impedance of the medium, ρ is the medium density, and c is the speed of sound. The transmitted wave's direction is given by the angle θ_t dependent on the angle of incidence angle θ_i. Snell's law gives both angles,

$$\frac{c_1}{c_2} = \frac{\sin\theta_t}{\sin\theta_i}. \tag{2.4}$$

Snell's law describes the reflections happening at distinct boundaries between two mediums with different acoustic properties. The reflections governed by Snell's law is known as geometrical scattering and results in specular reflections. This is one of three types of scattering. The three types are dependent on the size of the

object scattering the sound - the scatterer. When the scatterer is much larger than the wavelength of the transmitted wave, we have geometrical scattering with specular reflections. Rayleigh scattering, also known as diffuse scattering, occurs when the scatterer is much smaller than the transmitted wavelength. If enough small scatterers are present, we get multiple scattering, resulting in the well-known speckle pattern in ultrasound imaging. The statistical distribution of speckle in ultrasound is well known (see Section 2.9). . The third type of scattering is when the scattering structure is comparable to the size of the transmitted wavelength.

In summary, some of the signals transmitted into the body will be reflected or scattered back and recorded by the ultrasound probe, which transmitted the signal. In all, only 1 % of the sound waves transmitted into the body return to the probe (Soni, Arntfield, and Kory 2014).

2.3 The ultrasound probe

In medical ultrasound imaging, the waves are transmitted into the body using a probe consisting of an array of elements. A two-dimensional array is used for 3D imaging. We will restrict ourselves to 2D imaging and consider two variants of one-dimensional ultrasound probes: a linear and a phased array. Conventionally the elements of a probe are made from piezoelectric ceramics, exploiting the piezoelectric effect to create the ultrasound signal.

2.3.1 Linear array

We will use the L7-4 (Philips, Amsterdam, NL) probe shown in Figure 2.2 to describe a conventional linear array. The array consists of 128 elements with a pitch, the distance between the center of the elements, of 0.2980 mm. The height of the elements is 7 mm. Using a center frequency of 5.2 MHz results in $\approx \lambda$ pitch, where $\lambda = c/f$ is the wavelength. To characterize the probe we make some assumptions. We assume that the response in focus is similar to the far-field response (Steinberg 1976), and assume point sources. The beampattern can then be calculated by the discrete aperture smoothing function, the discrete Fourier transform, of an array along the x-axis as, see e.g., (Johnson and Dugdeon 1993)

$$W(k_x)_{\text{one way}} = \sum_{m=0}^{M-1} w_m e^{jk_x x_m}. \tag{2.5}$$

Here w_m is the element weight, k_x is the x component of the wavenumber vector, and x_m is the element position. The relation between k_x and the incidence angle θ of the wave is, $k_x = -k \sin\theta = -\frac{2\pi}{\lambda} \sin\theta$ (Johnson and Dugdeon 1993). Using (2.5) and assuming a narrow band with a center frequency of $f_c = 5.2$ MHz we get the beampattern for the L7-4 probe as plotted in the top plot of Figure 2.2b. The x-axis in the plot is expressed as the lateral axis in the image, relating the angular resolution to the x-axis through a small angle approximation. The small angle approximation means it is only valid around the focus center, around the main-lobe, which is what we are mostly interested in.

In ultrasound imaging, we are first transmitting and then receiving the signal. When using a focused transmit and receive, and assuming we use the full array for both, the final response of the probe is given by the two way beampattern, which can be calculated by (Johnson and Dugdeon 1993)

$$W_{\text{two way}} = W_{tx} W_{rx} = W^2_{\text{one way}}. \tag{2.6}$$

The two way beampattern for the L7-4 probe is plotted in the lower plot of Figure 2.2b. The beampattern is often used to characterize the resolution of a system. There exist many definitions of the resolution but perhaps the most used is the -6 dB width of the mainlobe, also known as the full width half maximum (FWHM). For a linear array, the angular resolution at -6 dB can be

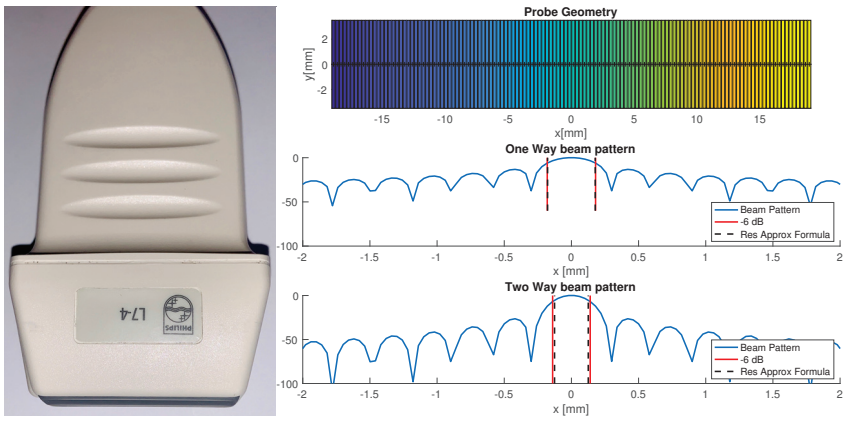

(a) (b)

Figure 2.2: The Philips L7-4 linear array probe imaged in (a) with the geometry and corresponding beampatterns calculated from (2.5) in (b). The vertical lines indicates the -6dB resolution (FWHM) calculated from the approximation formulas in (2.8) and (2.9) and estimated from the beampattern. The x-axis in the plot of the beampatterns is expressed as the lateral axis in the image, relating the angular resolution to the x-axis through a small angle approximation.

approximated by (Harris 1978)

$$\theta_{6dB} \approx \frac{1.21\lambda}{D}, \tag{2.7}$$

where D is the size of the full array aperture. Notice how the resolution is inverse proportional to the size of the array, and proportional to the signal frequency through the wavelength λ. The spatial lateral resolution at a certain depth, z, can be found using a small angle approximation

$$x_{\text{res}} = z\theta_{6dB} = z\frac{1.21\lambda}{D} = 1.21\lambda f\#. \tag{2.8}$$

Here we defined the f-number $f\# = \frac{z}{D}$ as the ratio between the depth and the size of the aperture D. We will later, in Section 2.6.2.1 see how we can use receive apodization to reconstruct a constant $f\#$ giving uniform resolution in the final image. For the x-axis in Figure 2.2b we have used this small angle approximation and assumed that $z = D$, thus that the $f\# = 1$.

An approximation for the two-way resolution, see derivation in Appendix A, assuming the same array has been used for both transmit and receive is

$$x_{\text{res two way}} \approx \frac{1.21\lambda z}{\sqrt{2}D}. \tag{2.9}$$

In Figure 2.2b we have estimated the -6 dB resolution found from the beampattern, and by using the approximation formulas in (2.8) and (2.9). From the figure, we see that the approximation fits pretty good.

2.3.2 Phased array

To demonstrate a typical phased array, we will use the P4-2 probe from Verasonics (Kirkland, Washington, USA) shown in Figure 2.3a. The P4-2 array has 64 elements with a pitch of 0.3 mm. Assuming a center frequency of 2.9 MHz, we get the beampatterns, using the same assumptions as earlier, calculated with (2.5) in Figure 2.3b.

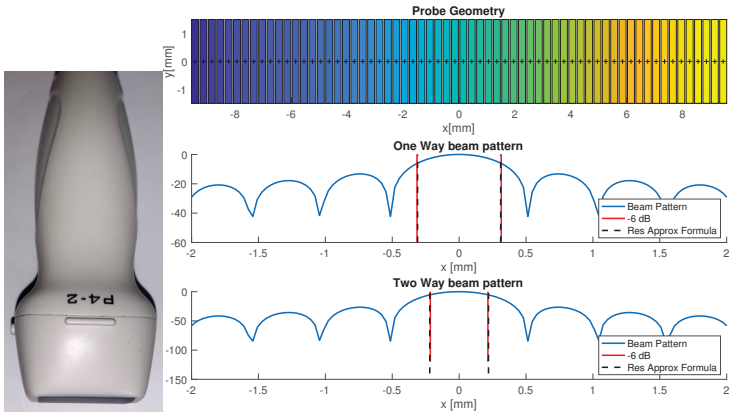

(a) (b)

Figure 2.3: The Verasonics P4-2 phased array probe imaged in (a) with the geometry and corresponding beampatterns calculated with (2.5) in (b). The vertical lines indicates the -6dB resolution (FWHM) calculated from the approximation formulas in (2.8) and (2.9) and estimated from the beampattern. The x-axis in the plot of the beampatterns is expressed as the lateral axis in the image, relating the angular resolution to the x-axis through a small angle approximation.

Notice that the resolution of the P4-2 array is significantly lower than for the L7-4 probe. The resolution is lower because of the smaller array and the lower frequency used for cardiography. To be able to image between the ribs, the array must be smaller, and the lower frequency is necessary to penetrate deep enough to image the full heart. The phased array gets its name from the fact that most cardiac applications use transmits beams at steered angles, resulting in a sector scan. While a linear array usually transmits straight forward-focused beams in front of the transducer resulting in a linear scan. However, in Section 2.4, we will see that the flexibility of software beamforming allows many kinds of transmit beams.

2.3.3 Elevation resolution

The resolution in the elevation dimension can be derived using the same analysis as we did for the axial dimension. However, the elevation resolution is dependent on the element height or for a 2D array, the array of elements in the elevation dimension.

2.3.4 Axial resolution

For completeness, we will add that the axial resolution is independent of the probe geometry but dependent on the transmit pulse. A rule of thumb for the axial resolution is (Franceschetti and Lanari 1999)

$$z_{\text{res}} = \frac{c}{2B}, \tag{2.10}$$

where c is the speed of sound, and B is the transmitted pulse bandwidth.

2.4 Transmission of ultrasound waves

Ultrasound imaging uses the pulse-echo principle. Meaning that the ultrasound wave is transmitted from the probe, and after the wave is transmitted, the same probe starts to receive the ultrasound signal reflected, echoed, from the body. The ultrasound wave travels with the speed of sound, typically assumed to be 1540 m/s for the body. The next wave cannot be transmitted before the two-way travel time from the deepest point in the image to be reconstructed, have been reached. Several, up to hundreds, of transmits are used per image effectively limiting the imaging frame rate. The best image quality is obtained if there is a focused transmit and a focused receive. Conventionally, this was done using a focused transmission, with a dynamic focusing applied on receive through the beamforming process, see Section 2.6. However, a focused transmission is illuminating only a small region of the image, and thus, a large number of transmits are needed resulting in a relatively low frame rate. Modern beamforming techniques utilize variously unfocused transmit waveforms. These unfocused transmit waveforms can synthetically be combined to recreate a focused transmission by a technique knows as coherent compounding, see Section 2.6.3. We will now consider the three most typical types of transmit waveforms: planar, diverging, and converging. These three transmit waveforms can be used to create the four most used types of imaging modalities known as plane wave imaging, diverging wave imaging, synthetic transmit aperture imaging, and focused imaging.

2.4.1 Plane Waves (PW)

The breakthrough of coherent plane wave compounding (CPWC) imaging came with the paper published by Montaldo et al. 2009. They showed that very high frame rate imaging is possible by utilizing planar transmits. Higher quality images can be achieved by coherently compounding multiple plane wave images. The high frame rate is possible because a plane wave illuminates a large, or the full, region one wants to image. This greatly reduces the number of transmits necessary to form an image. To illustrate this, we allow ourselves to make a leap forward in our understanding of ultrasound imaging and assume that we know how to recreate an ultrasound image. Thus, in Figure 2.4, three resulting images from single plane wave transmissions are shown. The time each element transmitted the ultrasound pulse, the transmit waveform delay, is plotted. The transmit waveform delay illustrates how we can steer the plane waves at different transmit angles. Notice how the plane waves steered at an angle in Figure 2.4 (a) and (c) only illuminates a part of the image, while the plane wave transmitted straight forward (b) is illuminating the entire image. An individual plane wave image has quite low quality in terms of contrast and resolution. However, for some applications such as Doppler imaging of the blood, the benefits of high frame rate outweigh the low image quality. Higher image quality, comparable to a fully focused image, can be obtained if enough plane waves transmitted at different angles are coherently compounded (Montaldo et al. 2009). However, coherent compounding is sensitive to targets moving between transmits, and

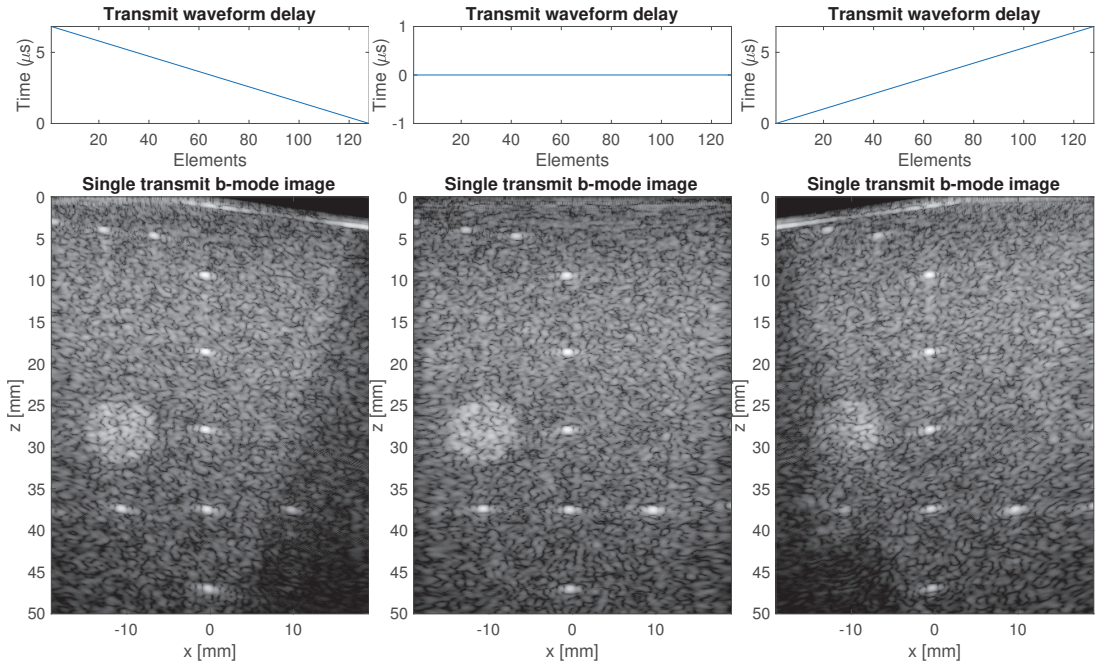

(a) PW at −16° (b) PW at 0° (c) PW at 16°

Figure 2.4: Illustration of three single plane wave images with the top plot showing the transmit waveform delay and the bottom showing the resulting images after beamforming. Note how the steered plane waves (a) and (c) are only illuminating a part of the image, while the plane wave transmitted straight forward (b) is illuminating the entire image. Data from (Liebgott et al. 2016).

the assumption of a plane wave is only valid in a certain region along with the propagating wave. Outside the region, ”edge waves” not following a plane propagation degrades the image quality since the plane wave assumption does not hold.

2.4.2 Diverging Waves (DW)

To have an even broader illumination of a region, one can transmit diverging waves. As illustrated in Figure 2.5 these images is illuminating a sector growing with depth, making it suitable for a sector scan used in, for example, cardiac imaging. Cardiac imaging uses a sector scan since it is restricted to a narrow *acoustical window* between the ribs. And thus, diverging waves are mostly applied for cardiac applications as described in (Papadacci et al. 2014). The same discussion on the pros and cons of PWs applies to DWs, where higher image quality can be obtained by coherently compounding multiple low-quality images.

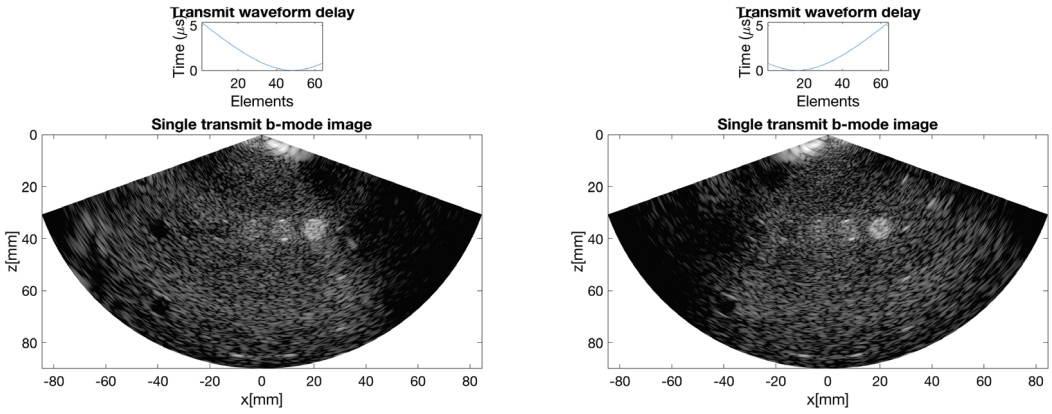

(a) DW at $-30°$

(b) DW at $30°$

Figure 2.5: Two single transmit images, bottom, created from a DW transmitted at two different transmit angles reconstructed in a sector scan. The transmit waveform delay is plotted in the top. The DW in (a) had a virtual source at $x = 4.8$mm, $z = -8.3$mm and the DW in (b) had a virtual source at $x = -4.8$mm, $z = -8.3$mm.

2.4.3 Synthetic Transmit Aperture Imaging (STAI)

The images with the highest image quality are created by synthetic transmit aperture imaging (STAI). With STAI imaging, we mean transmitting on every single consecutive element but receiving on the full array, see for example (Jensen et al. 2006). STAI has some obvious drawbacks such as penetration depth, and as with DWs and PWs the coherent compounding is sensitive to imaging moving targets. The limited penetration depth has been, slightly, improved by instead of firing a single element firing on a group of elements. In both cases, a diverging wave originating from the center of the firing element(s) is formed. The high image quality is obtained because we create a synthetic focus in the reconstruction. Compared to PW and DW imaging, the assumption of a diverging wave from each element holds for the entire propagation of the wave. Figure 2.6 shows three

images created from single element transmission; the top plot now indicates the transmitting element.

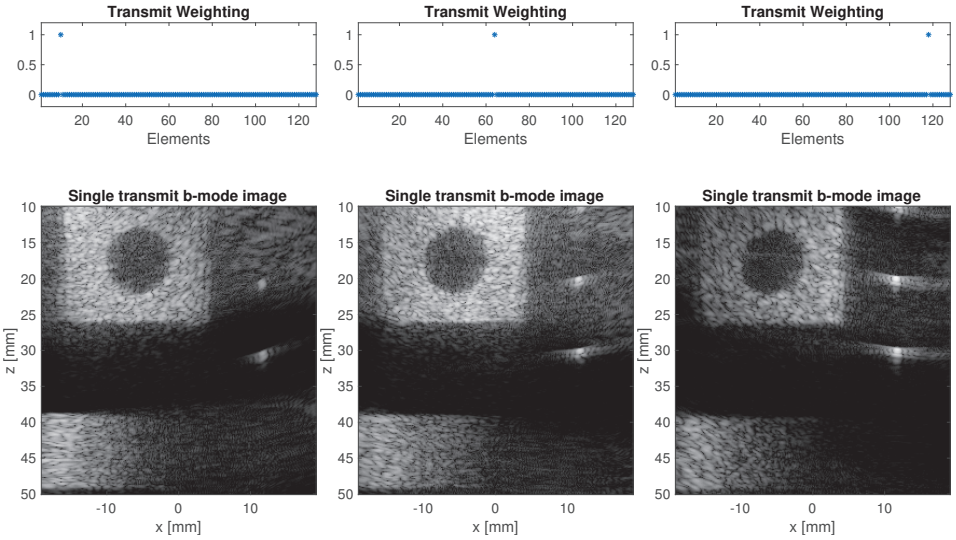

(a) Firing from element 10

(b) Firing from element 64

(c) Firing from element 118

Figure 2.6: Three single transmit images resulting from a single element transmit, as used in STAI imaging. The top plot indicates the firing element, the bottom image is the resulting image. Data from **(Paper VII)**.

2.4.4 Focused Imaging (FI)

Historically ultrasound transmissions where focused transmission meaning a first converging, towards a focus point, and then diverging wave front. This is still, to the authors knowledge the most used type of transmit in modern ultrasound systems. Conventionally, one transmit results in one *scan-line* in the final image. Typically tens to hundreds of transmits are used per image. With the flexibility of software beamforming we can, as with the previous imaging modalities, recreate the full image from a single transmit. This can be exploited in more sophisticated imaging techniques such as in multi line acquisitions (MLA, see Section 2.6.5) and retrospective beamforming (RTB, see Section 2.6.6). RTB, and to a certain degree MLA, recreates a synthetic focus in the overlapping regions between transmits, generating a synthetic focus through coherent compounding resulting in a fully focused image. To illustrate the waveform resulting from FI imaging, we have reconstructed the full image from single focused transmits in Figure 2.7, with the transmit element waveform delays plotted in the top.

It is worth to mention, without going two deep into non-linear acoustics, that FI images have benefits over PW, DW, and STAI imaging regarding second harmonics imaging. FI obtains higher peak pressure in the body, which generates more non-linearity resulting in more second harmonics generated.

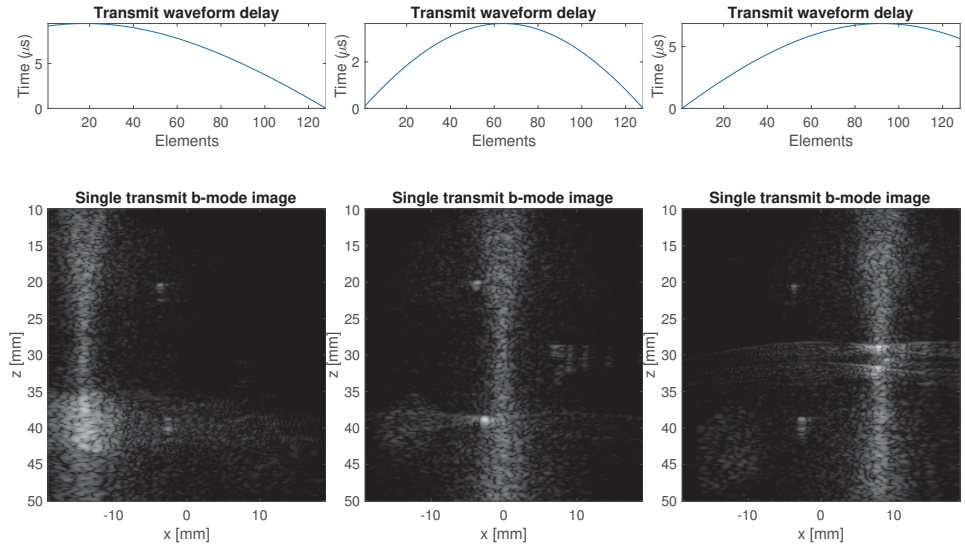

(a) Focus $x = -16, z = 30$

(b) Focus at $x = 0, z = 30$

(c) Focus at $x = 8, z = 30$

Figure 2.7: Three single transmit images from a FI transmission in the bottom, with the transmit waveform delay in the top. Data from **(Paper II)**

2.5 Representing the channel data

The ultrasound waveforms are transmitted into the body. The reflected signals are recorded with the array of elements in the ultrasound probe. Signals originating from deeper inside the body will be more attenuated than signals from shallow reflections. The signals are time gain compensated (TGC) to compensate for this attenuation. We will, from now on, assume that all signals have gone through appropriate TGC. Now, we will look at three different ways of representing the received channel data, as RF (radio frequency) data, as the analytical signal or as (In-phase Quadrature) IQ data.

2.5.1 RF-channel data

If we know our signal processing, including the Nyquist sampling criteria, we should sample the data at twice the highest frequency. Theoretically, this should be fine, however practically sampling at a higher frequency makes designing receiving filters easier. We will denote as the RF-channel data the channel data sampled according to the Nyquist sampling criteria.

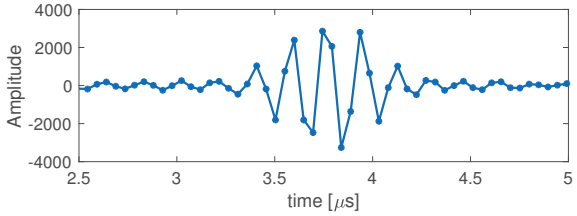

(a) Part of RF signal from a single element.

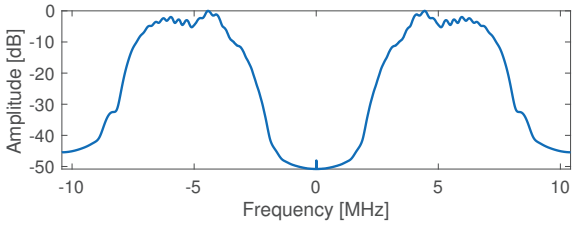

(b) Fourier power spectrum of a full data set.

Figure 2.8: Part of a RF signal from a single element in the received data used to reconstruct the image in Figure 2.7. The averaged Fourier power spectrum of the full received dataset.

As an example, we will consider the RF-channel data as generated by the Verasonics Vantage 256 system. Here, the default sampling rate is four times the transmitted center frequency. The channel data used to recreate the FI images in Section 2.4.4 were transmitted using a center frequency $f_c = 5.208$ MHz and sampled with a sampling frequency of $f_s = 4f_c = 20.83$ MHz. In Figure 2.8a, we have plotted a part of the signal received on element 10 for one of the transmits.

In Figure 2.8b, we have plotted the averaged Fourier power spectrum of the full data set.

2.5.1.1 The analytical signal

In medical ultrasound imaging, our result is an image of the received signal envelope. A convenient way of detecting the envelope is to use the analytical signal, which is defined as

$$x_a(n) = x(n) + j(\hat{x}(n)), \tag{2.11}$$

where x is the RF signal, while $\hat{x}$ is the Hilbert transform of x.

The envelope can be detected by simply taking the magnitude of the analytical signal $a(n) = |x_a[n]| = \sqrt{x(n)^2 + \hat{x}(n)^2}$. Figure 2.9a shows the analytical signal from the same FI data set from Section 2.4.4, and Figure 2.9b is it's Fourier power spectrum. Notice, from the power spectrum, that the analytical signal is a one-sided complex signal.

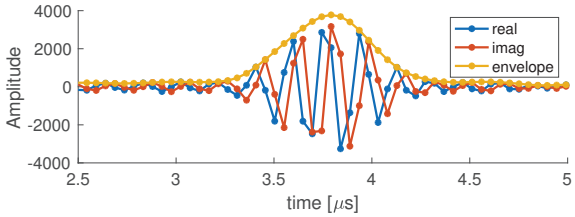

(a) Part of the analytical signal, the real (blue), the imagninary (red) and the envelope (yellow) from a single element

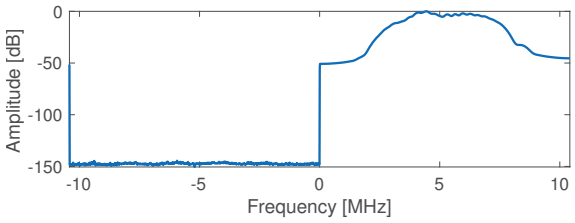

(b) Fourier power spectrum of a full analytical data set

Figure 2.9: The real, imaginary and the envelope of the analytical signal from a single element in the received data used to reconstruct the image in Figure 2.7. The averaged Fourier power spectrum of the full received analytical dataset in (b). Notice that the analytical signal is a one-sided complex signal.

The benefit of using the analytical signal, as we do in the USTB, is that it makes it easier to do envelope detection after beamforming. Using the analytical signal throughout the beamforming relaxes the number of axially reconstructed pixels. It also facilitates some adaptive beamforming techniques, that we will get back to in Section 2.7, such as Capon's minimum variance beamforming. The Capons minimum variance technique needs to create complex weights and needs

to be able to create unsymmetric, in frequency space, weight sets. Complex data also facilitates some Doppler-techniques.

2.5.2 IQ-channel data

The received ultrasound signal is bandlimited. Therefore, one can obtain more compact forms of storing the bandlimited signal through the In-phase Quadrature (IQ) signal. There are multiple definitions and variations of the IQ-signal. We will, however, briefly look into two ways the IQ-signal can be obtained. The first approach is to demodulate the RF signal into the IQ-signal. The second approach is to undersample the signal.

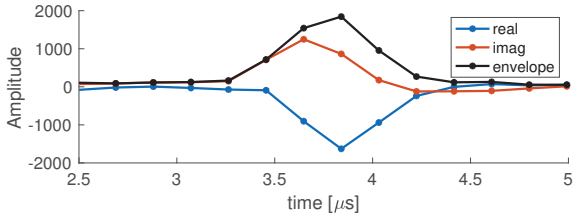

(a) Part of the IQ signal, the real, the imaginary and the envelope from a single element.

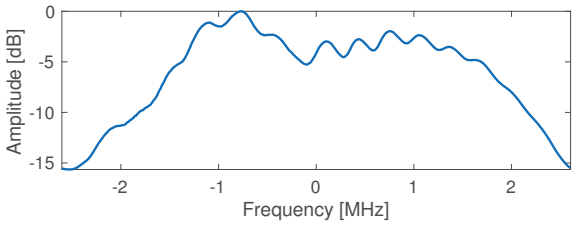

(b) Fourier power spectrum of a full IQ data set.

Figure 2.10: The real, imaginary and the envelope of the IQ signal from a single element in the received data used to reconstruct the image in Figure 2.7. The averaged Fourier power spectrum of the full IQ dataset in (b). Notice that the spectrum of the IQ signal is complex and centered around 0 MHz.

2.5.2.1 Demodulation

To describe demodulation, let's reuse a slightly modified text from (Palmer et al. 2016)

> The concept of In-phase Quadrature (IQ) data sampling is worth a brief explanation, for a more thorough description, see (Proakis and Manolakis 2007). When we have a bandlimited RF-signal centered around a center frequency, the IQ-signal can be obtained by down-mixing the signal. Down-mixing means multiplying the signal with a complex sinusoid signal given by a demodulation frequency f_{demod} "moving down" the signal in the frequency spectrum by

> using a negative demodulation frequency. This gives an asymmetrical and thus complex signal. This signal can then be low-pass filtered removing the frequencies and noise outside the desired bandwidth. This lowpass-filtered signal can then be decimated reducing the number of samples by a integer factor, in our case 4 compared to the default Verasonics RF-sampling frequency. However, we need to keep in mind that the IQ-sample is complex, thus having both a real and an imaginary part.

If we take the same signal as earlier and do this demodulation process, we end up with the complex IQ-signal plotted in Figure 2.10a with the frequency spectrum in Figure 2.10b. Notice that the spectrum of the IQ signal is complex and centered around 0 MHz, since a demodulation frequency equal to the center frequency was used.

The benefit of using the IQ signal is that it reduces the number of samples, allows easy detection of the envelope, and that it facilitates beamforming and Doppler-techniques that need complex data. An illustration of the reduction of samples, but not losing information, can be seen by comparing the envelope from the analytical signal with the envelope of the IQ-signal plotted in Figure 2.11. Note that a better interpolator than linear interpolations should have been used.

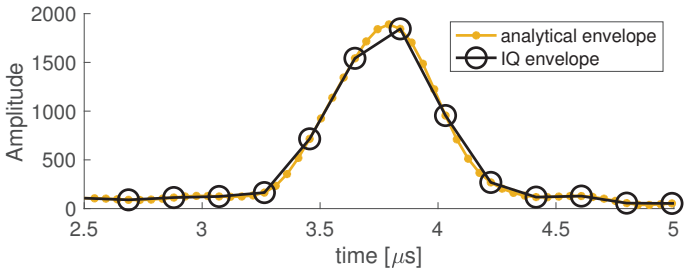

Figure 2.11: The envelope detected from the analytical signal (from Figure 2.9a) and the IQ signal (from Figure 2.10a). Notice that the signal are equal, but that the IQ signal should have used a better interpolator than a linear one.

2.5.2.2 Bandwidth sampling (Undersampling)

A second way of obtaining a variant of an IQ-signal is to do bandwidth sampling, or undersampling, of the signal directly. An intuitive explanation of this can be found in a whitepaper from Verasonics (Kaczkowski 2016). Here one sets the Nyquist sampling rate below the transducers frequency response and samples the aliased or a down-folded version of the bandlimited signal. However, to be able to do this, one needs to be able to filter out the ”unwanted” signal, which might already be present in the band the desired signal aliases into. Verasonics solves this by having programmable analog low-and highpass filters filtering out the signals before they allow the wanted signal to be folded down.

2.6 Beamforming

Beamforming denotes the process of going from the recorded channel data to a combined estimate of the reflection coefficient displayed in the final image. This section will describe the individual steps namely the waves travel time delay calculations (Section 2.6.1), the combination of the delayed signals with the delay and sum algorithm (Section 2.6.2), a closer look at the coherent compounding (Section 2.6.3) as well as going through the differences between scan-line beamforming (Section 2.6.4), multiple line acquisitions (MLA, Section 2.6.5) beamforming, and retrospective beamforming (RTB, Section 2.6.6). We will, for simplicity, only consider a linear scan in the rest of this chapter. Even though modifying the calculations to using polar coordinates facilitates the same techniques for a sector scan. However, let us first introduce beamforming by reusing some notation, definitions, and a figure from **Paper VII**.

“

Without loss of generality let us assume a linear array of M elements, laying on the x-axis, pointing towards the positive direction of the z-axis, as illustrated in Fig. 2.12. The domain, with characteristic sound speed c_0, is illuminated by a generic transmit beam, either planar, converging or diverging. Let us denote the signal received by element m as $h_m(t)$. Let us denote as T the distance from the origin of the transmitted wave to the point (x, z), and as R the distance from (x, z) to the location of element m. If we apply the propagation delay,

$$\Delta t = (T + R)/c_0, \tag{2.12}$$

we obtain the signal value at (x, z) received by element m,

$$s_m = h_m(t)|_{t=\Delta t}\,, \tag{2.13}$$

also referred to as *pixel value*. Note that we drop the spatial coordinates (x, z). The symbol s_m refers to the pixel value at an arbitrary location (x, z), unless otherwise specified.

”

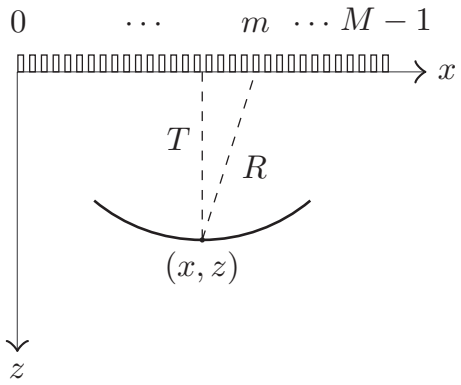

Figure 2.12: Geometrical illustration of the posed scenario. Figure from **(Paper VII)**. Credits to Alfonso Rodriguez-Molares for creating the figure.

2.6.1 Delay Calculation

Beamforming can be view as a geometrical problem. Let us, therefore, have a look at the delay calculations involved in software beamforming. We will calculate the delays assuming *the general beamformer* as used in the USTB **(Paper I)**

> [...] around the concept of the general beamformer. The wavefronts in most ultrasound sequences can be fully defined using a single point source P: in focused imaging (FI) and retrospective transmit beamforming (RTB) P is on the transmit focal point in front of the probe, in diverging wave imaging (DWI) P is at the wave origin behind the probe, in synthetic transmit aperture imaging (STAI) P lies on the active element, in coherent plane-wave compounding (CPWC) P is at an infinite distance but in a given direction. Using point sources to define all those waves it is possible to beamform all sequences with a single algorithm.

To further comply with the general beamformer, we assume that the channel data have been compensated to fulfill the time zero convention used in the USTB. In the USTB we have defined "that time zero corresponds to the moment the transmitted wave passes through the origin of coordinates (0,0,0)" **(Paper I)**. We will, for simplicity, restrict ourselves to 2D imaging and have a closer look at how the receive distance R and the transmit distance T from (2.12) can be calculated.

2.6.1.1 Receive delay

The receive distance R from (x, z) to the location of element m is independent of the type of transmit and can be calculated as

$$R(x, z, m) = \sqrt{z^2 + (x - m)^2}. \tag{2.14}$$

If we assume that we are imaging with the 128 elements L7-4 probe as defined in Section 2.3.1, and define a linear scan of pixels with 512 pixels from $x = -19$ to $x = 19$ mm and 512 pixels from $z = 0$ to $z = 50$ mm the receive delays can be visualized, four three of the elements, as in Figure 2.13.

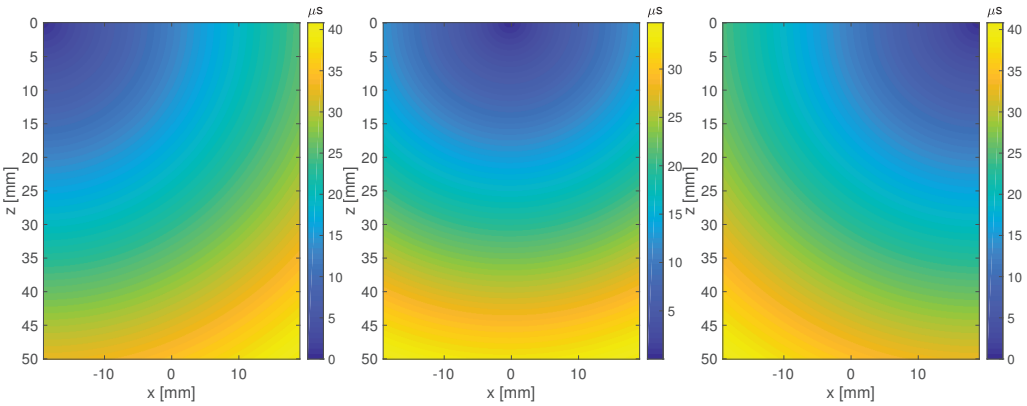

(a) Receive delay for element 1

(b) Receive delay for element 64

(c) Receive delay for element 128

Figure 2.13: Receive delay for three different elements (a) the first element, (b) the 64th element and (c) the 128th element.

The transmit distance T is dependent on the type of transmit wave, and we will consider the four different types of transmit waves, as described in Section 2.4.

2.6.1.2 Transmit delay for Plane Waves (PW)

When one or multiple planar transmit beams are transmitted into the body at different transmit angles α, we are doing PW imaging (Montaldo et al. 2009). Then the transmit distance, T, becomes

$$T_{\mathrm{PW}}(z, x, \alpha) = (z\cos(\alpha) + x\sin(\alpha)). \tag{2.15}$$

If we use the same scan and probe as earlier, the transmit delay for three different plane waves transmitted at $-30°, 0°$ and $30°$ are visualized in Figure 2.14 using the same geometry as in Figure 2.13.

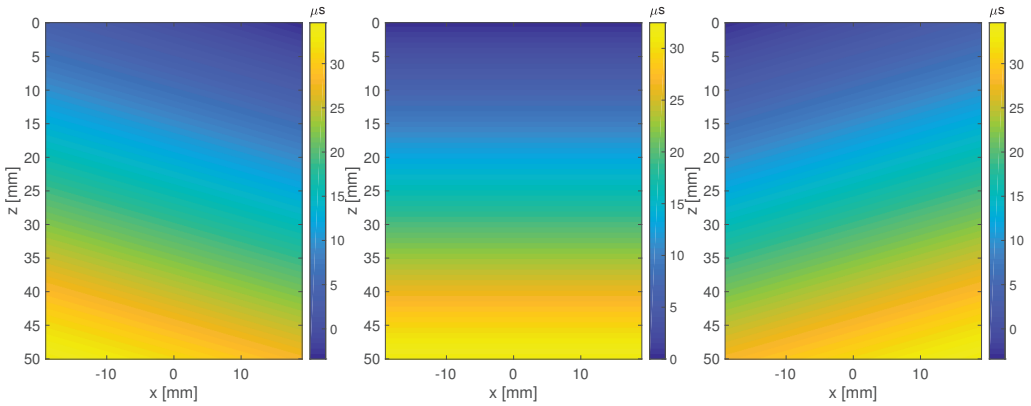

(a) Tx delay for PW at $-30°$ (b) Tx delay for PW at $0°$ (c) Tx delay for PW at $30°$

Figure 2.14: PW transmit delay for the full image scan for (a) a PW transmitted at $-30°$, (b) a PW transmitted at $0°$, and (c) a PW transmitted at $30°$.

2.6.1.3 Transmit delay for Diverging Waves (DW)

A diverging wave is formed by creating a virtual source behind the transducer at (x_s, z_s) with $z_s < 0$. The transmit distance, T, then becomes

$$T_{\mathrm{DW}}(z, x, x_s, z_s) = \sqrt{(x - x_s)^2 + (z - z_s)^2}. \tag{2.16}$$

In Figure 2.13 we have plotted the transmit delay for three DWs using the same linear scan as earlier. Even though a diverging transmit wave is usually used with a sector scan, a linear scan was used for comparison to the earlier figures.

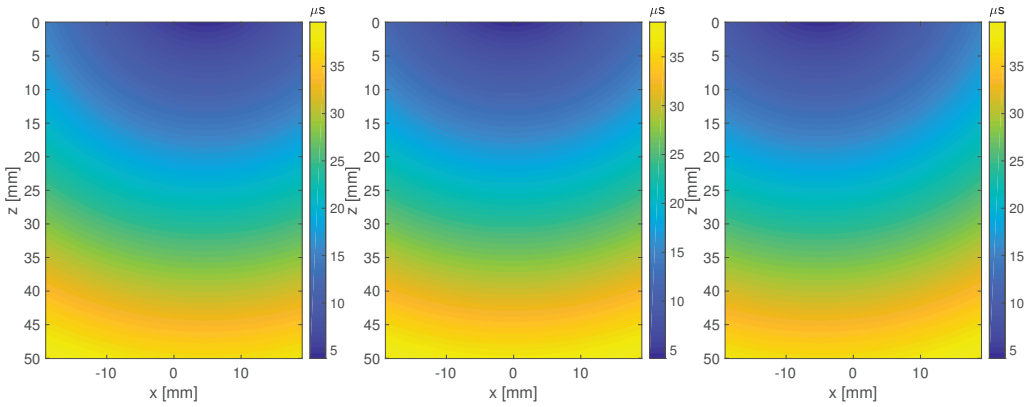

(a) DW Tx delay, source at x_s=4.8, z_s=$-$8.3mm (b) DW Tx delay, source at x_s=0, z_s=$-$9.6mm (c) DW Tx delay, source at x_s=$-$4.8, z_s=$-$8.3mm

Figure 2.15: DW transmit delay for virtual source at (a) $x_s = 4.8, z_s = -8.3$ mm, (b) $x_s = 0, z_s = -9.6$mm and (c) $x_s = -4.8, z_s = -8.3$mm.

Transmit delay for Synthetic Transmit Aperture Imaging (STAI)

The transmit delay for STAI images is the same as for a DW, but you place the source in the element firing. We can then assume $z_s = 0$ and that $x_s = x_m$ where x_m is the firing element. Thus, the transmit delay for STAI single firing element simplifies to the same as the receive delay in Figure 2.14.

2.6.1.4 Transmit delay for Focused Imaging (FI)

The transmit delay for software beamforming using Focused Imaging (FI) is actually a bit tricky. This is covered in detail in **(Paper II)**. We will again borrow some text, with some slight modifications to the notation. Compared to **(Paper II)**, we are changing from calculating the transmit time τ to the transmit distance T. The three different delay models for FI imaging; namely the spherical, the unified, and the hybrid delay model which we introduced in **(Paper II)**, then becomes.

“

Spherical delay model

Using a simple spherical model (Nikolov, Kortbek, and Jensen 2010) the transmit distance is calculated as

$$T_{\text{FI spherical}} = |\vec{v}_k - \vec{x}_k| + |\vec{p} - \vec{v}_k|, \tag{2.17}$$

where $\vec{v}_k$ denotes the location of the virtual source, $\vec{x}_k$ is the center of the transmitting aperture, and $\vec{p} = (x, z)$ is the location of the pixel in the image.

The transmit distance has two terms: the travel distance from $\vec{x}_k$ to $\vec{v}_k$, and the travel distance from $\vec{v}_k$ to $\vec{p}$. If the reconstructed point, $\vec{p}$, is in front of the focal point, the second term will be negative, and otherwise positive. This scenario is illustrated by Figure 2.16.

By looking at the two terms we can see that at the focal depth, where the second term flips from negative to positive, we will get a discontinuity in the spherical transmit delay model.

”

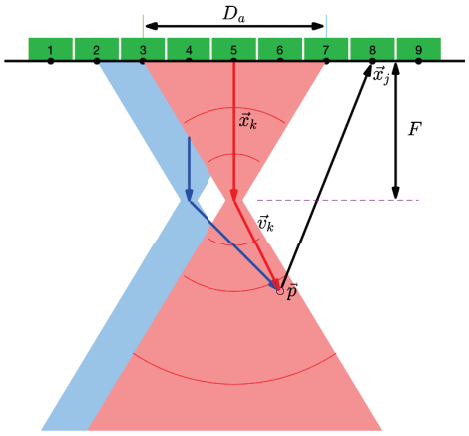

Figure 2.16: Delay geometry for a spherical virtual source as depicted in (Nikolov, Kortbek, and Jensen 2010). The blue and red indicate the insonified region from two individual transmits. Notice how they overlap in front of, and after the focal point at F. Figure credits to Andreas Austeng creating this figure from **Paper II**.

Unified delay model

In (Nguyen and Prager 2016) they analyzed and divided the transmitted wave field into four regions (I, II, III and IV) as seen in Fig. 2.17.

Their analysis showed that the transmitted signal is not a single pulse in regions II, and IV, but that it consists of two pulses that are comparable in strength. This violates the spherical wave assumption in regions II and IV, and the spherical transmit delay model is no longer valid.

As regions II and IV are not intensively insonified, the backscattered signal from these regions do not contribute significantly to the total beamformed energy. To correct the artifact (Nguyen and Prager 2016) suggested to linearly interpolate the transmit distance between regions I and III, across regions II and IV, and weighting down the amplitude of the data from regions II and IV.

The unified delay model (Nguyen and Prager 2016) then becomes

$$T_{\text{FI unified}} = \frac{|\vec{x}_b - \vec{p}|}{|\vec{x}_b - \vec{x}_a|} T_{\text{FI spherical},b} + \frac{|\vec{x}_a - \vec{p}|}{|\vec{x}_a - \vec{x}_b|} T_{\text{FI spherical},a}, \tag{2.18}$$

where $\vec{x}_a$ and $\vec{x}_b$ are vector positions of points A, B and $\vec{p}$ is the reconstructed point as seen in Fig. 2.17. $T_{\text{FI spherical},a}$ and $T_{\text{FI spherical},b}$ are the distance calculated as in (2.17) for positions A and B.

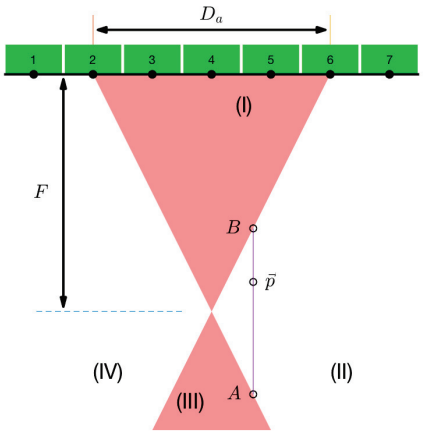

Figure 2.17: Delay geometry for the unified transmit delay model as described in (Nguyen and Prager 2016). The wavefield is divided into four regions I, II, III and IV. Region I and III follows the spherical model, while the delay for a point $\vec{p}$ in region II and IV is an interpolated value of the delay values in point A and point B. Figure credits to Andreas Austeng creating this figure for **Paper II**.

Hybrid delay model

We present a hybrid transmit delay model combining features of spherical and plane waves. In essence, we assume that the transmit wave propagates as a plane-wave in a small region m around the transmit focus, yielding the transmit distance

$$T_{\text{FI hybrid}} = \begin{cases} z, & \text{if } z > F_z - m \text{ and } z < F_z + m \\ T_{\text{FI spherical}}, & \text{otherwise.} \end{cases} \tag{2.19}$$

where F_z is the focal depth.

The transmit delay, using a slightly deeper scan than earlier, for a focused transmission from the center of the array is, for all three models, plotted in Figure 2.18.

We see that the spherical model has a discontinuity at the focus, $z = 29.6$ mm. The unified delay model does not have this discontinuity. The hybrid model "pushes" this discontinuity out of the focal zone in the lateral direction (x-direction). The discontinuity of the spherical model results in an artifact in the final image. Both the unified and hybrid model resolves this artifact - but the hybrid model is much less computationally expensive. Please see **(Paper II)** for more details, examples and in-depth discussion of this artifact. In the FI images in this chapter, such as in Section 2.4.4, we used the hybrid model.

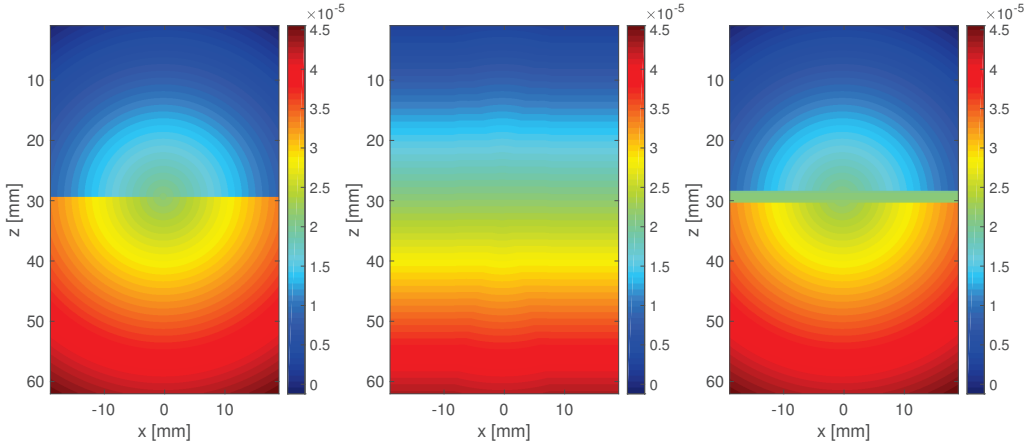

(a) Spherical FI transmit delay

(b) Unified FI transmit delay

(c) Hybrid FI transmit delay

Figure 2.18: Transmit delays for a FI transmission from the center of the array using the (a) spherical, (b) the unified and (c) the hybrid transmit delay model. Figures from **(Paper II)**.

2.6.2 The general beamformer – delay and sum

The conventional delay-and-sum (DAS) can be implemented using *the general beamformer*. The general beamformer makes "it [...] possible to beamform all sequences with a single algorithm" **(Paper I)**. The general beamformer can also, as we define it, reconstruct the image using channel data as either RF, IQ or as the analytical signal as described in Section 2.5. The DAS image is the coherent combination of the pixel values as received by all elements M from all transmits N_a. The subscript a denotes signal from each individual transmit, yielding

$$b_{\text{DAS}}(x,z) = \sum_{a=0}^{N_a-1} \sum_{m=0}^{M-1} w_a^{tx}(x,z) w_m^{rx}(x,z) s_{m,a}(x,z) e^{i2\pi f_{\text{demod}} \Delta t / f_s}. \tag{2.20}$$

Here w_m^{rx} is the receive apodization, see the details below, with dimensions $[N_z, N_x, M]$ while w_a^{tx} is the transmit apodization, see details in Section 2.6.3.1, with dimensions $[N_z, N_x, N_a]$.

If the channel data $s_{m,a}$ is the demodulated IQ-signal, we need to up-mix the signal by multiplying with $e^{i2\pi f_{\text{demod}} \Delta t / f_s}$. The demodulation frequency is f_{demod}, Δt is the delay from equation (2.12), and f_s is the sampling frequency. If we are beamforming using the RF signal or the analytical signal we can simply set the $f_{\text{demod}} = 0$ so that $e^{i2\pi f_{\text{demod}} \Delta t / f_s} = 1$.

For notational simplicity, let's rewrite (2.20). We will assume that we are using the analytical signal, and drop the spatial pixel coordinates (x, z), such that

$$b_{\text{DAS}} = \sum_{a=0}^{N_a-1} \sum_{m=0}^{M-1} w_a^{tx} w_m^{rx} s_{m,a} = \sum_{tx} w_a^{tx} \sum_{rx} w_m^{rx} s_{m,a}. \tag{2.21}$$

Note also that we can define that the inner sum over the elements is the sum over the receive (rx) dimension, while the sum over the a transmits are the sum over the transmit (tx) dimension, and that we can move the transmit weights w_a^{tx} out of the inner sum. If we have a closer look on the delayed channel data in $s_{m,a}$ we can visualize the data from each transmit a as a three dimensional cube where the first dimension is the z's, thus the depth pixels, the second dimension is the x's and the third dimension is the receive elements m. Thus, $s_{m,1}$ have dimensions $[N_z, N_x, M]$ and we will have N_a of these cubes, one from each transmit a.

2.6.2.1 Receive Apodization

The receive apodization, using a uniform rectangular window, can be calculated as

$$w_m^{rx}(z, x, x_m) = \begin{cases} 1, & \text{if } |x - x_m| \leq \frac{z}{2f\#} \\ 0, & \text{otherwise.} \end{cases} \tag{2.22}$$

Here (x, z) is the pixel position, x_m is the position of the receiving element and $f\#$ is the f-number. The f-number is defined as $f\# = \frac{z}{D}$, the ratio between the pixel depth z and the size of the aperture D. This results in an expanding aperture with a constant f-number, as shown when we, in Figure 2.19a, plot the apodization for the L7-4 probe with depth for the center pixel line, $x \approx 0$ mm, when using $f\# = 1$. Other apodization window functions can be applied. One can use the expression in (2.22) to find the "active" elements and calculate the window based on the number of active elements. This is done for the Hamming window in Figure 2.19b. The choice of window function will, as is well known, influence the resolution and side lobe suppression.

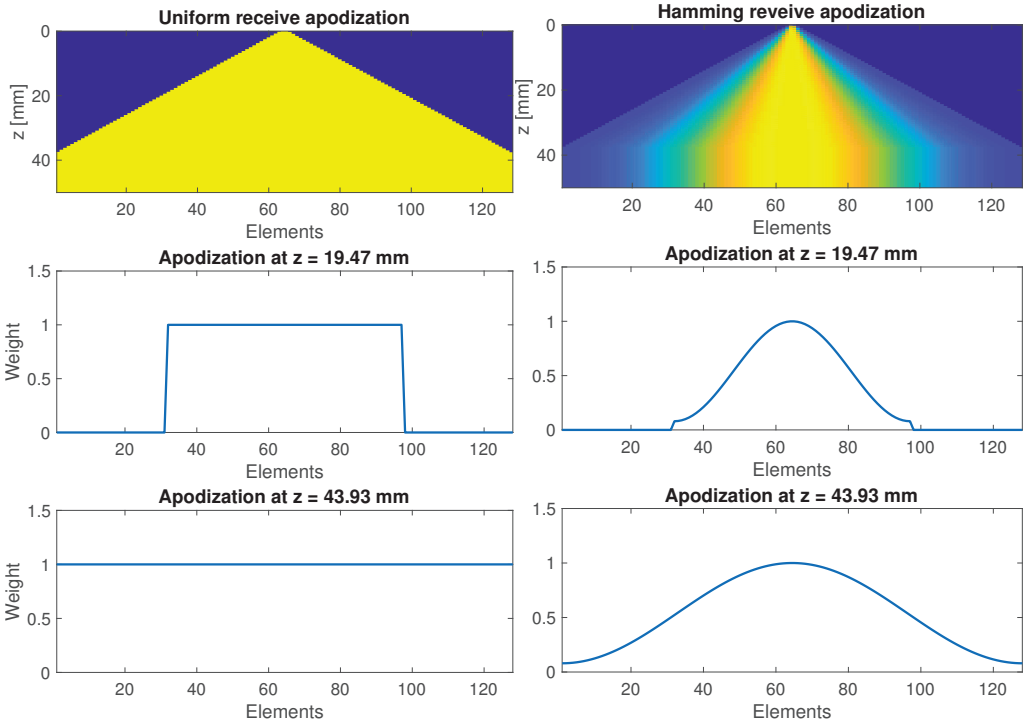

(a) Uniform receive apodization (b) Hamming receive apodization

Figure 2.19: Receive apodization for the center pixel $x \approx 0$ mm for the L7-4 probe with depth when using $f\# = 1$. A uniform window is used in (a), while a Hamming window is used in (b).

2.6.3 Coherent compounding

We can split up the sum in equation (2.21) into two

$$b_a^{\overline{R_{x\mathrm{DAS}}}} = \sum_{rx} w_m^{rx} s_{m,a} \tag{2.23}$$

$$b_{\mathrm{DAS}} = b^{\overline{T_{x\mathrm{DAS}}}\ \overline{R_{x\mathrm{DAS}}}} = \sum_{tx} w_a^{tx} b_a^{\overline{R_{x\mathrm{DAS}}}}. \tag{2.24}$$

Here $b_a^{\overline{R_{x\mathrm{DAS}}}}$ is the result from the sum over the receive elements M, where we with the superscript $\overline{R_{x\mathrm{DAS}}}$ denote that we have used a coherent combination of the signals over the receive dimensions, and equivalently that $\overline{T_{x\mathrm{DAS}}}$ denotes a coherent combination over the transmit dimension. This is what is known as coherent compounding, extensively used with plane waves (Montaldo et al. 2009) and diverging waves (Papadacci et al. 2014). All techniques dependent on coherent compounding are affected by object movement between transmissions. If the object move between transmission this will degrade the synthetic focusing mechanism of compounding (Denarie et al. 2013). There exist many studies trying to compensate for this effect, however, we will for simplicity assume stationary targets.

2.6.3.1 Transmit Apodization

The transmit apodization needs some explanation, since we in the USTB denote transmit apodization for the apodization applied over the transmit dimension of the received data, as defined in equation (2.21). The apodization applied over the elements when transmitting the ultrasound wave, we will denote transmit waveform apodization.

Transmit Angular Apodization

In (Rodriguez-Molares et al. 2015) the term angular apodization was coined to the apodization weights applied to the different single transmit low-quality plane wave images before coherent compounding. It was shown that CPWC imaging with angular apodization obtains the same image quality as STAI with apodization applied in the coherent compounding of the single transmit images and as FI with transmit waveform apodization. Thus, the results in (Rodriguez-Molares et al. 2015) shows that the transmit waveform apodization for FI imaging is connected with the angular transmit apodization applied to the receive data when synthetically creating a focus through coherent compounding.

Transmit Masking Apodization

A second type of transmit apodization is a masking apodization. Again, we are talking about transmit apodization as the apodization over the TX dimension of the received data as in equation (2.21). The masking apodization can be thought of as masking out the region insonified by the transmit beam. A good way of illustrating the region insonified is to view the single transmit B-mode image of a FI transmit. Three of these are shown in Figure 2.7.

We will consider three different imaging modalities for focused imaging which can all be viewed as a variant of transmit masking apodization. Namely, scan-line beamforming, multiple line aqusition (MLA) and retrospective beamforming (RTB).

2.6.4 Scan-line beamforming

Conventional scan-line beamforming, meaning one transmit beam resulting in one axial line in the image can be viewed as a transmit masking apodization. The masking apodization is then to mask out everything except the single line in the single transmit B-mode image. This is demonstrated in Figure 2.20 (a) to (c), where we have plotted three of the 128 scan-lines constituting the final image in (d).

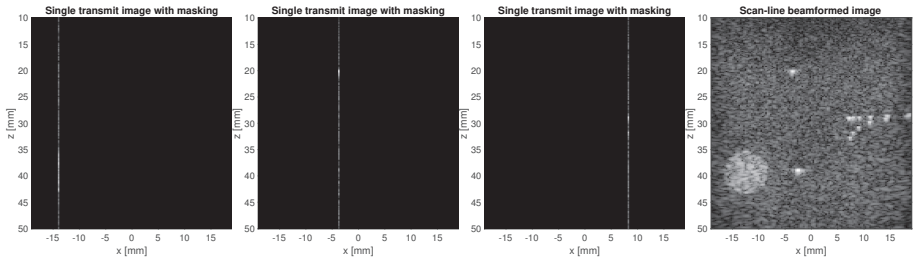

(a) single scan-line tx=18 (b) single scan-line tx=52 (c) single scan-line tx=92 (d) Full scan-line image.

Figure 2.20: Conventional scan-line beamforming as implemented in the USTB software beamforming using apodization to make one beam from each transmit.

2.6.5 Multiple Line Acquisition

To increase the image quality, a common strategy is to acquire multiple receive lines for every line transmitted - resulting in what is known as a multiple line acquisition (MLA). Alternatively, one can reconstruct an image with fewer transmits using MLA. Conventionally, this has been known as parallel beamforming (Shattuck et al. 1984), or multiline beamforming. In the PW and DW case, thus broad transmit beams, MLA can easily be implemented in software beamforming by simply defining a suitable image scan of pixels. However, with focused transmissions the narrow insonified region around focus might lead to some unwanted effects known as beam warping and skewing. These effects have been described and discussed in detail in (Hergum et al. 2007). We will not touch the details here, but the unwanted effects result in amplitude variations in the image since the receive lines do not line up with the transmit beams. One solution is the Synthetic Transmit Beams (STB) technique introduced in (Hergum et al. 2007). The STB technique introduces ”shift invariance through coherent interpolation”. In our USTB software beamforming framework this means that we can implement the STB technique using coherent compounding of single transmit images. By using appropriate transmit apodization masking we can decide the number of synthetic lines and how much they should overlap between transmits. First, let us demonstrate extra parallel receive beams, but without doing any coherent compounding between the transmits. Figure 2.21 illustrates in the two left plots the masking apodization used for $tx = 100$ and

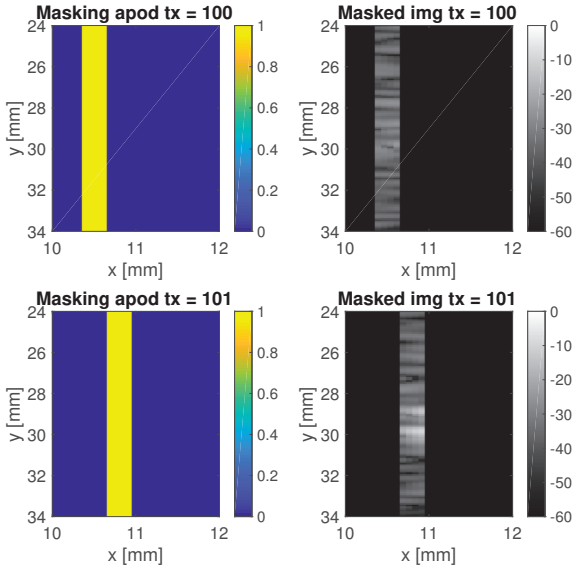

Figure 2.21: MLA beamforming with no overlap between the beams. Using 4 MLAs per beam with the transmit masking apodization in the left images, and the resulting single transmit images with the masking applied to the right.

$tx = 101$ respectively, and the corresponding single transmit images to the t using 4 MLAs.

To do coherent compounding, there needs to be some overlap between the single transmit images. Figure 2.22 demonstrates an example where we have used a total of 8 MLAs with two MLAs overlapping between each transmit. Again, the two left plots are the masking apodization used for $tx = 100$ and $tx = 101$ respectively, and the corresponding single transmit images to the right.

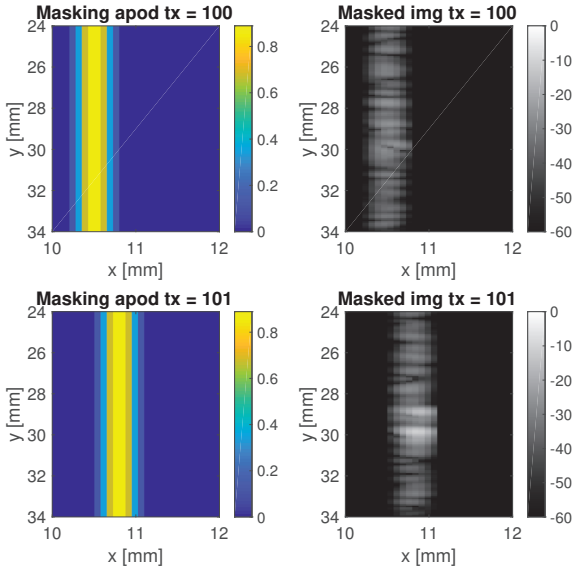

Figure 2.22: Transmit delays for a FI transmission from the center of the array using the (a) spherical, (b) the unified and (c) the hybrid transmit delay model.

From Figure 2.22 we can see how the two single transmit images now overlap and how the masking is created so that the amplitude in the overlapping region sums to 1.

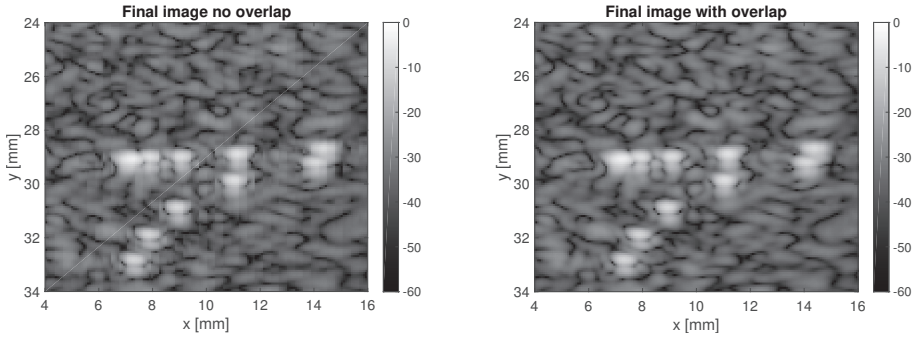

Figure 2.23: Final images created with MLAS with no overlap to the left, and with overlap to the right. Notice how the image with no overlap have some striping artifacts.

The final images are shown in Figure 2.23 from the MLAs with no overlap to the left, and the MLAs with overlap to the right. Notice the striping artifacts in the left image, which is the image without overlap, and notice how the overlap between the transmit events smooths these striping artifacts out in the image to the right.

2.6.6 Retrospective Beamforming

By comparing the images with MLAs (Figure 2.23) to the conventional scan-line based image, we can see a clear improvement in the image quality. However, from the single focused transmit images in Figure 2.7, we can see that there is more than just a wide stripe that is insonified. The transmitted beam results in a converging shape before the focus, and a diverging shape after the focus. Thus, there is more than the ”stripe” exploited in the MLA technique that overlaps between transmits. This brings us to, to the author’s knowledge, the state of the art in terms of image quality; retrospective beamforming (RTB). The concept have been known for some time, and already in 1995 Freeman, Li, and Odonnell published the paper titled Retrospective Dynamic Transmit Focusing. RTB has further been refined and is today considered a technique that uses a ”virtual source” in focus (Frazier and O’Brien 1998)(Bae 2000)(Nikolov, Kortbek, and Jensen 2010). RTB imaging can also be implemented, as is done in the USTB, using the general beamformer and a transmit masking apodization. Figure 2.24 shows to the left a full FI single transmit image, and to the right, the same image but with a suitable transmit masking apodization applied. The transmit masking is masking out the part of the image that is insonified. We will not touch the details here. However, the calculation is based on the transmit foci and the number of active elements in the transmission.

The advantage of RTB imaging is that it combines the benefits from a focused transmission and the synthetic focusing achieved from coherent compounding.

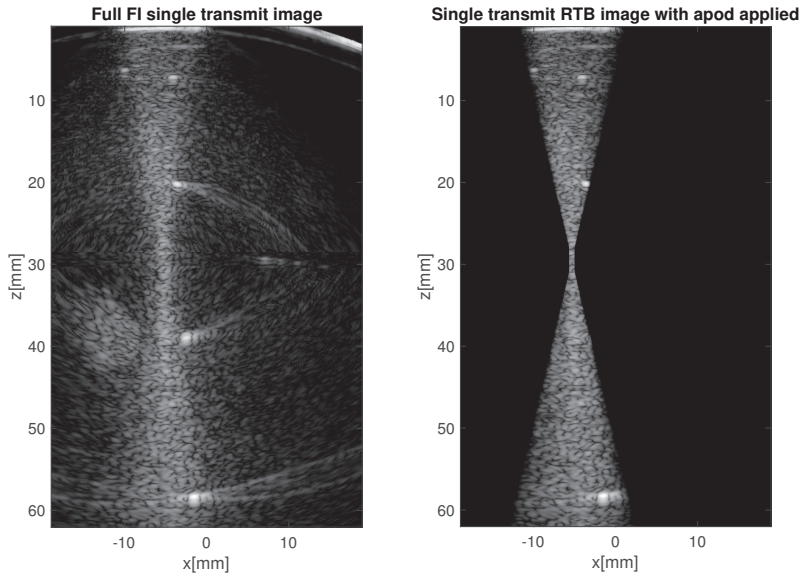

Figure 2.24: Transmit delays for a FI transmission from the center of the array using the (a) spherical, (b) the unified and (c) the hybrid transmit delay model.

Figure 2.25 shows three single transmit apodized images from transmit 47, 52, and 57, respectively. Notice, for example, how the point scatter at $z = 20$mm, $x = -2$mm is visible in all three images, and thus is for all ten single transmit images between $tx = 47$ and $tx = 57$. The point scatterers deeper in the image will be insonified in even more transmits as the overlap region is largest away from the foci. Thus, there is a nice correlation between the number of overlapping transmits and how unfocused the transmit is.

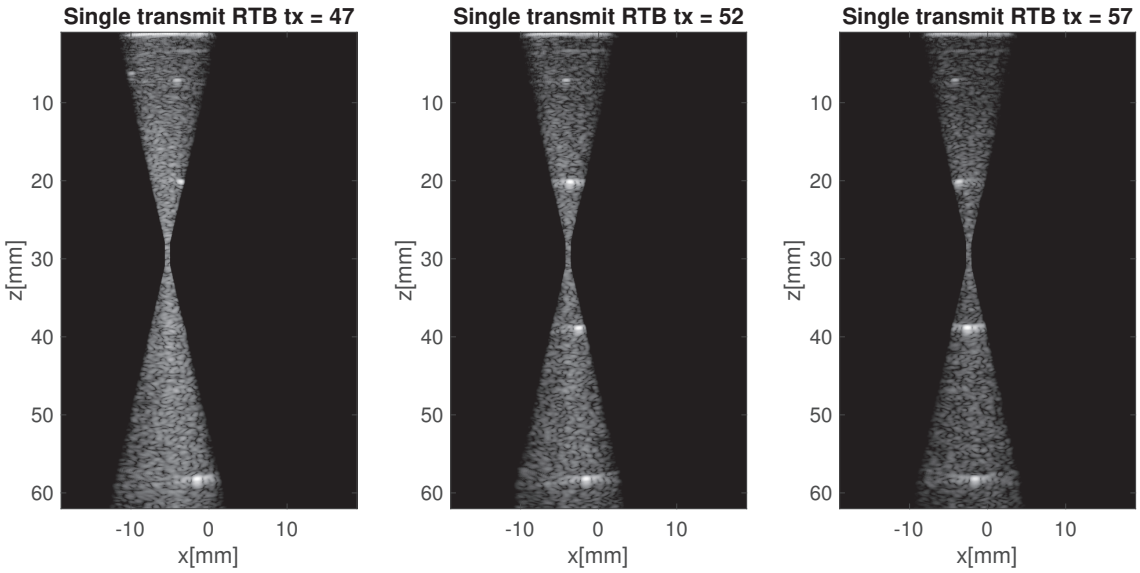

Figure 2.25: Transmit delays for a FI transmission from the center of the array using the (a) spherical, (b) the unified and (c) the hybrid transmit delay model.

Figure 2.26a is the resulting image from the coherent compounding of the

masked single transmit RTB images. The lower amplitude in the focal region is because this region had the least number of overlaps. To compensate for the difference in amplitude, we apply an apodization based on the single transmit apodization masks. The final image is displayed in Figure 2.26b.

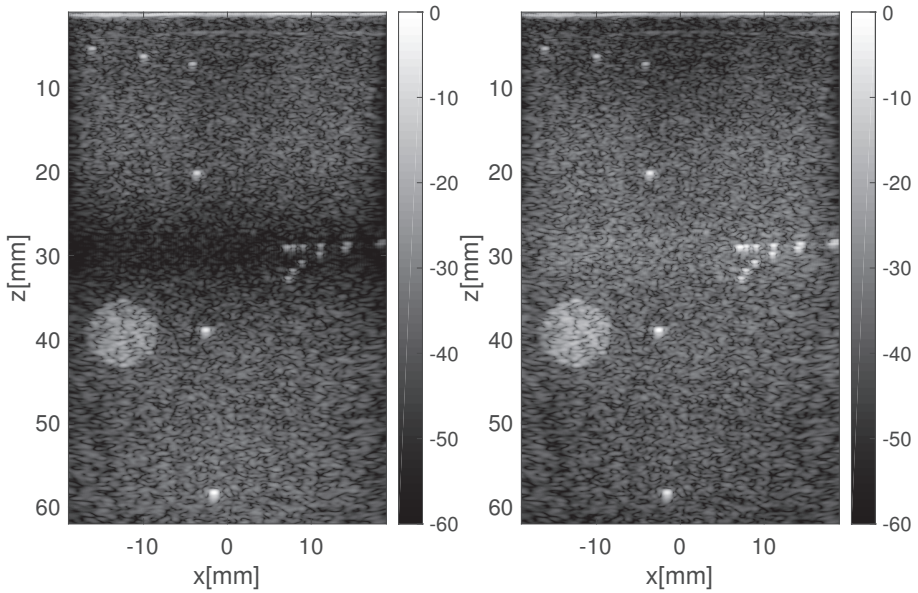

(a) Spherical FI transmit delay

(b) Unified FI transmit delay

Figure 2.26: Transmit delays for a FI transmission from the center of the array using the (a) spherical, (b) the unified and (c) the hybrid transmit delay model.

A comparison between the conventional scan-line beamforming, MLA beamforming and RTB beamforming is made in Figure 2.27. The images are created from the same channel data with the same number of transmits. For completeness, we also included an interpolated version of the scan-line beamformer to have the same number of pixels as for the MLA and RTB images. In Figure 2.27, we have zoomed in on the group of scatterers in the focal region. The B-mode image is shown in the top, while the lateral line through the scatterers is plotted below.

As expected, the MLA and RTB have some improved resolution, in terms of increased separability between the two leftmost scatterers. The difference between MLA and RTB is minimal. This is as expected, since these scatteres are located close to the foci where the MLA is already quite optimal.

However, in Figure 2.28 we investigate a point scatterer further away from the foci. From the B-mode images, and especially the plot of the axial line, we can observe that RTB resulted in an improved resolution. The improved resolution is because the coherent compounding in the overlapping regions of RTB resulted in an improved synthetic resolution for the RTB. Also, notice the improved side-lobe levels.

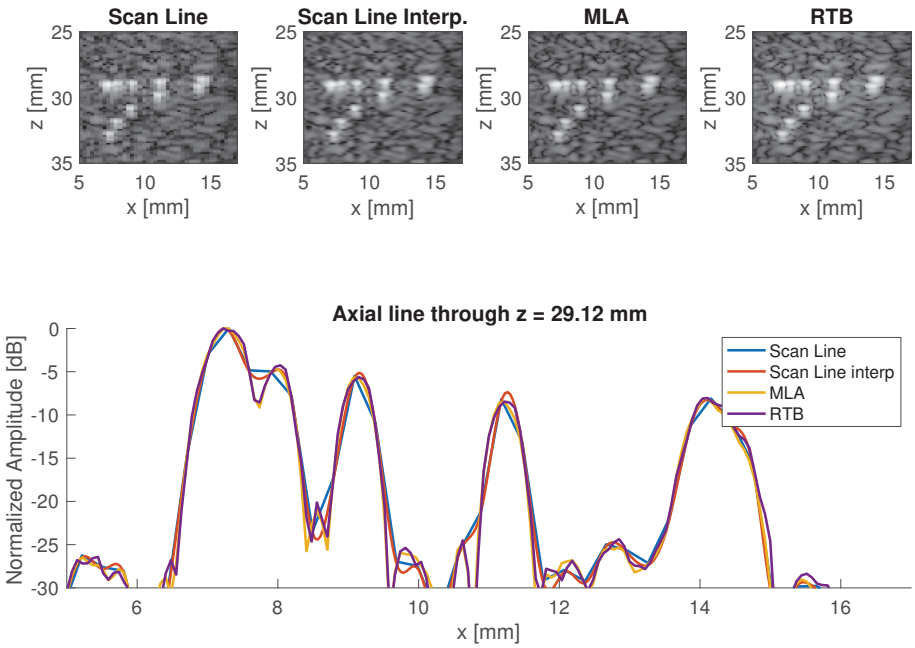

Figure 2.27: The conventional scan-line image in the top left, followed by an interpolated version of the scan-line image, the MLA image and the RTB image. The plot below is the axial line through the group of scatterers close to the foci.

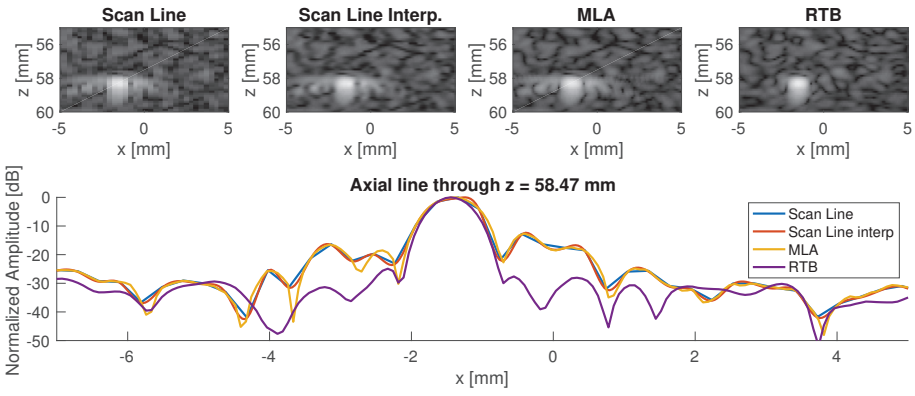

Figure 2.28: The conventional scan-line image in the top left, followed by an interpolated version of the scan-line image, the MLA image and the RTB image. The plot below is the axial line through the single scatterer almost 30 mm below the foci.

2.7 Adaptive beamforming

Most of the work in this thesis regards the image quality resulting from adaptive beamfoming **(Paper IV, V, VI, VII, VIII, IX and X)**. We will reuse a compact definition and introduction to adaptive beamforming from **Paper VII**:

> The popularization of software beamforming has brought numerous techniques that, by clever manipulation of channel data, are able to exceed the contrast and resolution provided by conventional delay-and-sum (DAS) beamforming. We refer as adaptive beamforming to any technique where the signal values alter the way the beamformed signal is constructed, for instance when the element weights are determined from the variance of the signal.
>
> Seminal work on adaptive beamforming dates back to the 1960s, where optimal element weights were derived for a given signal direction to minimize the influence of jamming signals in radio communication systems (Applebaum 1976; Bryn 1962; Capon 1964; Widrow et al. 1967).
>
> Adaptive beamforming was first applied to medical ultrasound at the end of the 1980s to compensate for phase aberration artifacts produced by tissue inhomogeneities (Flax and O'Donnell 1988; Nock, Trahey, and Smith 1989), and about a decade later to reduce the contribution of off-axis targets (Mann and Walker 2002; Sasso and Cohen-Bacrie 2005; Synnevåg, Austeng, and Holm 2005; Viola and Walker 2005; Wang, Li, and Wu 2005).

There is a myriad of techniques that are published within the field of adaptive beamforming for medical ultrasound imaging. We have implemented some of the most popular ones in the USTB. Quite some effort was spent in **Paper VII** to formulate a compact description of these adaptive beamformers. Will will, therefore, reuse the formulation here. For simplicity, compared to (2.20), we will assume only one transmit and drop the subscript a when defining the adaptive beamformers, so that $s_m(x, z)$ means the signal received on element m for pixel location (x, z).

2.7.1 Capon's Minimum Variance (MV)

> Capon's Minimum Variance (MV) technique calculates a data dependent set of weights $\boldsymbol{w}$ while maintaining unity gain in the steering direction (Synnevåg, Austeng, and Holm 2009). This is posed as a minimization problem by
>
> $$\begin{aligned} \min_{\boldsymbol{w}} \; E\left\{|b_{\mathrm{DAS}}|^2\right\} &= \boldsymbol{w}^H \boldsymbol{R} \boldsymbol{w} \\ \text{subject to } \boldsymbol{w}^{\boldsymbol{H}} \boldsymbol{a} &= \mathbf{1}, \end{aligned} \tag{2.25}$$
>
> where $\mathbf{R} \equiv E\left\{\boldsymbol{s}\boldsymbol{s}^H\right\}$ is the spatial covariance matrix, E is the expected value operator, and the steering vector $\boldsymbol{a} = \mathbf{1}$ because it is assumed that all signals are already delayed. The solution to (2.25) can by found by the method of

Lagrange multipliers, yielding

$$\boldsymbol{w}_{\mathrm{MV}} = \frac{\boldsymbol{R}^{-1}\boldsymbol{a}}{\boldsymbol{a}^H\boldsymbol{R}^{-1}\boldsymbol{a}}. \tag{2.26}$$

The spatial covariance matrix is unknown, but it can be estimated for point (x, z), assuming a linear array, by (Synnevåg, Austeng, and Holm 2009)

$$\hat{\boldsymbol{R}}(x,z) = \frac{\sum_{k=-K}^{K}\sum_{l=0}^{M-L}\overline{\boldsymbol{s}}_l(x,z-k)\,\overline{\boldsymbol{s}_l}^H(x,z-k)}{(2K+1)(M-L+1)}, \tag{2.27}$$

where $(2K+1)$ is the number of axial samples, L is the length of the subarray, and

$$\overline{\boldsymbol{s}}_l(x,z) = \begin{bmatrix} s_l(x,z) & s_{l+1}(x,z) & \dots & s_{l+L-1}(x,z)\end{bmatrix}^T. \tag{2.28}$$

The subarray averaging improves robustness. To further improve robustness, and numerical stability, diagonal loading is added to the estimated covariance matrix by $\tilde{\boldsymbol{R}}(x,z) = \hat{\boldsymbol{R}}(x,z) + \epsilon\mathbf{I}$, where $\mathbf{I}$ is the identity matrix, and

$$\epsilon = \frac{\Delta}{L} tr\{\hat{\boldsymbol{R}}(x,z)\},$$

where $tr\{\}$ is the trace operator.

The beamformed image is then computed as

$$b_{\mathrm{MV}} = \frac{1}{M-L+1}\sum_{l=0}^{M-L}\boldsymbol{w}_{\mathrm{MV}}^H\,\overline{\boldsymbol{s}}_l. \tag{2.29}$$

2.7.2 Eigenspace-Based Minimum Variance (EBMV)

The MV can be extended into EBMV. Asl and Mahloojifar 2010 was the first to apply it to beamforming for medical ultrasound. They utilized the eigenstructure of the covariance matrix aiming to obtain a better suppression of off-axis signals. The covariance matrix is estimated with (2.27) and eigendecomposed as

$$\hat{\boldsymbol{R}}_{\mathrm{DL}} = \boldsymbol{V}\boldsymbol{\Lambda}^{-1}\boldsymbol{V}^H, \tag{2.30}$$

where $\boldsymbol{\Lambda} = [\lambda_1, \lambda_2, ..., \lambda_L]^T$ are the eigenvalues in descending order, and $\boldsymbol{V} = [\boldsymbol{v}_1, \boldsymbol{v}_2, ...\boldsymbol{v}_L]$ are the corresponding eigenvectors. The signal subspace $\boldsymbol{E}_s$ can be constructed using the eigenvectors corresponding to the largest eigenvalues,

$$\boldsymbol{E}_s = [\boldsymbol{v}_1, ..., \boldsymbol{v}_E], \tag{2.31}$$

where E is the number of eigenvectors creating the signal subspace. Finally, the EBMV weight is obtained by projecting the conventional MV weights onto the constructed signal subspace

$$\boldsymbol{w}_{\mathrm{EBMV}} = \boldsymbol{E}_s\boldsymbol{E}_s^H\boldsymbol{w}_{\mathrm{MV}}. \tag{2.32}$$

The beamformed image is then computed as

$$b_{\mathrm{EBMV}} = \frac{1}{M-L+1} \sum_{l=0}^{M-L} \boldsymbol{w}_{\mathrm{EBMV}}^{H} \, \overline{\boldsymbol{s}}_l, \tag{2.33}$$

with $\overline{\boldsymbol{s}}_l$ defined as in (2.28).

2.7.3 Filtered-delay-multiply-and-sum (F-DMAS)

F-DMAS for medical ultrasound beamforming was introduced in (Matrone, Savoia, and Magenes 2015). The technique aims to increase image quality by multiplying the RF signals before summation. Namely, the signed square root signal is defined as

$$g_{ij} = \operatorname{sign}(s_i s_j) \sqrt{|s_i s_j|}, \tag{2.34}$$

where sign$(\cdot)$ denotes the sign function. The beamformed signal $b_{\text{F-DMAS}}$ is then computed as

$$b_{\text{F-DMAS}} = \left[\sum_{i=0}^{M-2} \sum_{j=i+1}^{M-1} g_{ij} \cdot \right]_{\mathrm{BPF}}, \tag{2.35}$$

where $[\cdot]_{\mathrm{BPF}}$ denotes the band pass filtering of the signal inside the brackets. Note that (2.34) is the multiplication of two signals with identical center frequency f_c, and hence it will have two frequency components: one at 0, and one at $2f_c$. Band pass filtering is applied to remove the DC component.

2.7.4 Coherence Factor (CF)

The CF was first introduced in (Mallart and Fink 1994), as the ratio between the coherent and incoherent energy across the aperture:

$$\mathrm{CF} = \frac{\left| \sum_{m=0}^{M-1} s_m \right|^2}{M \sum_{m=0}^{M-1} |s_m|^2}. \tag{2.36}$$

The CF has been used as an adaptive weight to increase image quality (Li and Li 2003) as;

$$b_{\mathrm{CF}} = \mathrm{CF} \, b_{\mathrm{DAS}}. \tag{2.37}$$

2.7.5 Generalized Coherence Factor (GCF)

In (Li and Li 2003) they generalized the coherence factor as

$$\mathrm{GCF} = \frac{\sum\limits_{n<M_0} |S_n|^2}{\sum\limits_{n=-\frac{M}{2}}^{\frac{M}{2}-1} |S_n|^2}, \tag{2.38}$$

where S is the M-point Fourier spectra over the aperture of the delayed channel data,

$$S_n = \sum_{m=0}^{M-1} s_m e^{-j2\pi(m-M/2)d\frac{n}{Md}}, \tag{2.39}$$

where $n \in [-\frac{M}{2}, \frac{M}{2}-1]$ is the spatial frequency index where M is assumed to be even, d is the pitch of the array, and M_0 is an arbitrary constant within $[0, \frac{M}{2}-1]$ that specifies the low spatial frequency region, thus going from $-M_0$ to M_0. Note that if $M_0 = 0$ the GCF simplifies to the CF.

The beamformed image is computed by multiplying the DAS image with GCF

$$b_{\mathrm{GCF}} = \mathrm{GCF}\, b_{\mathrm{DAS}}. \tag{2.40}$$

2.7.6 Phase Coherence Factor (PCF)

The PCF was introduced in (Camacho, Parrilla, and Fritsch 2009) as

$$\mathrm{PCF} = \max\left\{0, 1 - \frac{\gamma}{\sigma_0} p\right\}, \tag{2.41}$$

where γ is a parameter to adjust the sensitivity of PCF to out-of-focus signals, $\sigma_0 = \pi/\sqrt{3}$ is the nominal standard deviation of a uniform distribution between $-\pi$ and π, and p is given by

$$p = \min\left\{\sigma\left(\boldsymbol{\phi}\right), \sigma\left(\boldsymbol{\phi}^A\right)\right\}, \tag{2.42}$$

where $\boldsymbol{\phi} = [\phi_1\ \phi_2 \ldots \phi_M]$ is the instantaneous phase across the aperture, and $\sigma(\boldsymbol{\phi})$ is its standard deviation. To avoid phase wrapping discontinuity a set of auxiliary phases $\boldsymbol{\phi}^A = [\phi_1^A\ \phi_2^A \ldots \phi_M^A]$ is computed as

$$\phi_m^A = \begin{cases} \phi_m + \pi & \text{if } \phi_m < 0, \\ \phi_m - \pi & \text{otherwise.} \end{cases} \tag{2.43}$$

The beamformed image is computed using PCF as an adaptive weight

$$b_{\mathrm{PCF}} = \mathrm{PCF}\, b_{\mathrm{DAS}}. \tag{2.44}$$

2.7.7 Short Lag Spatial Coherence (SLSC)

In addition to the adaptive beamformers mentioned so far, this thesis includes a study including the Short Lag Spatial Coherence (SLSC) in **(Paper IX)**. For completeness, we will, therefore, include a definition here. The short lag spatial coherence (SLSC) algorithm was introduced in (Lediju et al. 2011). The spatial correlation can be calculated as

$$\hat{R}(m) = \frac{1}{M-m} \sum_{i=1}^{M-m} \frac{\sum_{n=n_1}^{n_2} p_i(n) p_{i+m}(n)}{\sqrt{\sum_{n=n_1}^{n_2} p_i^2(n) p_{i+m}^2(n)}}, \tag{2.45}$$

where p is the delayed signal, n is the depth sample index, m is the distance, or lag, in number of elements between two point on the aperture. The sum over n results in a correlation over a given kernel size, $n_2 - n_1$ of pixels. The short lag spatial coherence, is calculated as the sum over the first M lags,

$$b_{\mathrm{SLSC}} = \sum_{M}^{M} \hat{R}(m). \tag{2.46}$$

Thus, notice that b_{SLSC} is an image of the coherence and not the backscattered signal amplitude as with DAS and MV. The SLSC is a visualization of the spatial coherence of backscattered ultrasound waves, building upon the theoretical prediction of the van Cittert-Zernike (VCZ) theorem . The implications of the VCZ theorem for pulse-echo ultrasonic imaging was discussed by Mallart and Fink 1994, 1991.

Some of the adaptive methods have user settable parameters. For the results presented in this chapter we used the same parameteres as in **Paper VI**.

> For MV, L was set to 50% of the active receive channels, $K = 1.5\lambda$, and a diagonal loading factor of $\Delta = 1/100$ was used as suggested in (Synnevåg, Austeng, and Holm 2009). The number of eigenvectors used in EBMV was selected adaptively using the eigenvectors with eigenvalues larger than $\delta = 0.5$ times the maximum eigenvalue as suggested in (Asl and Mahloojifar 2010). For GCF the value $M_0 = 2$ was used as suggested in (Li and Li 2003). For PCF $\gamma = 1$ was chosen as suggested in (Camacho, Parrilla, and Fritsch 2009).

2.7.8 Categorizing adaptive beamformers

With the myriad of adaptive techniques, a way of categorizing them could be useful. We will suggest two different categorizations.

Categorization I : Coherence and non-coherence adaptive beamforming

Coherence F-DMAS, CF, GCF, PCF and SLSC

Non-coherence MV and EBMV.

The first categorization is based on if the beamformers exploit the coherence, or in a more general term similarity, of the wavefront received over the aperture. The connection between F-DMAS and coherence is not obvious. However, in **(Paper V)** we studied this in detail and concluded that "Being largely influenced by the signal coherence, the F-DMAS beamformer appears as an intermediate between the DAS beamformer and beamformers using coherence factor weighting". The CF, GCF, and PCF all weight the DAS image with a weight directly dependent on the signal coherence. In CF this is calculated from the signal directly. In GCF as a generalization of the CF through the Fourier spectra over the aperture. In PCF the coherence is measured as similarity based on the standard deviation of the phase over the aperture. The SLSC calculates the coherence based on a normalized correlation of the signal over the aperture. The MV and EBMV, on the other hand, are calculating an adaptive weight set that is trying to suppress unwanted off-axis signals based on the minimization problem posed. Thus, they are not "measuring" the coherence as the other beamformers, and we categorize them as non-coherence beamformers.

Categorization II : Adaptive element vs adaptive image weights

Element weights MV, EBMV, and F-DMAS

Image weights CF, GCF and PCF.

The second categorization is based on where the "adaptiveness" is applied. Both the MV and EBMV calculate an adaptive weight set that is applied in the summation of the signal. The F-DMAS does not calculate a weight set directly, but we will consider weighting the element signals with each other as some kind of element weighting.

The CF, GCF, and PCF are all weighting the DAS image with an *image weight* based on some coherence estimate, and thus, the adaptiveness is applied as an image weighting. The issue with categorization II is that the SLSC does not fit within this definition of categories since it displays the coherence directly and not multiplied with the image.

There do exist publications where adaptive methods are combined across these categories. For example, when coherence image weights are applied as a weighting to MV images (Chau, Lavarello, and Dahl 2016), thus there truly is a myriad of adaptive beamformers.

2.8 Post processing

Whether we have the image b_{DAS} created by the conventional DAS image as in equation (2.20). Or we have an image created by an adaptive beamformer such as the b_{MV} from the minimum variance beamformer equation (2.29), there are some final stages before the image is displayed on the screen.

2.8.1 Detecting the envelope

From Section 2.5, we know that if we have the analytical signal or the IQ-signal we can simply detect the envelope A of the signal by taking the absolute value $A = |b|$, where b for example is b_{DAS} from equation (2.20). If we have used the RF signal through the beamforming chain, the envelope can be detected by generating the analytical signal of the beamformed data, b. Thus, creating a complex signal by using the Hilbert transform of the data as the imaginary component. However, the number of pixels in the axial (z) direction is then very important. The signal in the axial direction needs to be well sampled to avoid artifacts in the image introduced from the Hilbert transform. The number of samples in the axial direction (z) can be reduced if one use the analytical signal through the processing chain, since the Hilbert transform is then taken on the well sampled RF channel data. The number of axial pixels can also be reduced if one use the IQ-signal.

2.8.2 Log compression

Ultrasound images are, at least in the research literature, usually shown in a logarithmic scale. Thus, the final stage is to do a logarithmic compression of, for example, the DAS signal so that

$$B_{\text{DAS}} = 20\log_{10}(A_{\text{DAS}}) = 20\log_{10}(|b_{\text{DAS}}|), \tag{2.47}$$

where A_{DAS} is the signal envelope and b_{DAS} (assuming IQ or analytical signal) is the coherent combination of the delayed signals as described in equation (2.20). The exception from the log compression is for example SLSC images that are for some applications shown in the natural scale (Lediju Bell et al. 2013). The SLSC image is an image of the coherence directly.

2.8.3 The dynamic range

The logarithmically compressed images are often normalized so that the maximum value in the image is displayed as 0 dB. The dynamic range of the image is then the lowest value displayed in the image. A common dynamic range is from 0 dB to -60 dB, resulting in an image as displayed in Figure 2.29a. In Figure 2.29b, we have displayed the same image but using a dynamic range of 0 dB to -40 dB. The two images are an illustration of how simply changing the dynamic range can result in an image where the apparent contrast, in terms of the hypoechoic cyst, seems to be improved. (**Paper VII**) is an in-depth investigation into the effects adaptive beamforming has on the dynamic range with emphasis on how this affects the estimated contrast.

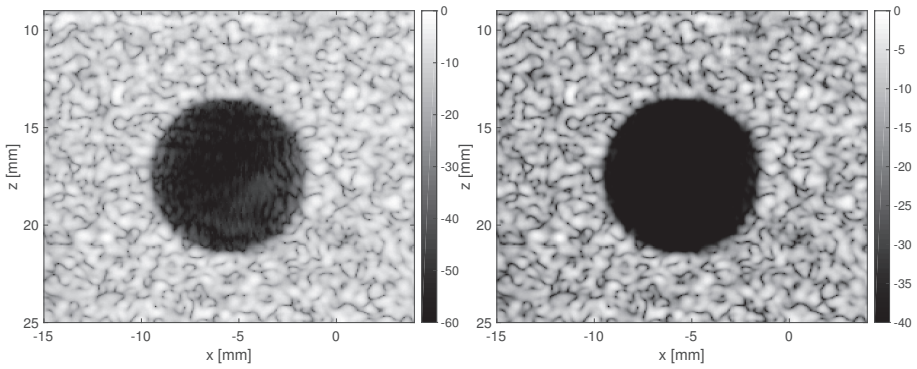

(a) 60 dB dynamic range (b) 40 dB dynamic range

Figure 2.29: Two images illustration how changing the dynamic range can result in an image where the apparent contrast, in terms of the hypoechoic cyst, seems to be improved. (a) have 60 dB dynamic range, while (b) have 40 dB dynamic range. Data from **Paper VII**.

2.8.4 Further post processing

In a clinical scanner, the final stages of the processing chain of a B-mode ultrasound image would now contain different image processing algorithms, such as speckle reduction. We will, however, stop our description of the medical ultrasound processing chain here.

2.9 Speckle statistics

If we are imaging a scene of enough randomly distributed small scatterers reflecting the transmitted ultrasound wave, see Section 2.2, the resulting image is of a *speckle pattern*. The speckle pattern is considered to be *well developed* if the number of scatterers per resolution cell is larger than 10 (Wagner et al. 1983). An image simulated in Field II (Jensen 1996; Jensen and Svendsen 1992) of such a scenario is shown in Figure 2.30, with a few tricks to obtain a uniform field of view detailed in (Rindal 2018).

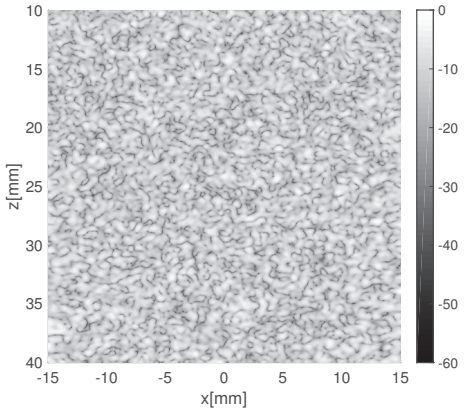

Figure 2.30: A STAI image of well developed speckle simulated in Field II.

According to (Wagner et al. 1983), well developed speckle results in an ultrasound pressure field that are circular Gaussian or more precisely a circularly-symmetric Normal distribution. This means that e.g. the analytical signal, both the real and imaginary parts, will follow a normal Gaussian distribution. This is confirmed in Figure 2.31, where we see that the estimated PDF for both the real and imaginary parts of the signal follows the theoretical normal Gaussian distribution.

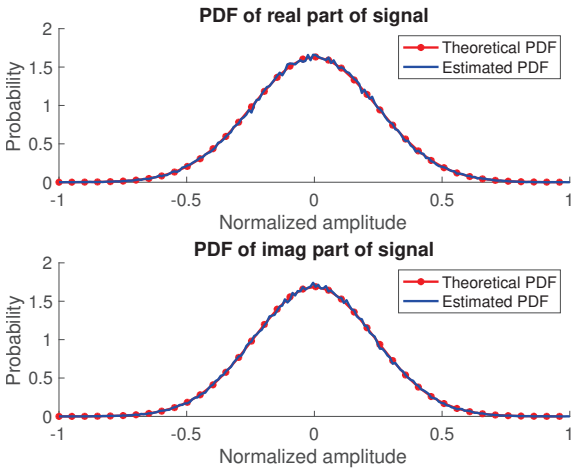

Figure 2.31: Estimated PDF of the real and imaginary part of the analytical signal plotted together with the theoretical normal Gaussian distribution.

The amplitude of the envelope follows a Rayleigh distribution with the theoretical probability function (Wagner et al. 1983)

$$f_{\text{Rayleigh}} = \frac{A}{\beta^2} e^{\frac{-A^2}{2\beta^2}}, \tag{2.48}$$

where A is the envelope amplitude and β is the scaling parameter than can be found from the variance of a Rayleigh distribution $\sigma^2 = \frac{4-\pi}{2}\beta^2$. The signal to noise ratio, SNR $= \frac{\mu}{\sigma} = 1.91$, where μ is the mean of the envelope, and σ is the standard deviation. The estimated SNR of the image in Figure 2.30 was 1.91 fitting the theoretical distribution very well, as we can see from Figure 2.32. Here we have plotted the estimated PDF together with the theoretical Rayleigh distribution. The Rayleigh distribution belongs to the family of Rician distributions.

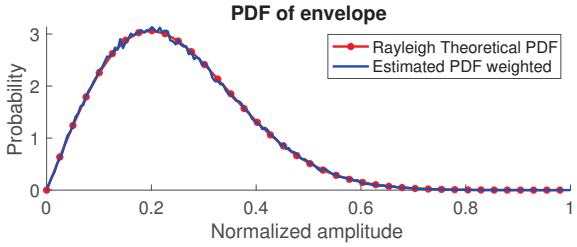

Figure 2.32: The estimated PDF of the envelope together with the theoretical Rayleigh distribution.

It is worth to mention that it is seldom large enough uniform areas in the body to create the well developed speckle. Often stronger targes or specular reflections will occur and result in different statistical distributions. However, for example the thyroid and the blood is known for having well developed speckle patterns.

The image in Figure 2.30 was created by the conventional DAS beamformer. In **(Paper VIII)**, we investigated the speckle statistics of several adaptive beamformers and the influence on conventional contrast metrics. We showed that most adaptive beamformers do not follow the same speckle statistics as DAS. In **(Paper V)** the image amplitude and speckle statistics of the F-DMAS beamformer were investigated in detail. In **(Paper IX)**, we argue that the alteration of the speckle statistics by adaptive beamformers is invalidating the conventional contrast metrics. We also use the known speckle statistics of DAS to derive analytical expressions of the contrast metrics for DAS.

2.10 Evaluation of image quality – metrics

By being introduced to the myriad of adaptive beamformers, we might have gained some insight into the author's motivations for using the word *curse* in the title of this thesis. The *curse*, in the author's opinion, is that software beamforming is so flexible that algorithms mostly optimizing the evaluation metrics, may be developed. More specifically, we, quite baldly, claim in **(Paper VII)** that "The results presented here expose a dangerous weakness of our image quality metrics. This weakness must be remediated. We must lay the groundwork upon which we build the new techniques. A new metric for contrast must be sought, one that is immune to dynamic range transformations, and help us assess the relevance of present and future beamforming techniques."

To understand how we got there, let's first have a look at the contrast metrics commonly used in ultrasound imaging.

2.10.1 Contrast

In **(Paper VII)**, we summarized the current status of contrast measurements in ultrasound images:

> No clear consensus exists yet on how to measure the contrast of ultrasound images. Perhaps the most widespread definition (Lediju et al. 2011; Matrone, Savoia, and Magenes 2015; Zhao et al. 2017) is the one in (Smith, Lopez, and Bodine 1985),
>
> $$\mathrm{CR} = \frac{\mu_{\mathrm{ROI}}}{\mu_{\mathrm{B}}}, \tag{2.49}$$
>
> where $\mu = E\left\{|b|^2\right\}$ is the expected value of the power of the beamformed signal, in linear scale, over a certain region; and where ROI and B denote, respectively, a region of interest and a background region. If the signal power is proportional to the back-scattering coefficient, which is the case for speckle signals beamformed with DAS, then CR is proportional to the ratio of the particle concentration in both regions. CR, often referred to as contrast ratio, can be expressed in logarithmic scale as,
>
> $$\mathrm{CR[dB]} = 10\log_{10}\mathrm{CR}. \tag{2.50}$$
>
> Detection probability not only depends on the mean value of the signal power but also on its variance. An alternative measure of contrast can be found in (Patterson and Foster 1983), a measure that became later known as the contrast-to-noise ratio
>
> $$\mathrm{CNR} = \frac{|\mu_{\mathrm{ROI}} - \mu_{\mathrm{B}}|}{\sqrt{\sigma^2_{\mathrm{ROI}} + \sigma^2_{\mathrm{B}}}}, \tag{2.51}$$
>
> where $\sigma = \sqrt{E\left\{(|b|^2 - \mu)^2\right\}}$ is the standard deviation of the power of the beamformed signal, in linear scale. CNR is an estimate of the detection

“

probability of a lesion. In particular for the case of circularly-symmetric Gaussian distributed signals, which is the case of speckle signals beamformed with DAS, CNR is bounded to the interval $[0, 1]$. This metric has been used by many authors (Lediju et al. 2011; Matrone, Savoia, and Magenes 2015; Shin and Huang 2017; Zhao et al. 2017).

Even though the expressions (2.49) and (2.51) were originally proposed to be applied to signal power in natural units, many authors have chosen to insert log-compressed values in them, effectively defining the alternative metrics:

$$\mathrm{CR_{LC}[dB]} = |\tilde{\mu}_{\mathrm{ROI}} - \tilde{\mu}_{\mathrm{B}}|, \tag{2.52}$$

where $\tilde{\mu} = E\{20\log_{10}(|b|)\}$ is the expected value of the log-compressed values within the ROI and B region, and

$$\mathrm{CNR_{LC}[dB]} = \frac{|\tilde{\mu}_{\mathrm{ROI}} - \tilde{\mu}_{\mathrm{B}}|}{\sqrt{\tilde{\sigma}^2_{\mathrm{ROI}} + \tilde{\sigma}^2_{\mathrm{B}}}}, \tag{2.53}$$

where $\tilde{\sigma} = \sqrt{E\{(20\log_{10}(|b|) - \tilde{\mu})^2\}}$ is the standard deviation of the log-compressed signal within the ROI and B region. We include the subindex LC to denote the metrics computed on log-compressed values.

Although (2.52) is similar to (2.50), they are not identical since $10\log_{10}\left(E\left\{|b|^2\right\}\right) \neq E\{20\log_{10}(|b|)\}$. CNR and $\mathrm{CNR_{LC}}$ take completely different values, and cannot be directly compared. Although both are thought to be estimates of the lesion detection probability, $\mathrm{CR_{LC}}$ can take values larger than 1, even for speckle signal beamformed with DAS. Several authors (Asl and Mahloojifar 2010; Krishnan, Rigby, and O'Donnell 1997; Mehdizadeh et al. 2012; Nguyen and Prager 2018; Shin and Huang 2017) have chosen (2.52) and (2.53) to quantify contrast.

In some articles (Camacho, Parrilla, and Fritsch 2009; Li and Li 2003; Ozkan, Vishnevsky, and Goksel 2018; Szasz, Basarab, and Kouamé 2016b; Zhao et al. 2017; Zhuang, Rohling, and Abolmaesumi 2018) it is not explicit whether logarithmic or natural units have been used. In some others variations of the classical definitions are used (Asl and Mahloojifar 2010; Krishnan, Rigby, and O'Donnell 1997; Ozkan, Vishnevsky, and Goksel 2018).

”

The consequences of the lack of consensus on how to measure ultrasound images are discussed in detail in **(Paper VI, VII, VIII)** and **Paper IX**. Where we claim that adaptive beamformers are invalidating the conventional contrast metrics, which can be seen as one of the *curses* of software beamforming. Fortunately, a remedy to the *curse* is presented in **Paper IX** where we present an improved contrast metric immune to the unwanted effects from adaptive beamformers, namely the generalized contrast-to-noise ratio (GCNR).

2.10.2 Resolution

For completeness, we will have a brief look at how the resolution is evaluated in the medical ultrasound research literature. There exist multiple definitions of resolution ranging from the −3dB Rayleigh resolution criteria (Rayleigh 1879), to the Sparrow resolution defined as where the saddle point between the two peaks first develops - thus being a measure on separability. A brief review shows that many authors tend to use the FWHM (-6 dB) (Liebgott et al. 2016; Matrone, Savoia, and Magenes 2015), while others use some measure of separability (Camacho, Parrilla, and Fritsch 2009; Jensen and Austeng 2014) while some use both (Diamantis et al. 2019). We will have a brief look at both.

2.10.3 Resolution as the width of the point spread function

To measure resolution the convention is to image a single scatterer, resulting in an image of the point spread function (PSF) of the system and measure the full with half maximum (FWHM). The FWHM is equivalent to measuring the mainlobe width of the PSF at ≈-6 dB. In Section 2.3, we saw how the FWHM made perfect sense when comparing the resolution between a wide linear array and a narrower phased array. However, the FWHM is often used to evaluate the resolution of adaptive beamformers, and we will look into some consequences.

In Figure 2.33, we have plotted the mainlobe of the PSF resulting from all the adaptive beamformers mentioned in Section 2.7, except SLSC. We have simulated a single point scatterer in Field II (Jensen 1996; Jensen and Svendsen 1992) illuminated by a single plane wave. The measured FWHM is indicated above the plot of the mainlobe, and in the bars below.

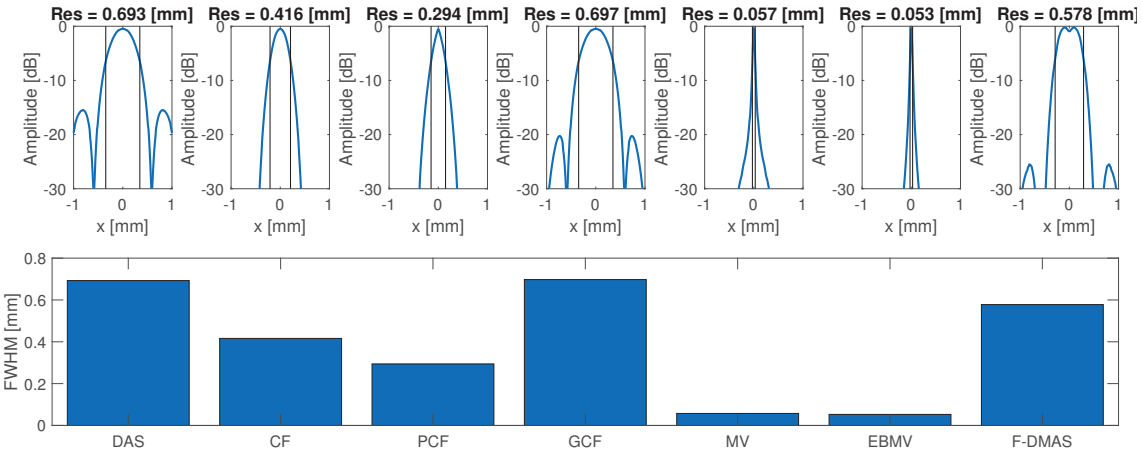

Figure 2.33: Full Width Half Maximum (FWHM) measured from a single point scatterer imaged by a plane wave transmission and reconstructed using the DAS, CF, PCF, GCF, MV, EBMV and F-DMAS beamformer.

Smaller FWHM means improved resolution if we define resolution to be an improved (narrower) reconstruction of the small point scatterer imaged. Judging by the results in Figure 2.33, all the adaptive beamformers tested, except GCF, have improved resolution compared to DAS.

2.10.4 Resolution as separability

Improved resolution should result in improved separation of closely located targets. Let us now, instead of using the FWHM as a measure of resolution, define resolution to be the ability to resolve two scatterers. In Figure 2.34, we show in (a) the resulting images using the adaptive beamformers imaging two point scatteres separated by 1 mm. The plot below the B-mode images is the lateral line through the center of the points. The red dashed line is indicating -6 dB. When the scatteres are separated by 1 mm, all the beamformers expect GCF are able to detect both. Where detection is defined as a local minimum between the peaks of more than -6 dB.

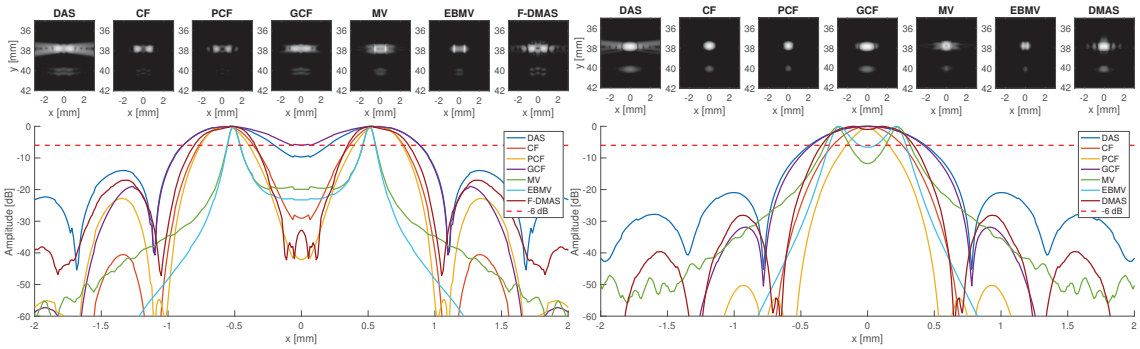

(a) Point scatterers separated by 1 mm

(b) Point scatterers separated by 0.5 mm

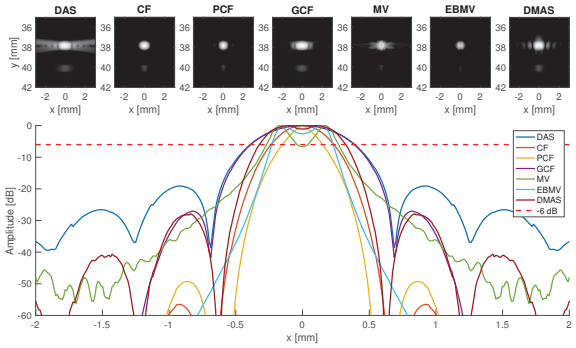

(c) Point scatterers separated by 0.4 mm

Figure 2.34: Images of two point scatteres separated by 1, 0.5 and 0.4 mm in (a), (b) and (c) respectively. The plot below the B-mode images are the lateral line through the center of the points. The red dashed line is indicating -6dB.

In Figure 2.34b only 0.5 mm is separating the point scatterers. Notice then that only the MV and EBMV are able to separate the two point scatterers. At 0.4 mm separation, in Figure 2.34c only the MV beamformer is able to separate the two points. When doing this study on more images with separation between the two point scatterers at 4, 2, 1, 0.5, 0.44 and 0.4 mm, we get the results in 2.35. In the top, we see the separability, measured as the lowest point between the point scatterers for all beamformers with the dashed red line indicating the

-6 dB limit.

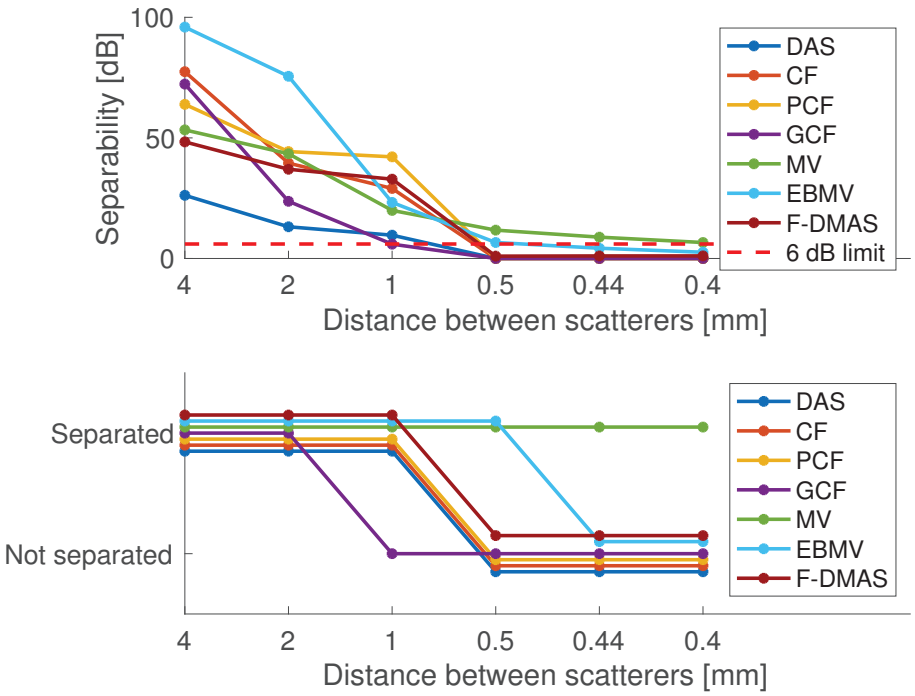

Figure 2.35: The measured separability, measured as the lowest point between the point scatterers, of two point scatteres separated by 4, 2, 1, 0.5, 0.44 and 0.4 mm in (a). The dashed red line indicate the 6dB separation. In (b) we have thresholded on the 6 dB limit, into separated or not separated.

In the bottom plot, we have, based on the -6 dB limit, divided the result from the beamformers into separated or not separated for all distances. Interestingly, only the MV and EBMV beamformer have better separability than DAS. Even though when we used the FWHM as the definition of resolution, all beamformers except GCF improved the FWHM compared to DAS. This short investigation shows some interesting results regarding the claimed improved resolution resulting from some adaptive beamformers. If the improved resolution, as measured by the FWHM does not result in improved separability, it is relevant to review the relevance of FWHM as a metric for resolution. Also, if we tie our preliminary results on resolution improvement with our previous categorization of the adaptive beamformers we can hypothesize an interesting connection. The beamformers categorized to the *image weight* category, according to categorization II in Section 2.7.8, have an improved FWHM. But they do not have an improved separability compared to DAS. This makes, of course, sense since the adaptive beamformers belonging to the *image weight* category is taking the DAS image and multiplying it with an adaptive weight. This will, of course, result in narrower FWHM, in the same way as simply raising the DAS image to a power > 1. However, simply raising the image to a power does not yield new information. Interestingly, this did not apply to the GCF in our tested scenario. Whether multiplying an image with an adaptive weight yields improved information in terms of resolutions remains to be investigated in depth. But our brief investigation here shows that

one can question the ability to resolve scatterers. Thus, we have identified that as with contrast, there seems to be no consensus on how to measure resolution in medical ultrasound imaging. Similar to the thorough investigation into contrast and contrast metrics of adaptive beamformers, as we have done in the published papers, needs to be done for resolution. However, such an investigation into resolution is not done in this thesis and remains to be further studied.

Chapter 3

Summary of Publications

This chapter provides a brief motivation and the outcome of the published papers included in this thesis. For convenience, the figure presented in the introduction chapter is included to highlight which part of the software beamforming processing chain the publications in this thesis relate.

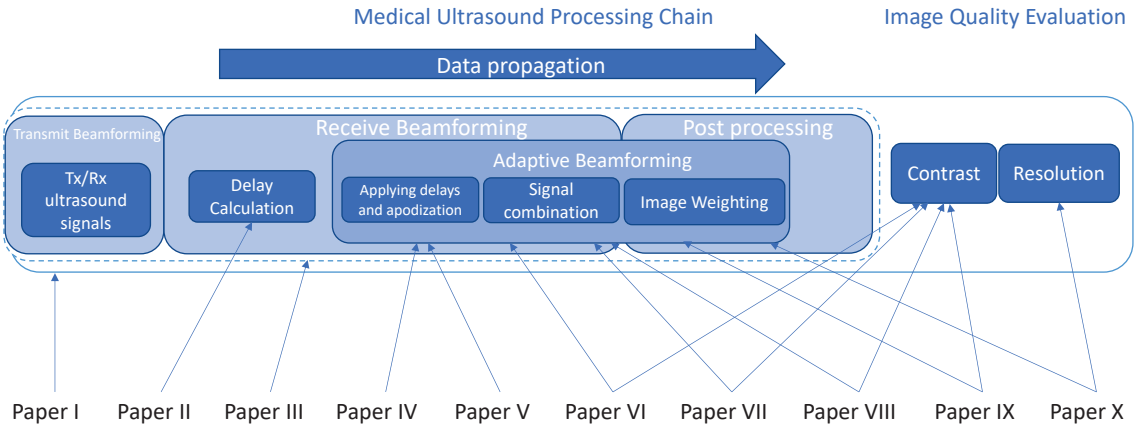

Figure 3.1: Graphical illustration of the software beamforming reconstruction chain in medical ultrasound imaging, also illustrating which area of the processing chain the papers in this thesis relate.

Paper I: The UltraSound ToolBox

Rodriguez-Molares*, A., Rindal*, O. M. H., Bernard, O., Nair, A., Lediju Bell, M. A., Liebgott, H., Austeng, A., and Løvstakken, L. 2017. "The UltraSound ToolBox" *IEEE International Ultrasonics Symposium, IUS:* 1–4. doi: 10.1109/ULTSYM.2017.8092389 *These authors are shared first authors with equal contributions.

The UltraSound ToolBox (USTB) is an open source processing framework for ultrasound signals implemented in MATLAB and C++. The motivation behind the USTB is to provide tools to compare ultrasound processing techniques and share data to aid the dissemination of research results. The USTB consists of two main parts; an ultrasound file format (UFF) and a framework for processing of ultrasound signals (processing classes). The UFF has later developed into a UFF initiative defining a common file format agreed upon by multiple research groups (Bernard et al. 2018). The USTB is an implementation of the entire software beamforming processing chain including implementations of many state of the art adaptive beamforming algorithms. The USTB was used to create the results for most of the papers in this thesis with the implementations and data available through the website http://www.ustb.no.

Paper II: A simple, artifact-free, virtual source model

Rindal, O. M. H., Rodriguez-Molares, A., and Austeng, A. 2018. "A simple, artifact-free, virtual source model". *IEEE International Ultrasonics Symposium, IUS*: 1–4. doi:10.1109/ULTSYM.2018.8579944

Retrospective beamforming is a technique that exploits the full overlap between transmit beams. This results in images with higher image quality, both in terms of contrast and resolution, since a syntethic focus is reconstructed in the overlapping region. Alternatively, one can use retrospective beamforming to obtain the same quality as conventional scan line imaging but with fewer transmits, thus getting a higher frame rate. Retrospective beamforming is a relatively new imaging technique, which can be implemented using software beamforming. The spherical delay model is conventionally used in the research literature. The spherical model places a virtual source in the foci of the transmitted beam. However, the spherical model results in a discontinuity to the side of the foci. This discontinuity results in an artifact in the final images. One solution to this artifact was published in (Nguyen and Prager 2016), where a unified delay model was presented. Nguyen and Prager did a thorough analysis of the wave propagation and presented a delay model that interpolates the delay values between the converging and diverging regions occurring before and after the foci. The unified delay model resolves the discontinuity and removes the resulting artifact. However, the unified model is cumbersome to implement and quite resource demanding. In this paper, we presented a hybrid delay model that combines the propagation of spherical and plane waves. We assume that the wave propagates as a plane wave in a small region around the foci, and outside this region we use the conventional spherical delay model. The presented model is fast, easy to implement, and removes the unwanted artifact. The presented delay model is now used in the USTB. The implementations and data used in this publication are available through the USTB at http://www.ustb.no/publications/paper_II.

Paper III: Wireless, Real-Time Plane-Wave Coherent Compounding on an iPhone - a feasibility study

Palmer*, C. L. and Rindal*, O. M. H. 2019. "Wireless, Real-Time Plane-Wave Coherent Compounding on an iPhone - a feasibility study" *IEEE Transactions on Ultrasonics, Ferroelectrics, and Frequency Control* (PP): 1–11. doi: 10.1109/TUFFC.2019.2914555 *These authors are shared first authors with equal contributions.

This paper demonstrates one of the main benefits of software beamforming; that any high-performance processing device can do medical ultrasound reconstruction. In this paper, we show that a range of the newer generation iPhones and iPads have the processing power to implement the full software beamforming processing chain. We demonstrated this by transferring channel data wirelessly to an iPhone or an iPad and process in the GPU with real-time frame rates of 60 FPS for the iPhones and 90 FPS for the iPad for a single PW transmission. A frame rate of e.g 13 FPS was achieved when coherently compounding 7 PW transmissions. PW transmissions were chosen since a full image can be reconstructed from a single transmission, while higher image quality is achieved when coherently compounding more transmissions. Thus, a tradeoff

between image quality and frame rate is achieved. The channel data was recorded and transmitted wirelessly in real-time using a Verasonics Vantage 256 scanner transmitting through a wireless access point. Interestingly, the bottleneck was not the processing power of the iPad/iPhone. The bottleneck in the system was the serialization of the channel data into the protobuf transmitted over the network. The main limitation was the serialization library implemented in Java that had to be called from MATLAB. Real-time Access to the channel data in a lower-level language than MATLAB could speed up the serialization. A demo video of the results is available at https://youtu.be/oN8cwysGxyM. The results hypothesize that hand-held systems will move to software beamforming, potentially lowering the price of the system since off-the-shelf devices can be used.

Paper IV: Double Adaptive Plane-Wave Imaging

Rindal, O. M. H. and Austeng, A. 2016. "Double Adaptive Plane-Wave Imaging". *IEEE International Ultrasonics Symposium, IUS*: 1–4. doi:10.1109/ULTSYM.2016.7728906

The flexibility of software beamforming can be exploited as we show in this paper where we presented an implementation of double adaptive plane wave beamforming. Meaning, that we first do conventional minimum variance beamforming applied to the receive channels of each plane wave image as in (Holfort, Gran, and Jensen 2008). The first adaptive step is followed by a minimum variance weighting of the coherent compounding as suggested in (Austeng et al. 2011). This paper was a contribution to Plane-wave Imaging Challenge in Medical UltraSound (PICMUS) arranged at the IEEE IUS 2016. The presented method showed a significant improvement to the FWHM and CNR compared to conventional DAS.

Paper V: Signal Coherence and Image Amplitude With the Filtered Delay Multiply and Sum Beamformer

Prieur, F., Rindal, O. M. H., and Austeng, A. 2018. "Signal Coherence and Image Amplitude With the Filtered Delay Multiply and Sum Beamformer". *IEEE Transactions on Ultrasonics, Ferroelectrics, and Frequency Control* 65 (7): 1133–1140. doi:10.1109/TUFFC.2018.2831789

The Filtered-Delay-Multiply-And-Sum (F-DMAS) adaptive algorithm is a somewhat recent adaptive beamforming algorithm. Despite the popularity and numerous publications using the beamformer, an understanding of why this method reports improved contrast and resolution compared to conventional DAS was missing. In this paper we presented a theoretical study of the amplitude statistics of the F-DMAS compared to the DAS beamformer backed up with numerical simulations and experimental data. The difference between the DAS and F-DMAS can partly be explained by our results showing that F-DMAS is more dependent on the coherence of the signal than DAS. This was, to the author's knowledge, the first time it was shown that the F-DMAS algorithm is exploiting the coherence in the ultrasound signal, and can thus be categorized as a coherence beamformer. The implementations and data used in this publication are available through the USTB at http://www.ustb.no/publications/paper_V.

Paper VI: The Dark Region Artifact in Adaptive Ultrasound Beamforming

Rindal, O. M. H., Rodriguez-Molares, A., and Austeng, A. 2017. "The Dark Region Artifact in Adaptive Ultrasound Beamforming". *IEEE International Ultrasonics Symposium, IUS*: 1–4. doi:10.1109/ULTSYM.2017.8092255

The *dark region artifact* (DRA) is an unwanted artifact created by some adaptive beamforming methods. The artifact occurs because some adaptive beamformers fail to estimate which signals originate in the mainlobe, and which signals originate from sidelobes. If a target, for example, a point scatterer or hypoechoic cyst, is sufficiently stronger than the surrounding area the dark region artifact occurs. Among the beamformers tested in the paper, only the DAS and MV beamformers are not affected by the DRA. The CF, GCF, PCF, and F-DMAS are affected by the DRA. This is because a strong signal received by a sidelobe dominates the signal received in the mainlobe resulting in wave-fronts that are non-parallel to the receiving aperture. This, therefore, creates low coherence. The EBMV algorithm aims at estimating and dividing the spatial covariance matrix into a signal and a noise subspace. However, when the delayed wave-field have wave-fronts that are not parallel to the receiving aperture, the signal space estimated might not contain the steering vector $a = 1$ entirely. Therefore, the projected weights will not fulfill the distortionless response constraint completely, with the consequence of a reduced output amplitude, resulting in the DRA. The DRA results in wrongly measured contrast and black holes in the speckle. The implementations and data used in this publication are available through the USTB at http://www.ustb.no/publications/paper_VI.

Paper VII: The Effect of Dynamic Range Alterations in the Estimation of Contrast

Rindal, O. M. H., Austeng, A., Fatemi, A., and Rodriguez-Molares, A. 2019. "The Effect of Dynamic Range Alterations in the Estimation of Contrast". *IEEE Transactions on Ultrasonics, Ferroelectrics, and Frequency Control* PP:1–11. doi:10.1109/TUFFC.2019.2911267

Within the published literature of medical ultrasound beamforming a myriad of publications exists on adaptive beamformers claiming improved contrast. Contrast is conventionally measured by the contrast ratio (CR) and the contrast-to-noise-ratio (CNR). In the paper, we present a literature search showing that there is no consensus on how to measure contrast in ultrasound images. Many different metrics and variations of CR and CNR have been used. Also, contrast has been measuring on the image signals both before and after log compression yielding quite different results. Further, by introducing a "gray level transform" beamformer we claim and show in the paper that the estimation of CR and CNR is affected by dynamic range alterations. A main contribution in the paper is to introduce gradients to investigate whether a beamformer is alternating the dynamic range. For the simulated data, both an axial and a lateral gradient were used, but for the experimental data only a lateral gradient was used. The gradients allowed us to introduce the *dynamic range test*, giving a quantitative measure on how much a beamformer is alternating the dynamic

range. We show that the amount of dynamic range stretching correlates very well, $R^2_{\text{adj}} = 0.88$ for the simulated and $R^2_{\text{adj}} = 0.96$ for the experimental data, with the CF improvements. The study tested the DAS, MV, EBMV, F-DMAS, CF, GCF and, PCF beamformer, and only the DAS and MV were found not to alternate the dynamic range notably. The F-DMAS was slightly alternating the dynamic range. While EBMV, F-DMAS, CF, GCF, and PCF had quite large alterations. We claim, based on the results that the classical contrast metrics C and CNR are invalidated by modern adaptive beamformers, and that a new improved metric immune to dynamic range alterations are needed. The implementations and data used in this publication are available through the USTB at http://www.ustb.no/publications/paper_VII.

Paper VIII: The Influence of Speckle Statistics on Contrast Metrics in Ultrasound Imaging

Hverven, S. M., Rindal, O. M. H., Rodriguez-Molares, A., and Austeng, A. 2017b. "The Influence of Speckle Statistics on Contrast Metrics in Ultrasound Imaging". *IEEE International Ultrasonics Symposium, IUS*: 1–4. doi:10.1109/ULTSYM.2017.8091875

It is well known that conventional DAS imaging well developed speckle results in Rayleigh distributed speckle statistics. In this publication, we show that some adaptive beamformers alter the speckle statistics. Since the statistical distribution affects the contrast metrics used to evaluate the beamformers, it is important to be aware of how the beamformer is altering the speckle statistics. If not, the alterations of the speckle statistics open up to cherry picking contrast metrics.

Paper IX: The Generalized Contrast-to-Noise ratio

Rodriguez-Molares, A., Rindal, O. M. H., D'hooge, J., Måsøy, S.-E., Austeng, A., Lediju Bell, M. A., and Torp, H. 2019. "The Generalized Contrast-to-Noise ratio". *Prepared for submission to IEEE Transactions on Ultrasonics, Ferroelectrics, and Frequency Control*: 1–12

This paper answers the call for an improved contrast metric that is immune to the dynamic range alterations, and the alteration of speckle statistics. In this paper, we present the Generalized-Contrast-to-Noise-Ratio (GCNR) which is a quantitative measure on the probability of detecting a region with different intensity by an ideal observer. For example the GCNR of a hypoechoic cyst is the percentage of pixels that are correctly classified as the cyst. The GCNR of several state-of-the-art adaptive beamforming methods are tested for different signal-to-noise ratios. Even though many of the methods improve the conventional CR and CNR metrics, our results reveal that some methods (CF, PCF) actually worsen the probability of lesion detection with an absolute decrease in GCNR. While other methods (GCF, F-DMAS) only improve it slightly. Only one of the tested methods (SLSC) produced a relevant increase in detection probability with an absolute increase in GCNR. It is important to point out that this paper, first and foremost, presents a new metric and is not aiming at benchmarking the methods. The results are based on both simulated and experimental data with good correlation in the simulated and experimental results. The paper

presents the theoretical derivation of the GCNR. Analytical expressions for the DAS beamformer for both CR and CNR are also derived.

Paper X: Hypothesis of Improved Visualization of Microstructures in the Interventricular Septum with Ultrasound and Adaptive Beamforming

Rindal, O. M. H., Aakhus, S., Holm, S., and Austeng, A. 2017. "Hypothesis of Improved Visualization of Microstructures in the Interventricular Septum with Ultrasound and Adaptive Beamforming". *Ultrasound in Medicine and Biology* 43 (10): 2494–2499. doi:10.1016/j.ultrasmedbio.2017.05.023

This paper explores applications of the improved resolution of Capon's minimum variance beamformer. We used the MV beamforming technique on in vivo cardiac ultrasound data creating images from three different views of a heart: the parasternal short-axis, parasternal long-axis and apical four- chamber views. The images reveal that the improved resolution of the MV beamforming technique produces images with an improved lateral resolution, resulting in a better-resolved speckle structure compared with that of conventional DAS beamforming. Myocardial microstructure, that is, the architecture of cardiomyocytes, connective tissue fibers, blood vessels and neural tissue, contributes to the reflected ultrasound data. Further studies are needed to identify the efficiency of MV compared with DAS in terms of identifying pathological alterations in this microstructure.

Chapter 4

Discussion

The main contributions in this thesis are

- The UltraSound ToolBox (USTB, http://www.USTB.no), which is an open source implementation of the software beamforming processing chain in medical ultrasound imaging. The USTB includes many of the state-of-the-art beamforming techniques and algorithms facilitating the comparison of techniques and dissemination of research results. The USTB is a shared project between several research institutions. However, in practice, most of the development is done by Alfonso Rodriguez-Molares at NTNU (The Norwegian University of Science and Technology) and I. The two of us are also administering the project.

- The hybrid delay model is a simple artifact-free virtual source model that removes an unwanted artifact from retrospective beamforming (RTB) and multiple line acquisition (MLA) images. Compared to other published solutions, our hybrid model is less computationally expensive and easier to implement.

- The demonstration of the perhaps most significant benefit of software beamforming: Medical image reconstruction, beamforming, can be implemented on off-the-shelf devices such as an iPhone.

- The double adaptive plane-wave imaging algorithm successfully demonstrating the flexibility of software beamforming.

- Insight into the state of the art algorithms such as the Filtered Delay and Sum Beamformer (F-DMAS). Demonstrating that F-DMAS can be considered a coherence based beamformer.

- Identified and coined the term *dark region artifact* for an unwanted artifact appearing next to acoustically strong targets for some adaptive beamforming algorithms.

- Showed that some state of the art adaptive algorithms alter the dynamic range of the image. The alteration effectively invalidates the conventional contrast metrics contrast ratio (CR) and contrast to noise ratio (CNR).

- Pointed out that there is no clear consensus on how to measure contrast in ultrasound images. Multiple definitions of CR and CNR are used in the research literature.

- Provided the *dynamic range test*, comprising data and code publicly available through the USTB. The dynamic range test allows anyone to check if their algorithm alters the dynamic range of the image.
- Investigation of the speckle statistics of adaptive beamformers and how this influences the conventional contrast metrics in ultrasound imaging.
- Introduced an improved contrast metric, the Generalized Contrast-to-Noise ration (GCNR), which is immune to dynamic range alterations, that can be used on any type of data regardless of signal nature and units and results in a value that has physical meaning. The GCNR measures the percentage of pixels that are correctly classified by an ideal observer.
- Investigated benefits from adaptive beamforming in in-vivo images. Specifically hypothesizing that the minimum variance beamformer improves the visualization of microstructures in the interventricular septum of the heart.

As seen from the main contributions, this thesis has investigated various aspects of the software beamforming processing chain in medical ultrasound imaging. Especially the in-depth evaluation and comparison of adaptive beamforming techniques as well as suggesting methods and metrics to evaluate the resulting image quality of adaptive beamformers. This can be summarized into the *blessing* and the *curse* of software beamforming.

4.1 The blessing

The published results in **(Paper I, II, III and IV)** demonstrate some of the benefits, the blessings, of software beamforming: the flexibility. The ultrasound signals received are better exploited through techniques such as retrospective beamforming and various adaptive beamforming methods. Software beamforming allows flexible delay models, flexible combinations of the received signals and generally improved beamforming resulting in higher image quality. Perhaps the main benefit of software beamforming is that the entire 2D image reconstruction, from raw channel data to final rendered images, may be done on any device with sufficient processing power such as an iPhone. The ability to do software beamforming on *off-the-shelf* devices will most likely drive down the price of ultrasound equipment since expensive specialized hardware for beamforming is obsolete. Cheaper ultrasound systems will aid the democratization of ultrasound imaging, making it available to more people, potentially leading to better and earlier diagnosis of medical conditions.

4.2 The curse

The issues with software beamforming, the curse, is that it allows implementations so flexible that they invalidate the metrics used to evaluate the image quality **(Paper VII and IX)**. The complexity can also make it hard to gain insight into why the image quality is improved **(Paper V)**. The methods can alternate

the speckle statistics **(Paper VIII)**, again affecting the conventional contrast metrics. An alternated speckle pattern will also look unfamiliar to a physician who has years of experience viewing conventional ultrasound images. Also, there is a potential that unwanted artifacts occur from the adaptive methods as we showed in **(Paper VI)**.

4.3 Testing scenarios

It is important to be aware that the results we have obtained are limited to the cases we have tested. Even though, most of the adaptive beamformers investigated in this thesis, except the SLSC, does not seem to significantly improve the probability of detecting a hypoechoic cyst in speckle **(Paper IX)**. With a reservation that the algorithms and implementations could potentially be better tuned for lesion detection. However, it might be that some of the methods do suppress other types of noise that occur in in-vivo imaging. The author's opinion is, therefore, that the scenarios used to test and evaluate new techniques need to be more complex than what typically has been used in the research literature. The conventional hypoechoic cyst in speckle to evaluate contrast, and the single point scatterer to evaluate resolution are not complex enough scenarios to truly evaluate the image quality and clinical relevance of a method. As a minimum, when evaluating contrast - gradients should be studied in combination with the dynamic range test, as suggested in **(Paper VII)** to evaluate whether a method is alternating the dynamic range. Metrics immune to both dynamic range alterations and alterations of the speckle statistics should be used to evaluate contrast. The suggested metric, the generalized contrast-to-noise-ratio **(Paper VII)**, is such a metric. Also, as we saw in Section 2.10.2, perhaps single point scatterers to evaluate resolution is not good enough. Perhaps a measure of separability is more relevant than a measure of mainlobe width. However, further studies need to investigate this more in-depth.

4.4 In-vivo imaging

Research on medical ultrasound imaging is very much applied research. Thus, we should always aim towards actually improving clinical images to assist a physician in diagnosing a patient. Methods should be tested on in-vivo cases together with the knowledge of experienced physicians. We did so in **(Paper X)** where

> we used the MV beamforming technique on in vivo cardiac ultrasound data creating images from three different views of a heart: the parasternal short-axis, parasternal long-axis, and apical four-chamber views. The images reveal that the improved resolution of the MV beamforming technique produces images with improved lateral resolution, resulting in a better resolved speckle structure compared with that of conventional DAS beamforming. Myocardial

> microstructure, that is, the architecture of cardiomyocytes, connective tissue fibers, blood vessels and neural tissue, contributes to the reflected ultrasound data. Further studies are needed to identify the efficiency of MV compared with DAS in terms of identifying pathological alterations in this microstructure.

We were careful not to conclude too boldly since, as is the problem with in-vivo data, it is hard to know what is the actual underlying structures.

Another interesting publication using in-vivo data is the paper *Robust Short-Lag Spatial Coherence Imaging of Breast Ultrasound Data: Initial Clinical Results* by Wiacek, Rindal, Falomo, et al. We showed that the novelty of adaptive beamforming is not limited to simply improving the image quality in terms of contrast and resolution. Adaptive beamforming can improve diagnostics by displaying novel clinical information different from the conventional B-mode image. More specifically, we showed that SLSC could "improve the fluid vs. solid classification of hypoechoic breast masses and improve the detectability of fluid-filled masses, thereby improving the diagnostic power of breast ultrasound imaging." (Wiacek et al. 2018b). Three images from the publication is included in Figure 4.1, where (a) is a simple fluid-filled cyst, (b) is a fibroadenoma (a benign mass) while (c) is a hematoma (a collection of blood). The findings in (Wiacek

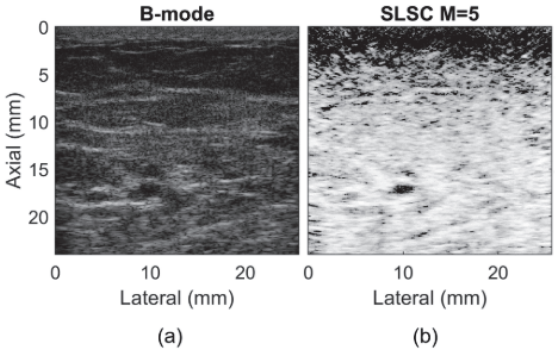

(a) Simple fluid filled cyst

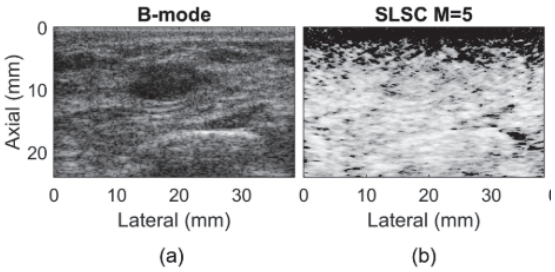

(b) A fibroadenoma

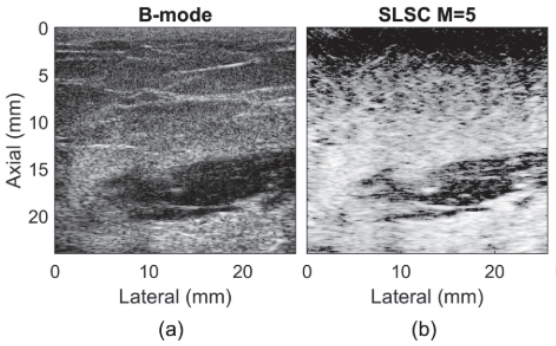

(c) A hematoma

Figure 4.1: Three images from (Wiacek et al. 2018b) where (a) is a simple fluid filled cyst, (b) is a fibroadenoma which is a benign mass while (c) is a hematoma which is a collection of blood. IEEE holds all copyrights ©.

et al. 2018b) can be illustrated with the images in Figure 4.1. All three masses appear hypoechoic in the B-mode image. However, in the coherence images the masses that are fluid-filled (a) and (c) have low coherence - thus appearing dark in the SLSC images while the solid mass in (b) has high coherence.

Chapter 5

Concluding Remarks

5.1 This thesis in a holistic view

This thesis started showing that the number of papers on adaptive beamforming has grown exponentially over the last two decades. Some of these papers could claim unprecedented improvements with more than 100% improvement of the contrast. We raised some research questions based on this observation. Among the questions was whether the results obtained provided a fair comparison between methods, and further if there is a consensus in the literature on what metrics should be used to evaluate the image quality.

We believe the work done in this thesis has brought our research community forward in terms of open and reproducible research through the development of the UltraSound ToolBox (USTB). We believe the USTB is a valuable tool since it provides reference implementations of several state-of-the-art beamforming algorithms as well as sharing benchmarking datasets to evaluate methods. The USTB is open source, meaning that any author can share, or correct, the implementation of their method. The USTB was a valuable and productive tool in this thesis resulting in thorough comparisons of the state-of-the-art adaptive beamformers, revealing that some do alter the speckle statistics compared to the conventional delay-and-sum. We also revealed that unwanted artifacts such as the dark region artifact could occur from adaptive beamforming.

The review of the contrast metrics used in the literature is very important. The review revealed that there is no consensus on contrast metrics used in ultrasound imaging. Perhaps more important is the identification of the effect of dynamic range alterations in the estimation of contrast. We identified that several state-of-the-art adaptive beamformers alternate the dynamic range and that these dynamic range alterations invalidate the conventional contrast metrics. These findings left, in the author's opinions, the community in distress. We did provide a tool, *the dynamic range test*, to investigate whether an algorithm alters the dynamic range. Luckily, we provided an answer to our call for a new metric when we introduced *the generalized contrast-to-noise ratio* (GCNR). The GCNR is immune to both dynamic range alterations and alterations of the speckle statistics, and we believe it is a very valuable tool in the comparison of adaptive beamforming techniques.

This thesis also presented results showing some of the benefits of both software and adaptive beamforming. Answering our first research question and confirming that software beamforming does have benefits in terms of improving the image quality of medical ultrasound images. The improved image quality is achieved through flexible implementations accessing, and better exploiting the full channel data set earlier in the processing chain.

Our last research question was simply a question on whether adaptive beamforming is clinically relevant. We believe our results from imaging the interventricular septum of the heart with the minimum variance beamformer displays interesting findings based on the improved resolution. This leads to a hypothesis that adaptive beamforming may improve the visualization of the interventricular septum of the heart. We would also like to point to the results mentioned in Section 4.4 from (Wiacek et al. 2018b), where we showed that the novelty and clinical relevance of adaptive beamforming is not limited to merely improving the image quality in terms of contrast and resolution. Adaptive beamforming can improve diagnostics by displaying novel clinical information different from the conventional B-mode image. Thus, even though some of the results published among the exponentially growing number of papers on adaptive beamforming might be questionable – there are still methods and algorithms that achieve what should be the goal of research on medical ultrasound imaging: clinical relevance.

5.2 Further aspects

Based on the results presented in this thesis, the author believes that the research community would benefit from complying to the following:

- If more publications were using a shared processing framework, such as the UltraSound ToolBox (USTB, http://www.USTB.no), research would be more open and reproducible. The USTB would also cut down implementation time, boosting research productivity. A common framework and standard datasets would also make the revision of research much easier, more efficient, and more correct.
- When evaluating the contrast of adaptive beamformers, gradients should be studied to evaluate whether the dynamic range is alternated. The dynamic range test, with shared implementations and data available through https://www.ustb.no/publications/paper_VII, facilitates such investigations.
- Contrast metrics immune to dynamic range alterations, and alternated speckle statistics should be used. The suggested generalized contrast-to-noise-ration is such a metric.
- The resolution of adaptive beamformers should, possibly, be measured using separability instead of mainlobe width. More thorough investigations than the one in Section 2.10.2 needs to be done.
- The adaptive beamformers performance on more complex scenarios than cysts in speckle and point targets should be investigated. However, effects should be studied separately to be sure that the results obtained are not originating because of unwanted side effects, such as alternating the dynamic range. One such interesting scenario is the investigation of coherence based beamforming on, for example, reverberation noise.

- Further development of the USTB with an overall goal of reaching image quality comparable to clinical systems. Today, the image quality of the images in the research literature is significantly lower than the quality of the images in clinical scanners. There are, of course, many reasons for this, but the lack of the full processing pipeline, including proper post-processing such as e.g., speckle reduction. Having a state of the art implementation of the full processing chain is, of course, difficult for a single researcher or a single research group. However, with a joint effort, an open source implementation comparable to the quality of clinical scanners could be achieved.
- To evaluate the true impact of adaptive beamforming studies on in-vivo data in cooperation with skilled physicians should be sought. After all, the physicians and their preferences are the final metrics of image quality.

Bibliography

Applebaum, S. 1976. “Adaptive arrays”. *IEEE Transactions on Antennas and Propagation* 24, no. 5 (): 585–598. doi:10.1109/TAP.1976.1141417.

Asl, B. M. and Mahloojifar, A. 2010. “Eigenspace-based minimum variance beamforming applied to medical ultrasound imaging”. *IEEE Transactions on Ultrasonics, Ferroelectrics, and Frequency Control* 57 (11): 2381–2390. doi:10.1109/TUFFC.2010.1706.

Austeng, A., Nilsen, C.-I. C., Jensen, A. C., Nasholm, S. P., and Holm, S. 2011. “Coherent Plane-Wave Compounding and Minimum Variance Beamforming”. In *2011 IEEE International Ultrasonics Symposium*. Ieee.

Bae, M. H. 2000. “A study of synthetic-aperture imaging with virtual source elements in B-mode ultrasound imaging systems”. *IEEE Transactions on Ultrasonics, Ferroelectrics, and Frequency Control* 47 (6): 1510–1519. doi:10.1109/58.883540.

Bernard, O., Hansen, H. H. G., Kruizinga, P., Mc, E., Ricci, S., Rindal, O. M. H., Rodriguez-molares, A., Stuart, M. B., and Dos Santos, P. F. V. 2018. “The Ultrasound File Format (UFF) - First draft”. *IEEE International Ultrasonics Symposium, IUS*. doi:10.1109/ULTSYM.2018.8579642.

Boni, E., Yu, A. C., Freear, S., Jensen, J. A., and Tortoli, P. 2018. “Ultrasound open platforms for next-generation imaging technique development”. *IEEE Transactions on Ultrasonics, Ferroelectrics, and Frequency Control* 65 (7): 1078–1092. doi:10.1109/TUFFC.2018.2844560.

Bryn, F. 1962. “Optimum Signal Processing of Three-Dimensional Arrays Operating on Gaussian Signals and Noise”. *The Journal of the Acoustical Society of America* 34 (3): 289–297. doi:10.1121/1.1928112.

Camacho, J., Parrilla, M., and Fritsch, C. 2009. “Phase coherence imaging”. *IEEE Transactions on Ultrasonics, Ferroelectrics, and Frequency Control* 56 (5): 958–974. doi:10.1109/TUFFC.2009.1128.

Capon, J. 1964. “Optimum weighting functions for the detection of sampled signals in noise”. *IEEE Transactions on Information Theory* 10, no. 2 (): 152–159. doi:10.1109/TIT.1964.1053664.

Chau, G., Lavarello, R., and Dahl, J. 2016. “Short-Lag Spatial Coherence Weighted Minimum Variance Beamformer for Plane-wave Images”: 1–3.

Denarie, B., Tangen, T. A., Ekroll, I. K., Rolim, N., Torp, H., and Lovstakken, L. 2013. “Coherent Plane Wave Compounding for Very High Frame Rate Ultrasonography of Rapidly Moving Targets”. 32 (7): 1265–1276.

Diamantis, K., Anderson, T., Butler, M. B., Villagomez-Hoyos, C. A., Jensen, J. A., and Sboros, V. 2019. "Resolving ultrasound contrast microbubbles using minimum variance beamforming". *IEEE Transactions on Medical Imaging* 38 (1): 194–204. doi:10.1109/TMI.2018.2859262.

Flax, S. W. and O'Donnell, M. 1988. "Phase-aberration correction using signals from point reflectors and diffuse scatterers: basic principles". *IEEE Transactions on Ultrasonics, Ferroelectrics, and Frequency Control* 35, no. 6 (): 758–767. doi:10.1109/58.9333.

Franceschetti, G. and Lanari, R. 1999. *Synthetic Aperture Radar Processing*. Electronic Engineering Systems. Taylor & Francis.

Frazier, C. H. and O'Brien, W. D. 1998. "Synthetic aperture techniques with a virtual source element". *IEEE Transactions on Ultrasonics, Ferroelectrics, and Frequency Control* 45 (1): 196–207. doi:10.1109/58.646925.

Freeman, S., Li, P. C., and Odonnell, M. 1995. "Retrospective Dynamic Transmit Focusing". *Ultrasonic Imaging* 17 (3): 173–196. doi:https://doi.org/10.1006/uimg.1995.1008.

Harris, F. J. 1978. "On the Use of Windows for Harmonic Analysis with the Discrete Fourier Transform". *Proceedings of the IEEE* 66 (1): 51–83.

Hergum, T., Bjåstad, T., Kristoffersen, K., and Torp, H. 2007. "Parallel beamforming using synthetic transmit beams". *IEEE Transactions on Ultrasonics, Ferroelectrics and Frequency Control* 54 (2).

Holfort, I. K., Gran, F., and Jensen, J. A. 2008. "Plane wave medical ultrasound imaging using adaptive beamforming". *2008 5th IEEE Sensor Array and Multichannel Signal Processing Workshop*, no. 2: 288–292.

Holm, S. 2019. *Waves with Power-Law Attenuation*. Vol. 1. Norway: Springer International Publishing. doi:10.1007/978-3-030-14927-7.

Hverven, S., Rindal, O. M. H., Hunter, A., and Austeng, A. 2017a. "Point scatterer enhancement in ultrasound by wavelet coefficient shrinkage". In *IEEE International Ultrasonics Symposium, IUS*, 1–4. doi:10.1109/ULTSYM.2017.8091972.

Hverven, S. M., Rindal, O. M. H., Rodriguez-Molares, A., and Austeng, A. 2017b. "The Influence of Speckle Statistics on Contrast Metrics in Ultrasound Imaging". *IEEE International Ultrasonics Symposium, IUS*: 1–4. doi:10.1109/ULTSYM.2017.8091875.

Jensen, A. and Austeng, A. 2014. "The iterative adaptive approach in medical ultrasound imaging". *IEEE Transactions on Ultrasonics, Ferroelectrics, and Frequency Control* 61 (10): 1688–1697. doi:10.1109/TUFFC.2014.006478.

Jensen, J. A. 1996. "Field: A program for simulating ultrasound systems". *Medical & Biological Engineering & Computing* 34:351–353.

Jensen, J. A., Nikolov, S. I., Gammelmark, K. L., and Peders, M. H. 2006. "Synthetic aperture ultrasound imaging". *Ultrasonics* 44. doi:10.1016/j.ultras.2006.07.017.

Jensen, J. A. and Svendsen, N. B. 1992. “Calculation of Pressure Fields from Arbitrarily Shaped, Apodized, and Excited Ultrasound Transducers”. *IEEE Transactions on Ultrasonics, Ferroelectrics and Frequency Control* 39 (2): 262–267.

Johnson, D. H. and Dugdeon, D. E. 1993. *Array signal processing: Concepts and techniques*. Vol. Prentice-Hall signal processing series. UpperSaddle River, NJ 07458: P.T.R. Prentice-Hall.

Kaczkowski, P. 2016. “Bandwidth Sampling Data Acquisition with the Vantage System for High Frequency Transducers”. *Verasonics Inc. White Paper*.

Krishnan, S., Rigby, K. W., and O’Donnell, M. 1997. “Improved estimation of phase aberration profiles”. *IEEE Transactions on Ultrasonics, Ferroelectrics, and Frequency Control* 44 (3): 701–713. doi:10.1109/58.658333.

Kulina, R., Agarwal, S., Wiley, B., Narula, J., Sengupta, P. P., and Chaudhry, F. A. 2016. “New Software Beamforming Algorithm is Superior to Standard Hardware-Based Beamformer in Endocardial Border Detection”. *GE Healthcare Whitepaper, GE Symposium 2016*: 1–4.

Lediju Bell, M. A., Goswami, R., Kisslo, J. A., Dahl, J. J., and Trahey, G. E. 2013. “Short-Lag Spatial Coherence (SLSC) Imaging of Cardiac Ultrasound Data: Initial Clinical Results”. *Ultrasound in medicine & biology* 39 (10): 1861–1874. doi:10.1016/j.ultrasmedbio.2013.03.029.

Lediju, M. A., Trahey, G. E., Byram, B. C., and Dahl, J. J. 2011. “Short-lag spatial coherence of backscattered echoes: Imaging characteristics”. *IEEE Transactions on Ultrasonics, Ferroelectrics, and Frequency Control* 58 (7): 1377–1388. doi:10.1109/TUFFC.2011.1957.

Li, P. C. and Li, M. L. 2003. “Adaptive imaging using the generalized coherence factor”. *IEEE Transactions on Ultrasonics, Ferroelectrics, and Frequency Control* 50 (2): 128–141. doi:10.1109/TUFFC.2003.1182117.

Liebgott, H., Rodriguez-Molares, A., Cervenansky, F., Jensen, J. A., and Bernard, O. 2016. “Plane-Wave Imaging Challenge in Medical Ultrasound”. *IEEE International Ultrasonics Symposium, IUS* 2016-Novem. doi:10.1109/ULTSYM.2016.7728908.

Mallart, R. and Fink, M. 1994. “Adaptive focusing in scattering media through sound-speed inhomogeneities: The van Cittert Zernike approach and focusing criterion”. *The Journal of the Acoustical Society of America* 96 (6): 3721. doi:10.1121/1.410562.

— . 1991. “The van Cittert-Zernike theorem in pulse echo measurements”. *Journal of Acustical Society of America* 90 (November 1991): 2718–2727.

Mann, J. A. and Walker, W. F. 2002. “A constrained adaptive beamformer for medical ultrasound: initial results”. In *2002 IEEE Ultrasonics Symposium, 2002. Proceedings.* Vol. 2, 1807–1810 vol.2. doi:10.1109/ULTSYM.2002.1192650.

Matrone, G., Savoia, A. S., and Magenes, G. 2015. "The Delay Multiply and Sum Beamforming Algorithm in Ultrasound B-Mode Medical Imaging". *IEEE Transactions on Medical Imaging* 34 (4): 940–949.

McNeil Jr., D. G. 2019. "In African Villages, These Phones Become Ultrasound Scanners". Visited on 06/06/2019. https://www.nytimes.com/2019/04/15/health/medical-scans-butterfly-iq.html.

Mehdizadeh, S., Austeng, A., Johansen, T. F., and Holm, S. 2012. "Eigenspace based minimum variance beamforming applied to ultrasound imaging of acoustically hard tissues". *IEEE Transactions on Medical Imaging* 31 (10): 1912–1921. doi:10.1109/TMI.2012.2208469.

Montaldo, G., Tanter, M., Bercoff, J., Benech, N., and Fink, M. 2009. "Coherent plane-wave compounding for very high frame rate ultrasonography and transient elastography". *IEEE Transactions on Ultrasonics, Ferroelectrics, and Frequency Control* 56 (3): 489–506. doi:10.1109/TUFFC.2009.1067.

Nguyen, N. Q. and Prager, R. W. 2018. "A Spatial Coherence Approach to Minimum Variance Beamforming for Plane-Wave Compounding". *IEEE Transactions on Ultrasonics, Ferroelectrics, and Frequency Control* PP (99): 1–1. doi:10.1109/TUFFC.2018.2793580.

Nguyen, N. Q. and Prager, R. W. 2016. "High-Resolution Ultrasound Imaging With Unified Pixel-Based Beamforming". *IEEE Trans. Med. Imaging* 35 (1): 98–108.

Nikolov, S. I., Kortbek, J., and Jensen, J. A. 2010. "Practical applications of synthetic aperture imaging". *2010 IEEE International Ultrasonics Symposium*: 350–358. doi:10.1109/ULTSYM.2010.5935627.

Nock, L., Trahey, G. E., and Smith, S. W. 1989. "Phase aberration correction in medical ultrasound using speckle brightness as a quality factor". *The Journal of the Acoustical Society of America* 85 (5): 1819–1833.

Ozkan, E., Vishnevsky, V., and Goksel, O. 2018. "Inverse Problem of Ultrasound Beamforming with Sparsity Constraints and Regularization". *IEEE Transactions on Ultrasonics, Ferroelectrics, and Frequency Control* PP (99): 1–1. doi:10.1109/TUFFC.2017.2757880.

Palmer, C. L. and Rindal, O. M. H. 2019. "Wireless, Real-Time Plane-Wave Coherent Compounding on an iPhone - a feasibility study". *IEEE Transactions on Ultrasonics, Ferroelectrics, and Frequency Control*, no. PP: 1–11. doi:10.1109/TUFFC.2019.2914555.

Palmer, C. L., Rindal, O. M. H., Holm, S., and Austeng, A. 2016. "Realtime plane-wave software beamforming with an iPhone". *IEEE International Ultrasonics Symposium, IUS*: 1–4. doi:10.1109/ULTSYM.2016.7728408.

Papadacci, C., Pernot, M., Couade, M., Fink, M., and Tanter, M. 2014. "High-contrast ultrafast imaging of the heart". *IEEE Transactions on Ultrasonics, Ferroelectrics, and Frequency Control* 61 (2): 288–301. doi:10.1109/TUFFC.2014.6722614.

Patterson, M. and Foster, F. 1983. "The Improvement and quantitative assessment of b-mode images produced by an annular array/cone hybrid". *Ultrasonic Imaging*, no. 5: 195–213.

Prieur, F., Rindal, O. M. H., and Austeng, A. 2018. "Signal Coherence and Image Amplitude With the Filtered Delay Multiply and Sum Beamformer". *IEEE Transactions on Ultrasonics, Ferroelectrics, and Frequency Control* 65 (7): 1133–1140. doi:10.1109/TUFFC.2018.2831789.

Prieur, F., Rindal, O. M. H., Holm, S., and Austeng, A. "Influence of the Delay-Multiply-And-Sum beamformer on the ultrasound image amplitude". *IEEE International Ultrasonics Symposium, IUS*: 1–4. doi:10.1109/ULTSYM.2017.8092637.

Proakis, J. and Manolakis, D. 2007. *Digital Signal Processing*. Pearson Prentice Hall.

Rayleigh, L. J. W. S. 1879. "Investigations in optics, with special reference to the spectroscope". *The London, Edinburgh, and Dublin Philosophical Magazine and Journal of Science* 8 (49): 261–274. doi:10.1080/14786447908639684.

Rindal, O. M. H. 2018. "Achieving uniform field of view (FOV) in synthetic aperture imaging (STAI) in Field II simulations". Visited on 06/05/2018. http://www.ustb.no/examples/uniform-fov-in-field-ii-simulations/.

Rindal, O. M. H., Aakhus, S., Holm, S., and Austeng, A. 2017. "Hypothesis of Improved Visualization of Microstructures in the Interventricular Septum with Ultrasound and Adaptive Beamforming". *Ultrasound in Medicine and Biology* 43 (10): 2494–2499. doi:10.1016/j.ultrasmedbio.2017.05.023.

Rindal, O. M. H., Åsen, J. P., Holm, S., and Austeng, A. 2014. "Understanding Contrast Improvements from Capon Beamforming". *IEEE International Ultrasonics Symposium, IUS*, no. 1: 1694–1697. doi:10.1109/ULTSYM.2014.0420.

Rindal, O. M. H. and Austeng, A. 2016. "Double Adaptive Plane-Wave Imaging". *IEEE International Ultrasonics Symposium, IUS*: 1–4. doi:10.1109/ULTSYM.2016.7728906.

Rindal, O. M. H., Austeng, A., Fatemi, A., and Rodriguez-Molares, A. 2019. "The Effect of Dynamic Range Alterations in the Estimation of Contrast". *IEEE Transactions on Ultrasonics, Ferroelectrics, and Frequency Control* PP:1–11. doi:10.1109/TUFFC.2019.2911267.

Rindal, O. M. H., Austeng, A., Torp, H., Holm, S., and Rodriguez-Molares, A. 2016. "The dynamic range of adaptive beamformers". *IEEE International Ultrasonics Symposium, IUS*, no. 1: 1–4. doi:10.1109/ULTSYM.2016.7728717.

Rindal, O. M. H., Rodriguez-Molares, A., and Austeng, A. 2018. "A simple, artifact-free, virtual source model". *IEEE International Ultrasonics Symposium, IUS*: 1–4. doi:10.1109/ULTSYM.2018.8579944.

— . 2017. "The Dark Region Artifact in Adaptive Ultrasound Beamforming". *IEEE International Ultrasonics Symposium, IUS*: 1–4. doi:10.1109/ULTSYM.2017.8092255.

Rodriguez-Molares, A., Rindal, O. M. H., Bernard, O., Nair, A., Lediju Bell, M. A., Liebgott, H., Austeng, A., and Løvstakken, L. 2017. "The UltraSound ToolBox". *IEEE International Ultrasonics Symposium, IUS*: 1–4. doi:10.1109/ULTSYM.2017.8092389.

Rodriguez-Molares, A., Rindal, O. M. H., D'hooge, J., Måsøy, S.-E., Austeng, A., Lediju Bell, M. A., and Torp, H. 2019. "The Generalized Contrast-to-Noise ratio". *Prepared for submission to IEEE Transactions on Ultrasonics, Ferroelectrics, and Frequency Control*: 1–12.

Rodriguez-Molares, A., Rindal, O. M. H., D'hooge, J., Måsøy, S.-E., Austeng, A., and Torp, H. 2018. "The Generalized Contrast-to-Noise Ratio". *IEEE International Ultrasonics Symposium, IUS*, no. 6: 1–4. doi:10.1109/ULTSYM.2018.8580101.

Rodriguez-Molares, A., Torp, H., Denarie, B., and Løvstakken, L. 2015. "The Angular Apodization in Coherent Plane-Wave Compounding". *IEEE transactions on ultrasonics, ferroelectrics, and frequency control* 62 (11): 2018–2023.

Sasso, M. and Cohen-Bacrie, C. 2005. "Medical Ultrasound Using The Fully Adaptive Beamformer". *IEEE International Conference on Acoustical Speech and Signal Processing, 2015. Proceedings (ICAASP 05).* 2 (4): 489–492.

Scopus. 2018. *Scopus Document Search Results.* https://www.scopus.com. Accessed: 2018-02-21.

Shattuck, D. P., Weinshenker, M. D., Smith, S. W., and Ramm, O. T. von. 1984. "Explososcan: A parallel processing technique for high speed ultrasound imaging with linear phased arrays". *The Journal of the Acoustical Society of America* 75 (4): 1273–1282. doi:10.1121/1.390734.

Shin, J. and Huang, L. 2017. "Spatial Prediction Filtering of Acoustic Clutter and Random Noise in Medical Ultrasound Imaging". *IEEE Transactions on Medical Imaging* 36 (2): 396–406. doi:10.1109/TMI.2016.2610758.

Siemens Healthineers. 2019. "A Honeymoon at Siemens - The story of the first ultrasound image of a beating heart". https://www.medmuseum.siemens-healthineers.com/en/stories-from-the-museum/echokardiographie.

Smith, S., Lopez, H., and Bodine, W. 1985. "Frequency independent ultrasound contrast-detail analysis". *Ultrasound in Medicine & Biology* 11 (3): 467–477. doi:https://doi.org/10.1016/0301-5629(85)90158-9.

Soni, N. J., Arntfield, R., and Kory, P. 2014. *Point of Care Ultrasound E-book.* Elsevier Health Sciences.

Steinberg, B. D. 1976. *Principles of Aperture and Array System Design.* John Wiley & Sons.

SuperSonic Imagine. 2019. "Aixplorer". https://www.supersonicimagine.com.

Synnevåg, J., Austeng, A., and Holm, S. 2005. "Minimum variance adaptive beamforming applied to medical ultrasound imaging". In *IEEE Ultrasonics Symposium, 2005.* 2:1199–1202. doi:10.1109/ULTSYM.2005.1603066.

Synnevåg, J.-F., Austeng, A., and Holm, S. 2009. "Benefits of minimum-variance beamforming in medical ultrasound imaging". *Ultrasonics, Ferroelectrics and Frequency Control, IEEE Transactions on* 56 (9): 1868–1879.

Szabo, T. L. 2013. *Diagnostic Ultrasound Imaging: Inside Out*. Second Edi. Biomedical Engineering. Elsevier Science.

Szasz, T., Basarab, A., and Kouamé, D. 2016a. "Beamforming Through Regularized Inverse Problems in Ultrasound Medical Imaging". *IEEE Transactions on Ultrasonics, Ferroelectrics, and Frequency Control* 63 (12): 2031–2044. doi:10.1109/TUFFC.2016.2608939.

Szasz, T., Basarab, A., and Kouamé, D. 2016b. "Strong reflector-based beamforming in ultrasound medical imaging". *Ultrasonics* 66:111–124. doi:10.1016/j.ultras.2015.11.003. arXiv: 1507.08184.

Viola, F. and Walker, W. 2005. "Adaptive signal processing in medical ultrasound beamforming". *Proceedings IEEE Ultrasonics Symposium* 4 (c): 1980–1983. doi:10.1109/ULTSYM.2005.1603264.

Von Ramm, O. T. and Thurstone, F. L. 1975. "Thaumascan: design considerations and performance characteristics". In *Ultrasound in medicine*, 373–378. Springer.

Wagner, R. F., Smith, S. W., Sandrik, J. M., and Lopez, H. 1983. "Statistics of Speckle in Ultrasound B-Scans". *IEEE Transactions on Sonics and Ultrasonics* 30 (3).

Wang, Z., Li, J., and Wu, R. 2005. "Time-delay- And time-reversal-based robust Capon beamformers for ultrasound imaging". *IEEE Transactions on Medical Imaging* 24 (10): 1308–1322. doi:10.1109/TMI.2005.857222.

Wiacek, A., Falomo, E., Myers, K., Rindal, O. M. H., Fabrega-foster, K., Harvey, S., and Bell, M. A. L. 2018a. "Clinical Feasibility of Coherence-Based Beamforming to Distinguish Solid from Fluid Hypoechoic Breast Masses". *IEEE International Ultrasonics Symposium, IUS*: 1–4. doi:10.1109/ULTSYM.2018.8579846.

Wiacek, A., Rindal, O. M. H., Falomo, E., Myers, K., Fabrega-Foster, K., Harvey, S., and Bell, M. A. L. 2018b. "Robust Short-Lag Spatial Coherence Imaging of Breast Ultrasound Data: Initial Clinical Results". *IEEE Transactions on Ultrasonics, Ferroelectrics, and Frequency Control* 66 (3): 527–540. doi:10.1109/TUFFC.2018.2883427.

Widrow, B., Mantey, P. E., Griffiths, L. J., and Goode, B. B. 1967. "Adaptive antenna systems". *Proceedings of the IEEE* 55 (12): 2143–2159. doi:10.1109/PROC.1967.6092.

Zhao, J., Wang, Y., Yu, J., Guo, W., Zhang, S., and Aliabadi, S. 2017. "Short-lag Spatial Coherence Ultrasound Imaging with Adaptive Synthetic Transmit Aperture Focusing". PMID: 28068874, *Ultrasonic Imaging* 39 (4): 224–239. doi:10.1177/0161734616688328.

Zhuang, B., Rohling, R., and Abolmaesumi, P. 2018. "Accumulated Angle Factor-Based Beamforming to Improve the Visualization of Spinal Structures in Ultrasound Images". *IEEE Transactions on Ultrasonics, Ferroelectrics, and Frequency Control* 65 (2): 210–222. doi:10.1109/TUFFC.2017.2781726.

Papers

Paper I

The UltraSound ToolBox

Alfonso Rodriguez-Molares*, Ole Marius Hoel Rindal*, Olivier Bernard Olivier, Arun Nair, Muyinatu A. Lediju Bell, Hervé Liebgott, Andreas Austeng and Lasse Løvstakken

Published in *IEEE International Ultrasonics Symposium, IUS.* (2017), 1–4. doi: 10.1109/ULTSYM.2017.8092389.

*These authors are shared first authors with equal contributions.

Paper II

II

A simple, artifact-free, virtual source model

Ole Marius Hoel Rindal, Alfonso Rodriguez-Molares and Andreas Austeng

Published in *IEEE International Ultrasonics Symposium, IUS,* (2018), 1–4. doi: 10.1109/ULTSYM.2018.8579944

Paper III

Wireless, Real-Time Plane-Wave Coherent Compounding on an iPhone - a feasibility study

III

Cameron Lowell Palmer* and Ole Marius Hoel Rindal*

Accepted for publication in *IEEE Transactions on Ultrasonics, Ferroelectrics, and Frequency Control*, (2019), 1–11. doi: 10.1109/TUFFC.2019.2914555.

*These authors are shared first authors with equal contributions.

Erratum: In equation (9) it should be "if $|x - x_m| <= \frac{z}{2f_\#}$". There is missing a "2" in the denominator. This was corrected in the proof of the final paper.

Wireless, Real-Time Plane-Wave Coherent Compounding on an iPhone - a feasibility study

Cameron Lowell Palmer*, *Student Member IEEE* and Ole Marius Hoel Rindal*, *Student Member, IEEE*

***Abstract*—The processing power in commercially available hand-held devices has improved dramatically in recent years. In parallel, techniques used in high frame-rate medical ultrasound imaging, specifically plane-wave imaging, have reduced the number of ultrasound transmissions and amount of data necessary to reconstruct an ultrasound image. In combination, the processing power and data reduction allow all of the processing steps in ultrasound image formation, from raw ultrasound channel data to final rendering, to be performed on a hand-held device. In this study, we send raw ultrasound channel data from a research scanner wirelessly to an *off-the-shelf* hand-held device. The hand-held unit's graphical processing unit is processing the raw ultrasound data into the final image, achieving real-time frame rates on the order of 60-90 frames per second for a single angle plane wave transmission. Higher quality images are achieved by trading-off frame rate by coherently compounding multiple plane wave images, resulting in frame-rates on the order of e.g. 13 frames per second when coherently compounding 7 plane wave transmissions. The presented setup has the potential of providing image quality which could be valuable for simple medical ultrasound diagnostic scans of e.g. the carotid artery or thyroid. Also, since the computationally expensive beamforming can be done in *off-the-shelf* devices, this could reduce the price of hand-held ultrasound systems in the future.**

***Index Terms*—Hand-held ultrasound, software beamforming, wireless probe, coherent plane-wave compounding.**

I. Introduction

HAND-HELD ultrasound systems are receiving increased attention and use [1] [2], and Godt [3] has predicted hand-held ultrasound will even replace the physician's stethoscope. However, ultrasound signal processing and image creation are computationally expensive. Until recently, most clinical high-end ultrasound scanners used specialized hardware to do ultrasound image formation. Ultrasound image formation, known as beamforming, is done by converting and combining the ultrasound signals received on the numerous elements inside the ultrasound probe into a brightness value in the image. Only in recent years has computing power increased to the point that manufacturers of high-end clinical ultrasound scanners could move beamforming into software [4] [5]. Software beamforming allows much more flexible implementations of beamforming algorithms potentially leading to improved image quality [6]–[11] by allowing real-time implementations of sophisticated beamforming techniques [12]–[15]. It is therefore comprehensible that most research ultrasound systems utilize software beamforming [16].

The benefit of a hand-held system is the ability for a physician to carry an ultrasound system in their pocket. Perhaps more importantly is the availability of medical imaging *on the scene* [17]. A paramedic can easily bring a device to the scene of an accident and within seconds perform for example an FAST exam (Focused Assessment with Sonography in Trauma), allowing pre-arrival notification to the hospital in turn allowing a specialized team to be ready in the operating room. In addition, ultrasound images can be transmitted real-time from the scene or ambulance, allowing physicians to review and assist the paramedics in the treatment of the patients before they even arrive at the hospital.

In the range of hand-held medical ultrasound devices specialized hardware implementations of the beamforming algorithms are used in most commercially available devices [18]–[22]. In systems with wireless probes, the bottleneck of transferring large amounts of raw channel data led to all, or parts, of the beamforming to be implemented in dedicated hardware in the ultrasound probe. One technique for such processing is the synthetic aperture sequential beamforming (SASB) [23]. SASB has been demonstrated in implementations for commercially available hand-held devices [24], and the SASB approach motivated a system-level design of a wireless ultrasound probe [25]. The SASB uses focused transmission and performs the first stage of the beamforming in the probe, reducing the amount of data needed to be transferred to the probe significantly.

Recently, the miniaturization of high-performance processing hardware such as graphical processing units (GPUs) has made such high-end hardware available on *off-the-shelf* hand-held devices such as an iPad or iPhone. The hardware improvements have motivated software implementations of other computationally expensive parts of the ultrasound processing chain such as vector flow imaging on commercial, consumer-level tablets [26] [27].

Another recent breakthrough in medical ultrasound imaging is ultra-fast imaging [28]. This was made possible

*The two authors have contributed equally to this work, and appear in alphabetical order.

Palmer is affiliated with the Department of Circulation and Medical Imaging, Faculty of Medicine, Norwegian University of Science and Technology, Trondheim, Norway.
E-mail: cameron.palmer@ntnu.no

O. Rindal is affiliated with the Research Group for Digital Signal Processing and Image Analysis, Department of Informatics, University of Oslo, Oslo, Norway. E-mail: omrindal@ifi.uio.no

Manuscript received January 17th, 2018; revised January 28th and April 16th, 2019.

This article has been accepted for publication in a future issue of this journal, but has not been fully edited. Content may change prior to final publication. Citation information: DOI 10.1109/TUFFC.2019.2914555, IEEE Transactions on Ultrasonics, Ferroelectrics, and Frequency Control

through the introduction of plane-wave imaging [29]. In plane-wave imaging, one can form the complete ultrasound image from the transmission of a single plane wave, compared to the conventional focused transmission that requires hundreds of transmissions per image. This dramatically reduced the amount of channel data necessary to create an image. Higher image quality can be obtained by coherently compounding multiple low-quality plane wave images transmitted at different angles. The drawback of plane wave imaging is reduced penetration depth and fewer tissue harmonics making harmonic imaging challenging.

Fourier beamforming [30] [31] has emerged as a technique that can reduce the computational load of plane wave coherent compounded beamforming compared to conventional delay-and-sum beamforming [32]. Thus, a Fourier beamforming approach could possibly lower the computational load on a hand-held device even more. Especially since most hand-held devices have specialized implementations, and potentially hardware, for the Fast Fourier Transform algorithm [33]. Beamforming in the Fourier domain has also been suggested as a path to do compressed sensing and reducing the amount of data needed to reconstruct the full image [34]. Even though these studies and techniques are interesting and promising for a hand-held device we limited our study to conventional time-delayed beamforming.

In this study, we will exploit the benefits from coherent plane wave compounded (CPWC) imaging and the increased computer power available on commercially available hand-held devices. We will demonstrate that it is possible to do real-time ultrasound image formation on an iPhone/iPad exploiting the processing power of the built-in GPUs. Contrary to the SASB technique, which used focused transmission and a two stage beamforming to reduce the amount of data needed to be transmitted, we use CPWC to reduce the amount of channel data needed per image, which also provides a trade-off between the amount of data to be transferred and image quality. The current study builds on our previous study [35], and a related study [36]. Compared to our previous study we have introduced CPWC imaging and expanding aperture imaging resulting in higher image quality, and several improvements to the processing chain resulting in dramatic improvements to the processing frame rate.

Our hypothesis is primarily; an *off-the-shelf* hand-held device like an iPhone has the processing power to do real-time ultrasound image formation from raw channel data. Here channel data is defined as the signals from the individual elements in an ultrasound probe. Secondarily, that the transmission of channel data from the probe to the iPhone can be done wirelessly. This suggests that a full ultrasound imaging system only needs a wireless probe with minimal processing of the signals, while an iPhone does the computationally expensive image reconstruction. This is different from the existing solutions which all use specialized hardware to do the beamforming [18]–[22]. The wireless probe needs the electronics and power to transmit and receive ultrasonic signals in the individual probe elements, and needs to be able to sufficiently sample, temporarily store and transmit the raw channel data to the phone. This can be done in specialized hardware or field programmable gate arrays, while the full beamforming processing chain can be processed by flexible software implementations in *off-the-shelf* hand held devices. By having a software implementation of the beamforming system, progress in beamforming techniques can easily be incorporated, and improvements in the processing power of commercially hand-held devices can be exploited via software updates while still receiving the same type of data from the probe. We thus believe, that future commercial devices will move more towards using *off-the-shelf* devices for much of the processing to lower the production cost and eventually device cost.

In section II we detail the specific hardware used in our setup and detail the processing pipeline and choices made in the implementation and the networking details. The results are presented in section III and discussed in section IV. We conclude in section V that we are capable of doing real-time ultrasound image formation on an iPhone processing multiple coherently compounding plane waves recorded from an ultrasound probe, as illustrated in Fig. 1.

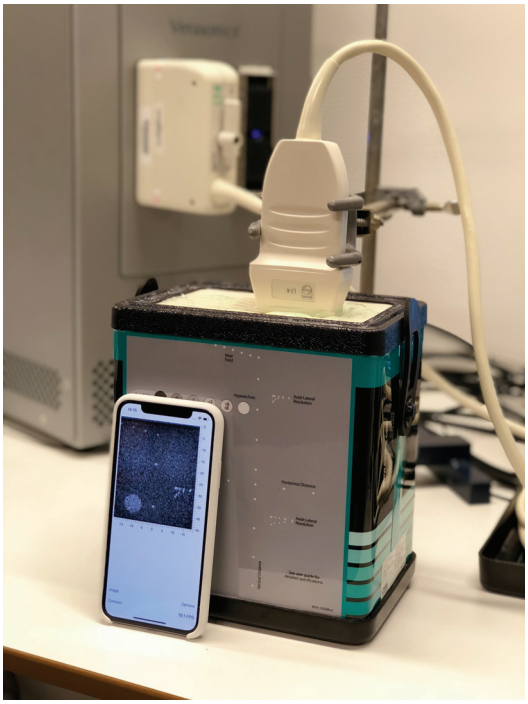

Fig. 1: The complete setup of the ultrasound probe imaging a phantom with the research scanner streaming the channel data wirelessly through the router before it is received, beamformed and displayed on the iPhone. A demo video is available at https://youtu.be/oN8cwysGxyM.

Device	CPU	GPU	Memory	Wi-Fi	Single threaded*	Multi threaded*	Metal*
iPhone 6s+	A9, 2-core @ 1849 MHz	PowerVR GT7600 (six-core)	2 GB	802.11ac	2409	4161	10355
iPhone 8	A11 Bionic, 6-core @ 2390 MHz (2x Monsoon + 4x Mistral)	Apple GPU (three-core graphics)	2 GB	802.11ac MIMO	4225	10145	15137
iPhone X	A11 Bionic, 6-core @ 2390 MHz (2x Monsoon + 4x Mistral)	Apple GPU (three-core graphics)	3 GB	802.11ac MIMO	4213	10148	15239
iPad Pro 2017	A10X Fusion, 3-core @ 2340 MHz	PowerVR Series 7XT (12-core)	4 GB	802.11ac HT80 MIMO	3915	9340	29531

TABLE I: The main technical specifications of the devices used in this study. *The three last columns are benchmark results from https://browser.geekbench.com/ios-benchmarks.

II. Materials and Methods

A. "The wireless probe" and channel data acquisition

To mimic a wireless probe we use a research scanner streaming raw recorded channel data wirelessly to the iPhone using a Unifi (Ubiquiti Networks, Inc., New York, USA) AC-HD-Pro access point. We are using a Verasonics Vantage 256 (Verasonics Inc., Redmond, WA) scanner with a L7-4 (Philips, Amsterdam, NL) linear probe with 128 elements with λ spacing (0.298mm). The transmission sequence is a varying number of plane waves transmitted with a center frequency of 5.1 MHz with maximum and minimum angles at $\alpha = \pm 16°$, except for the case of a single plane wave which is transmitted at $\alpha = 0°$. The data is in-phase and quadrature sampled (IQ-sampled) using the bandwidth sampling data acquisitions available with the Verasonics Vantage systems [37]. In our setup, the number of samples in the IQ-sampled signal can be reduced by an integer factor, specifically 4 compared to the default RF-sampling frequency. However, the IQ-samples are complex, thus having both a real and an imaginary part so effectively the number of samples in the channel data is reduced by a factor of 2 using IQ-sampling. Since the signal is IQ sampled the envelope can be detected by simply taking the magnitude of the signal, avoiding the Hilbert transform needed to detect the envelope from a RF-signal. We are imaging a 45.8 mm deep image requiring us to receive 512 samples per channel. The total amount of data in bytes, per image frame is then:

$$\frac{bytes}{img} = \frac{PWs}{img} \cdot \frac{channels}{img} \cdot \frac{samples}{channel} \cdot \frac{bytes}{sample} \quad (1)$$

$$= \frac{PWs}{img} \cdot 128 \cdot 512 \cdot 8 \quad (2)$$

$$= \frac{PWs}{img} \cdot 524288 \text{ bytes}, \quad (3)$$

where $\frac{PWs}{img}$ varies from 1 to 21 PWs per image, $\frac{channels}{img} = 128$, $\frac{samples}{channel} = 512$ and $\frac{bytes}{sample} = 8$ since we have one real and one complex four-byte signed integer for every sample. Arguably, we could have used two-byte signed integers, but because of limitations in the serialization code using four-byte integers resulted in faster serialization. See details on the serialization in Section II-C.

We will denote the term *the probe* throughout this paper, when referring to the part of our setup mimicking the wireless probe, thus the Verasonics Vantage 256 research scanner recording and processing the raw channel data from the L7-4 probe into a data packet to be transmitted over the network.

B. The Mobile Client

In this study we worked with a range of iOS-based devices, namely the iPhone 6s, 8, X and the iPad Pro. The technical specifications of the devices can be seen in Table I. Apple's iOS devices have adopted an unified memory architecture. This allows the GPU and the CPU to access the same physical memory without needing to transfer data between the processors. This is in contrast to the PC model of discrete memory where CPU/GPU memory have been distinctly separate entities. The unified memory model simplifies the CPU/GPU processing pipeline by allowing data to be written to a shared CPU/GPU buffer. The GPU compute shader has full access to this buffer and can thus process the data without needing to transfer the data to the GPU first. This is in contrast to how some vendors use the term unified memory only meaning a shared address space. A shared address space is convenient to the programmer, but doesn't result in a performance improvement since the copying of data from CPU to GPU is happening behind the scenes.

In addition to the advantage of a shared memory architecture, more recent iterations of Apple's hardware platform have inverted the relationship between screen and GPU refresh with what is marketed as ProMotion [38]. Traditionally, the screen receives GPU updates at a fixed frequency, for example 60 times a second, but with ProMotion the GPU tells the screen when to update. ProMotion, available on iPad Pro, allows a variable refresh rate from 24Hz to 120Hz. A variable refresh rate directly benefits computationally intensive tasks such as beamforming that might have taken too long to complete within a 16.67ms ($\frac{1}{60}$ of a second) time budget and high-frame rate tasks that would be limited by a hardware imposed upper-bound of 60Hz.

We will interchangeably use the term *the phone* for all devices, unless the certain device is explicitly stated, throughout this paper.

This article has been accepted for publication in a future issue of this journal, but has not been fully edited. Content may change prior to final publication. Citation information: DOI 10.1109/TUFFC.2019.2914555, IEEE Transactions on Ultrasonics, Ferroelectrics, and Frequency Control

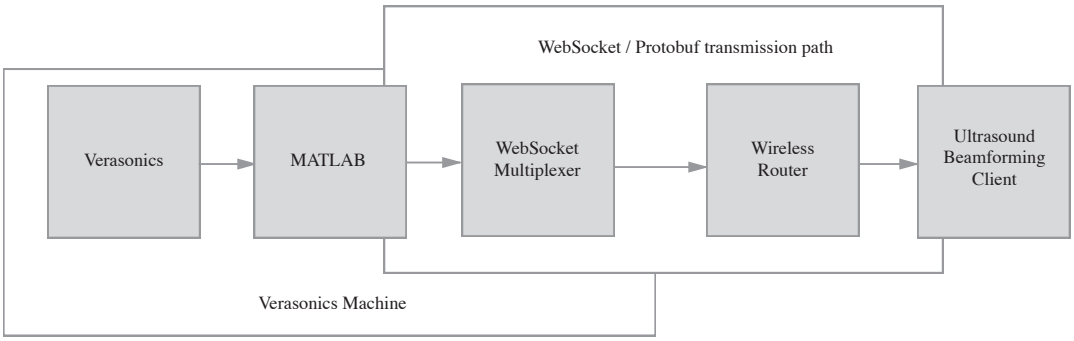

Fig. 2: The flow of data recorded from the L7-4 ultrasound probe connected to the Verasonics Vantage research scanner (*the probe*) to the client (*the phone*).

C. Wireless Networking

For the wireless communication we connected *the phone* and *the probe* over an isolated 802.11ac Wi-Fi network using a Unifi AC-HD-Pro access point (Ubiquiti Networks, Inc., New York, USA), to a switch that via Ethernet connects to the scanner and a DHCP server. The network pipeline is illustrated in Fig. 2. The base station was configured to provide a wireless connection in the 5 GHz spectrum and with 80 MHz wide channels. Performance was measured in the 400-500 Mbps range using iPerf [39]. The Verasonics scanner has an *external* function giving real-time access to the buffer with the raw ultrasound IQ-sampled channel data in MATLAB (The MathWorks Inc., Natick, MA, USA) once the channel data has been received. The channel data is serialized using Google's protocol Buffers (protobufs) [40] through a Java-based (Oracle Corporation, Redwood Shores, CA, USA) library providing a compact binary message structure to encode the settings and data. It was limitations in this Java library that forced us to use four-byte integers instead of two-byte as mentioned in Section II-A. The first protobuf transmitted from *the probe* to *the phone* contains the settings detailing the ultrasound acquisition sequence providing necessary variables for the image reconstruction, while the subsequent protobufs provide the raw channel data sent by the Verasonics research scanner.

To establish the connection between *the phone* and *the probe* a WebSocket (RFC 6455) multiplexer was implemented using Python (Python Software Foundation). The WebSocket is set up using Zeroconf [41] to advertise the correct port and address for clients to connect to thereby avoiding hard-coded ports and IP addresses in the client implementation. In short, the networking pipeline, as illustrated in Fig. 2, starts off with the raw channel data received in the Verasonics scanner serialized into a protobuf before it is transmitted via the WebSocket through the wireless router to *the phone*.

D. Beamforming in software

This section gives a general explanation of the beamforming implemented in software, while the iOS specific implementation is detailed in the next section.

The flexibility of software beamforming allows pixel-based beamforming. This means that we can define a set of pixels, our image, and beamform the ultrasound data directly to the pixels. The first step is to calculate the time delay for every signal received on every element to every pixel in the image.

Given the transducer geometry, the element width and pitch, we get the coordinates for our elements, x_m, and then define the coordinate for every pixel in the image (z, x). Given the speed of sound in human tissue, c, and the angle of the plane wave transmission, α, we can calculate the two-way time delay [29] as illustrated in Fig. 3 by

$$\tau_{tx}(z, x, \alpha) = (z\cos(\alpha) + x\sin(\alpha))/c, \tag{4}$$

$$\tau_{rx}(z, x, x_m) = \sqrt{z^2 + (x - x_m)^2}/c, \tag{5}$$

$$\tau(z, x, x_m, \alpha) = \tau_{tx} + \tau_{rx}. \tag{6}$$

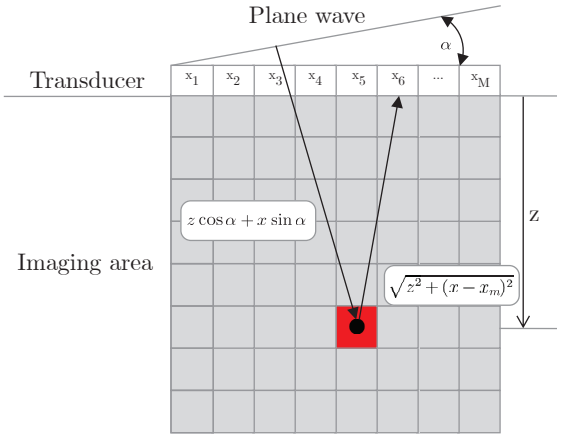

Fig. 3: Illustrating the geometry of the delay calculations in equation (4), (5) and (6).

The delay calculated in (6) can be a non-integer sample number. To get the correct signal value for every pixel we linearly interpolate between the samples such that

$$y_{m,a} = \beta u_{m,a}[s] + (1 - \beta)u_{m,a}[s + 1], \tag{7}$$

where $u_{m,a}$ is the signal recorded from element m for transmit a, $s = \lfloor \tau / f_s \rfloor$ is the sample delay calculated from the delay, τ, from equation (6) and the sampling

This article has been accepted for publication in a future issue of this journal, but has not been fully edited. Content may change prior to final publication. Citation information: DOI 10.1109/TUFFC.2019.2914555, IEEE Transactions on Ultrasonics, Ferroelectrics, and Frequency Control

frequency, f_s, while $\beta = \lceil \tau \rceil - \tau$. Eg. if a certain pixel has the delay $\tau = 15.5$ for a sample from a certain element, we simply linearly interpolate between sample 15 and 16 to get the correct value for that pixel using equation (7).

Each pixel in the image is the sum of the correctly delayed signal

$$I_{\text{DAS}}[z,x] = \sum_{a=0}^{N_\alpha - 1} \sum_{m=0}^{M-1} w_{m,a}[z,x] y_{m,a}[z,x] e^{i2\pi f_{\text{demod}} \tau / f_s}. \tag{8}$$

Here M is the number of elements, $y_{m,a}$ is the correctly delayed IQ-demodulated signal from element m and transmit a, and $w_{m,a}$ is given by

$$w_m[z,x] = \begin{cases} 1, & \text{if } |x - x_m| \leq \frac{z}{f\#} \\ 0, & \text{otherwise,} \end{cases} \tag{9}$$

where $[z,x]$ is the pixel position, x_m is the receiving element position and $f\#$ is the selected ratio between the pixel depth and the size of the aperture. Thus, $w_{m,a}$ results in an expanding dynamic aperture. This is to improve the near field and have uniform resolution throughout the image. In this study we used a constant $f\#$ of 1.7.

The multiplication with $e^{i2\pi f_{\text{demod}} \tau / f_s}$ in equation (8) up-mixes the IQ-demodulated signal. f_{demod} is the demodulation frequency, which was equal to the transmitted center frequency, τ is the delay from equation (6), and f_s is the sampling frequency. The outer sum, where N_α is the number of angular transmits, is the coherent compounding of multiple angular transmits. The correctly delayed complex amplitude for each transmit is accumulated for every pixel.

The final step in our ultrasound image processing chain is to convert the raw complex signal amplitude to a final brightness value in the image. Since the up-mixed IQ-data is the one-sided analytic signal, the envelope can easily be detected by taking the absolute value of the complex value resulting from the sum in (8). This image magnitude is then converted to decibel values. This is achieved by applying the log compression

$$I_{\text{dB}} = 20 \cdot log_{10}(|I_{\text{DAS}}|). \tag{10}$$

The image in dB is then normalized with relation to a selected maximum value, M_v,

$$I_{\text{dB norm.}} = I_{\text{dB}} - M_v, \tag{11}$$

before the values outside the desired dynamic range, D_r, are clamped

$$I_{\text{dB final}} = \begin{cases} I_{\text{dB norm.}}, & \text{if } I_{\text{dB norm.}} < -D_r \\ -D_r, & \text{otherwise.} \end{cases} \tag{12}$$

Finally, the image is normalized to gray-level values between $[0, 255]$,

$$I_{\text{grayscale}} = \left\lfloor \frac{255(I_{\text{dB final}} + D_r)}{D_r} \right\rceil, \tag{13}$$

where the $\lfloor \, \rceil$ represents a rounding to nearest integer function. The image in $I_{\text{grayscale}}$ can then finally be displayed on the screen.

E. iOS implementation

The networking and data deserialization on the iPhone is implemented in Swift 4 [42] and the beamforming and image reconstruction is written in Metal [43]. The CPU is responsible for networking and deserialization, queueing up data to be processed by the GPU using a triple-buffer of memory shared by the CPU and GPU. The channel data for each image frame is made available to the Metal GPU compute shader that is run in parallel across the GPU's cores. One compute shader thread is started for every pixel in the image. The number of pixels generated depends on the wavelength of the transmitted pulse chosen, but for an $Z \times X$ number of pixels in an ultrasound image there are $Z \times X$ threads each summing the contribution (complex sample) of the M number of channels. For the images used in this study we specifically used a pixel spacing of $\lambda/2$ resulting in $Z \times X = 307 \times 256 = 78592$ pixels since the image is 48.8 mm deep, $\lambda = 0.298$ mm, and we used 128 elements with λ spacing. The compute shader implements the beamforming such that it is described in detail in Section II-D. Thus the associated delay from each receive element to each pixel, equation (6), is calculated *on-the-fly*. Equation (7) to (9) is implemented withing a double *for-loop* over the elements M and potentially the multiple transmit angles N_α as described in equation (8). Equations (10) to (13) is implemented outside the loop with the pixel value from equation (13) written to the texture, and thus being the only value returned from each compute shader. The code for the iOS app is made available

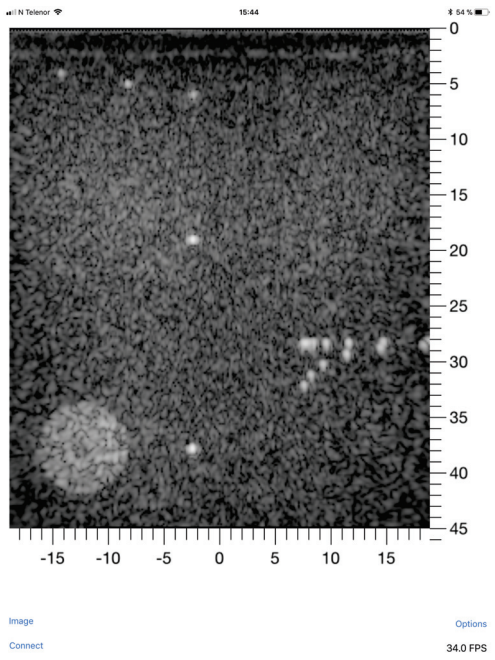

Fig. 4: Screen capture from the iPad processing three angles coherently compounded into a higher quality image at a processing rate of 34 frames per second. A demo video is available at https://youtu.be/oN8cwysGxyM.

This article has been accepted for publication in a future issue of this journal, but has not been fully edited. Content may change prior to final publication. Citation information: DOI 10.1109/TUFFC.2019.2914555, IEEE Transactions on Ultrasonics, Ferroelectrics, and Frequency Control

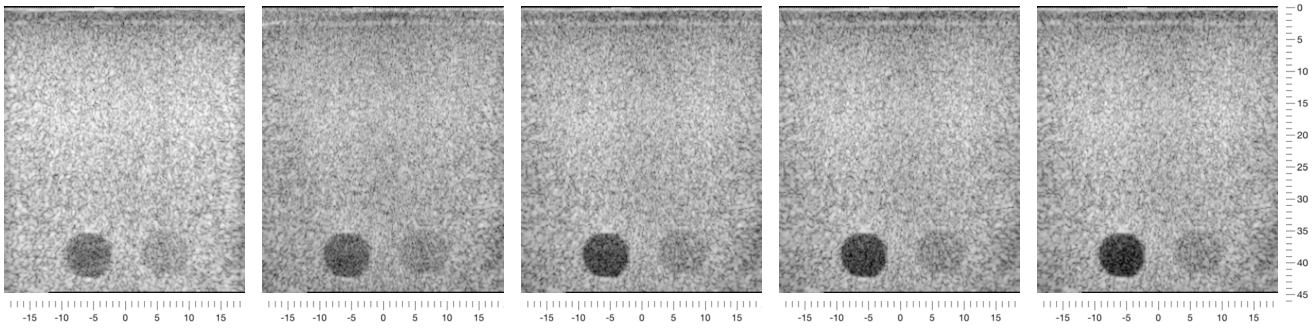

(a) 1 angle (b) 3 angles (c) 7 angles (d) 11 angles (e) 21 angles

Fig. 5: Ultrasound images dumped from the iPhone 6s imaging cysts with 1 (a), 3 (b), 5 (c), 11 (d) and 21 (e) plane waves with transmission angles uniformly distributed between ±16° coherently compounded, except the single plane wave transmitted at 0°. Notice that the contrast within the hypoechoic cyst is improved with increased number of angles coherently compounded. The images are displayed with 60 dB dynamic range. A demo video is available at https://youtu.be/oN8cwysGxyM.

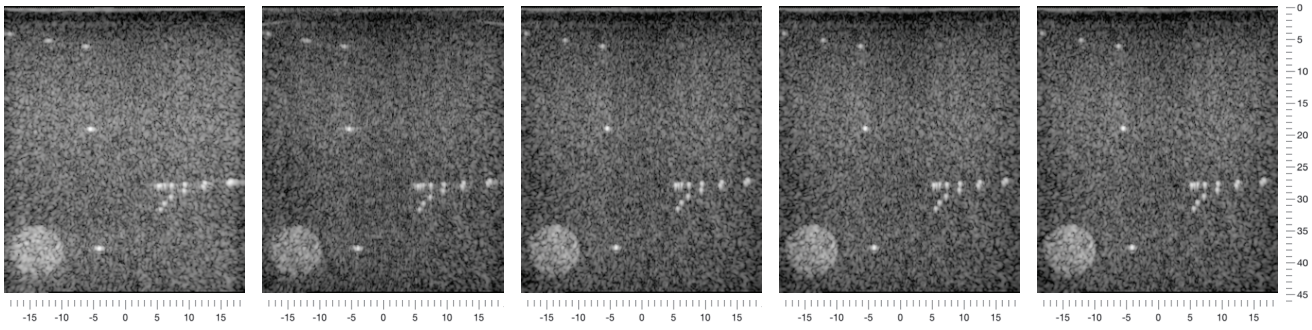

(a) 1 angle (b) 3 angles (c) 7 angles (d) 11 angles (e) 21 angles

Fig. 6: Ultrasound images dumped from the iPhone 6s imaging a hyperechoic cyst and point scatterers with 1 (a), 3 (b), 7 (c), 11 (d) and 21 (e) plane waves with transmission angles uniformly distributed between ±16° coherently compounded, except the single plane wave transmitted at 0°. Notice that the resolution of the point scatterers is improved with the increased number of angles coherently compounded. The images are displayed with 60 dB dynamic range. A demo video is available at https://youtu.be/oN8cwysGxyM.

at GitHub (https://github.com/palmerc/Beamformer) with the Metal compute shader implemented in the Beamformer.metal file (Beamformer/SmartWave/Common/Metal/Beamformer.metal).

The client interface allows for real-time dynamic adjustment of the processing variables such as the imaging depth and width, the speed of sound, c, used in equation (6), the maximum value, M_v, used in equation (11) and the dynamic range D_r used in equation (12) and (11). The image is displayed with depth and width rulers, and pinch-and-zoom of the image works as is standard for a touchscreen app.

F. Measuring frame rate

We measured the framerate at *the probe* and *the phone* separately by updating a timestamp once for every data packet sent or upon the completion of image formation. If the two framerates were approximately the same, while requiring no more than one frame to be buffered in *the phone's* processing queue, we considered the throughput frames per second (FPS) to be accurate.

The throughput frame rate will vary, and to get a stable estimate we ran each test for three minutes after the connection between *the probe* and *the phone* were established and the processing of the data had begun.

III. Results

Fig. 1 shows the full setup of the ultrasound probe imaging a CIRS phantom 054GS (CIRS, Norfolk, VA) with the research scanner streaming the channel data wirelessly through the router before it is received, beamformed and displayed on the iPhone. Fig. 4 shows a screen dump from the iPad Pro of an image created from three angles coherently compounded at 34 FPS. The screen dump also illustrates the width and depth rulers.

Fig. 5 shows the ultrasound images dumped from the iPhone 6s imaging cysts with 1 (a), 3 (b), 7 (c), 11 (d)

This article has been accepted for publication in a future issue of this journal, but has not been fully edited. Content may change prior to final publication. Citation information: DOI 10.1109/TUFFC.2019.2914555, IEEE Transactions on Ultrasonics, Ferroelectrics, and Frequency Control

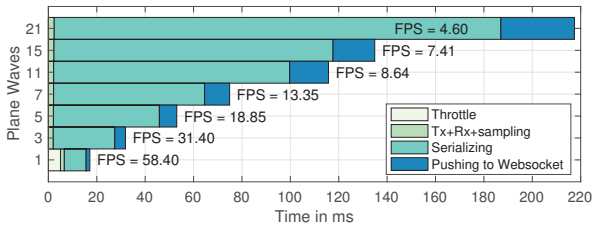

Fig. 7: The timing diagram of the processing in the probe when transmitting to the iPhone. Thus, detailing the amount of time spent on respectively transmitting and receiving data (Tx+Rx+sampling), serializing the data into the packet and the amount of time to push the web packet to the WebSocket. Notice that when transmitting one PW we had to throttle the acquisition to get an FPS lower than 60, since the screen refresh rate for the iPhone is maximum 60 FPS. This was not needed when transmitting for the iPad Pro

and 21 (e) plane waves with transmission angles uniformly distributed between ±16° coherently compounded. Notice that the contrast within the hypoechoic cyst is improved with an increased number of angles coherently compounded. Fig. 6 shows the ultrasound images dumped from the iPhone 6s imaging a hyperechoic cyst and point scatterers with 1 (a), 3 (b), 7 (c), 11 (d) and 21 (e) plane waves with transmission angles uniformly distributed between ±16° coherently compounded. Note that the resolution of the point scatterers is improved with the increased number of angles coherently compounded.

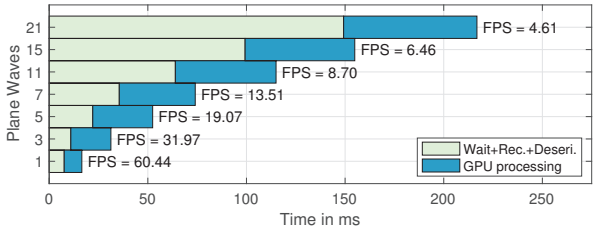

Fig. 8: A timing diagram of the processing in the device, measured for the iPhone X. Detailing the amount of time spent waiting for a new packet to arrive, receiving the packet and deserializing it, and the portion spent in the GPU processing the data.

Fig. 7 shows the timing diagram of the processing in *the probe*, detailing the amount of time spent on respectively transmitting and receiving data (Tx+Rx+sampling), serializing the data packet and the amount of time to push the packet into the WebSocket. Note that a significant amount of time is spent serializing the data. Also notice that we perform throttling on the single PW acquisition with the iPhones to slow down the frame rate to below 60 FPS because of the maximum screen refresh rate of 60 Hz. However, the iPad has, as stated earlier, a variable refresh rate up to 120 Hz and thus no throttling was necessary. See the IV. Discussion for more details.

Fig. 8 shows the timing diagram of the processing in *the phone*, detailing the amount of time spent waiting for a new packet to arrive, receiving the packet and deserializing it, and the time portion spent in the GPU processing the data. Notice that GPU processing is not consuming the largest share of the time, it is actually waiting for, receiving and deserializing the web packet that takes most of the time.

Fig. 9 plots the frame rates achieved for different numbers of angles. As expected higher frame rates are achieved when processing and compounding images with fewer angles. Frame rates of roughly 60 FPS are achieved for all the iPhones tested in the single angle case, and nearly 90 FPS for the iPad Pro, see the IV. Discussion section for details on this particular result. A frame rate of approximately 9 FPS is achieved on most devices while compounding up to 11 plane waves. The exception is the iPhone 6s where we saw performance drop off faster than for the other devices.

In Fig. 10a the average size of the data packet for each angle transferred over the network and received for processing on the device is plotted both before and after serialization.

Fig. 10b shows the amount of data processed per second in the system, thus taking the network packet size shown in Fig. 10a and multiplying it by the frame rate achieved by the iPhone X. Notice that the data processing rate is equal for all angles except for the single angle case, which was lower because of the throttling necessary to keep the frame rate below 60 FPS.

Also note that that a demo video is available at https://youtu.be/oN8cwysGxyM.

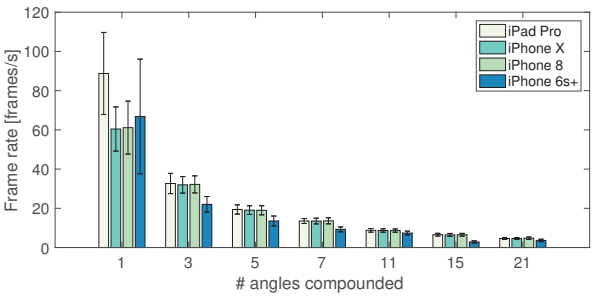

Fig. 9: The throughput processing frame rate as measured on the devices indicated by the legend. These frame rates are made sure to approximately correspond to the frame rate measured in the probe as detailed in Section II-F. As expected the frame rate drops as the number of angles that are processed and compounded increases.

IV. Discussion

The setup described in our study is capable of handling real-time ultrasound imaging with the data wirelessly transmitted from *the probe* to *the phone* doing all processing from IQ-demodulated and downsampled data to the full reconstructed image. This is illustrated in Fig. 9 where we can observe that real-time frame rates are achieved

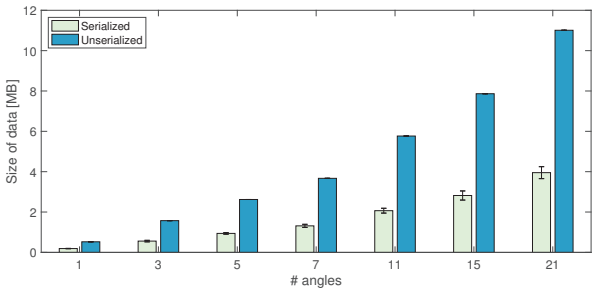

(a) Average network packet size for the different number of angles

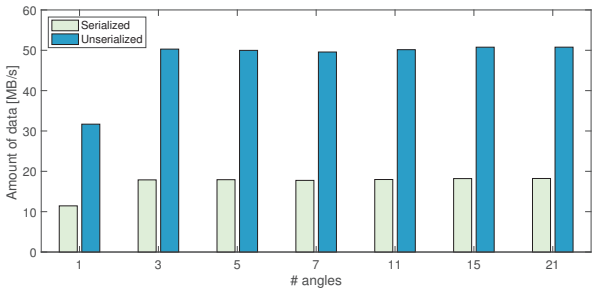

(b) Data processing rates for the different number of angles

Fig. 10: The size of the data packet for each angle transferred over the network and received for processing on the device is plotted both before and after serialization in (a). The amount of data processed per second in the system, thus when taking the average network packet size from (a) and multiplying it by the frame rate achieved by the iPhone X is shown in (b). The data processing rate is equal for all angles except for the single angle case, which was lower because of the throttling necessary to keep the frame rate below 60 FPS. The large difference between the size of the serialized and unserialized data is most likely because limitations in the Java-based serialization library forced the use of four-byte integers, where arguably two-byte integers would be sufficient. Thus, much of the data before serialization was redundant.

for all devices. Fig. 7 illustrates that most of the processing time in *the probe* is spent serializing the data, and only a fraction of the time is spent actually transmitting and receiving the ultrasound signal (Tx+Rx+Sampling). When comparing Fig. 7 and Fig. 8 we see that the frame rates achieved are approximately similar and thus, from Section II-F, we can trust the framerates measured. A conventional definition of real time computing is a system able to finish a task before the scheduled deadline [44]. If we define the deadline in our system as when the channel data for the next image frame arrives on *the phone*, we are doing real time processing, since *the phone* is processing the data as fast as *the probe* can push data over the network. However, by closely investigating Fig. 8 we can observe that a significant amount of time is spent waiting on, receiving and deserializing the data while a smaller portion is spent in the GPU processing the data. This observation indicates that the bottleneck in the system is the serialization of the data in *the probe*.

There is little latency in the system, meaning that the image produced on *the phone* is very responsive when moving the probe back and forth on the phantom, as demonstrated in the video available at https://youtu.be/oN8cwysGxyM.

The implementation of the serialization could potentially be improved. Our implementation is done in software calling a Java library from MATLAB since the Verasonics Vantage research scanner only gives access to the channel data buffers through MATLAB. An implementation in a lower level language, or a hardware implementation, accessing the buffers directly could possibly speed up the serialization avoiding the bottleneck in the current setup. Using a different serialization type other than Protobufs could potentially solve the issue with serialization.

The average network packet size, displayed in Fig. 10a increases as expected when the data from more angles are included in the packet. When we calculate the average amount of data processed per second in Fig. 10a, we see that we are transmitting and processing less than 20 MB/s of serialized data (approximately 50 MB/s unserialized). The theoretical bandwidth of the 802.11ac wireless router is 1733 Mb/s (216.62 MB/s). The bandwidth value is highly dependent on the surrounding RF environment and the type of wireless hardware on the client. In a real RF environment, we cannot expect to sustain more than 400 Mbps in good conditions. Our setup was measured, using iPerf [39], to perform in the 400-500 Mbps range. Still, we are transmitting less than 20 MB/s (160 Mbps) using less than 10% of the theoretical bandwidth, once again indicating that the serialization of the data is the bottleneck in the pipeline and not the wireless networking.

Notice that the iPad had a significantly higher processing frame rate for a single PW, while the iPhone X, 8 and 6s was limited to approximately 60 FPS. This is because only the iPad has the capability of screen refresh rates higher than 60 FPS using the ProMotion technology as mentioned in Section II-B. Therefore, we had to throttle *the probe* by adding an additional delay in the Tx+Rx+sampling part of the processing to match the fixed screen refresh rate of 60 FPS when transmitting to the iPhones. If this is not done, the devices are not able to keep up the real-time processing since the data starts to buffer, and a large and growing latency in the processing chain is introduced. This also explains the dip in the first bar in Fig. 10a indicating less data processed per second for the one angle case. However, for the case of the iPad Pro, the processing was equal for all angles.

It is also worth pointing out that we are not observing any processing improvements between the iPad Pro, the iPhone X and iPhone 8 when more than one angle is compounded, even though the iPhone X and iPad Pro have a different GPU compared to the iPhone 8. This is probably because the bottleneck in the serialization in *the probe* leads to a significant amount of the processing time in *the phone* is spent waiting and thus the GPU performance is not a differentiating factor for the frame-

rates achieved. This means that there is a surplus of GPU processing power, a surplus one can expect to increase with the next generation of iOS devices. If the serialization can be improved this surplus can be spent on compounding more angles at a higher frame rate, or one could potentially exploit the surplus by implementing more sophisticated beamforming techniques, such as adaptive beamforming, for higher quality ultrasound images. By having the software beamforming fully implemented on an off-the-shelf device, one can exploit improvements in the hardware, achieving higher quality ultrasound images by simply updating the software in *the phone* while still receiving the same data in the *the probe*.

Heating of *the phone* might be an issue when processing extensively on the CPU and GPU. We ran our test for three minutes on each device and did not observe any issues with heating, except for the iPhone 6s where we, as mentioned, saw some performance drop that could be because of heating. However, since, from Fig. 8 most of the processing time in *the phone* is spent waiting, receiving and deserializing the data in the CPU before the GPU starts to process neither the GPU nor the CPU are run consecutively - reducing the risk of throttling because of heating. The issue with heating is also reduced in the latest generation of devices where the performance is improved dramatically, and also the "sustained performance" without heating is greatly improved [45].

We chose to use a wireless connection, first and foremost because a wireless connection gives the most portable and durable device. Also, with technologies such as Wi-Fi Direct [46], a high speed connection between portable devices such as an ultrasound probe and *the phone* is possible. Wi-Fi Direct is known to have transfer rates up to 250 Mbps (31.25 MB/s) [47] and thus could support our current transfer rate. Whether such transfer rates are possible between two hand-held devices are somewhat uncertain. However, we believe it is safe to speculate that the transfer rates of Wi-Fi Direct will become higher in the future exploiting new Wi-Fi standards such as 802.11ac, as well as miniaturization of improved technology. Wi-Fi Direct is in fact already in use in the hand-held Clarius ultrasound scanner [21], using it to transfer the beamformed ultrasound image to a smartphone to be displayed [48]. A cabled connection could, of course, also provide higher bandwidths with technologies such as USB 3.0 with transfer rates up to 5 Gbit/s (625 MB/s). A wired connection, in addition to the drawbacks of limiting movement of the probe and potentially broken cables, requires specific drivers and potentially licensing for each device the probe can be connected to. Choosing a wireless transfer also fits into current technology trends with more and more devices becoming wireless [49].

The image quality in Fig. 5 and Fig. 6 confirms that the image quality is improved, in terms of contrast and resolution, with the number of plane waves coherently compounded. However, the image quality is not improved linearly with the number of angles, the improvement is dominated more with the inclusion of the first angles, thus going from a single PW to three, while the improvement is less significant going from e.g. 11 PWs to 21 PWs. This is in agreement with [29]. Our setup using coherent plane wave imaging allows a trade-off between image quality and frame rate. However, one could argue that by coherently compounding 7 angles the image quality is good enough for simple, clinically valuable imaging. Since coherent compounding of 7 angles results in a frame rate of 13 frames per second one can argue that we are capable of doing real-time imaging with clinically valuable image quality in clinical cases of slow moving body parts such as the thyroid, the eye, lymph nodes and some abdominal scanning. However, we also expect to see improvements in both image quality and frame rates with technological improvements in processing power, transfer rates and more sophisticated beamforming techniques.

V. Conclusion

We have demonstrated real-time, coherent plane wave compounded, ultrasound imaging with the processing handled by *off-the-shelf* devices such as the iPhone and iPad Pro. The frame rates achieved are dependent on the number of angles compounded, resulting in a trade-off between image quality and frame rate. Frame rates of $\approx$ 60 FPS were achieved for single PW imaging on the iPhones, while $\approx$ 90 FPS was achieved for the iPad Pro. When compounding 7 angles, a frame rate of 13 frames per second was achieved on all devices tested (iPad Pro, iPhone X and iPhone 8) except for the iPhone 6s+ which only achieved 9 FPS.

The bottleneck in the current system was identified as the serialization of the data in *the probe*, thus higher frame rates are possible with the current setup by improving the data serialization performance. However, the frame rates and image quality achieved might be good enough for simpler medical clinical ultrasound imaging of e.g. the carotid artery or thyroid. Since the beamforming can be moved to an *off-the-shelf* device this can reduce the specialized hardware necessary and lower the price of a hand-held system and aiding the democratization of medical ultrasound imaging.

Acknowledgment

The authors would like to thank Andreas Austeng, professor at the University of Oslo, for support and technical discussions during this study, and especially for proofreading and improving the manuscript. We would also like to thank Thomas Hansen, senior engineer at the University of Oslo for assisting in providing and setting up Apple products making this research possible. We would also like to thank Promon AS, Oslo, Norway for providing Apple devices and the wireless equipment for this study. This study was partially financed by Center for Innovative Ultrasound Solutions (CIUS) and the Research Council of Norway, Project Code 237887.

References

[1] S. Lafitte, N. Alimazighi, P. Reant, M. Dijos, A. Zaroui, A. Mignot, M. Lafitte, X. Pillois, R. Roudaut, and A. DeMaria, "Validation of the Smallest Pocket Echoscopic Device's Diagnostic Capabilities in Heart Investigation," *Ultrasound in Medicine and Biology*, vol. 37, no. 5, pp. 798–804, 2011.

[2] C. Prinz and J. U. Voigt, "Diagnostic accuracy of a hand-held ultrasound scanner in routine patients referred for echocardiography," *Journal of the American Society of Echocardiography*, vol. 24, no. 2, pp. 111–116, 2011.

[3] E. Godt. (2015) Handheld ultrasound a heartbeat away from ousting the stethoscope? [Online]. Available: http://www.cardiovascularbusiness.com/topics/imaging/handheld-ultrasound-heartbeat-away-ousting-stethoscope

[4] General Electric Healtcare, Vingmed Ultrasound. Vivid E95 cSound. [Online]. Available: http://www3.gehealthcare.com/en/products/categories/ultrasound/vivid/vivid_e95

[5] Supersonic Imagine. AiXplorer. [Online]. Available: https://www.supersonicimagine.com

[6] O. Rindal, S. Aakhus, S. Holm, and A. Austeng, "Hypothesis of Improved Visualization of Microstructures in the Interventricular Septum with Ultrasound and Adaptive Beamforming," *Ultrasound in Medicine and Biology*, vol. 43, no. 10, pp. 2494–2499, 2017.

[7] M. A. Lediju Bell, R. Goswami, J. A. Kisslo, J. J. Dahl, and G. E. Trahey, "Short-Lag Spatial Coherence (SLSC) Imaging of Cardiac Ultrasound Data: Initial Clinical Results," *Ultrasound in medicine & biology*, vol. 39, no. 10, pp. 1861–1874, 2013.

[8] A. Wiacek, O. M. H. Rindal, E. Falomo, K. Myers, K. Fabrega-Foster, S. Harvey, and M. A. Bell, "Robust Short-Lag Spatial Coherence Imaging of Breast Ultrasound Data: Initial Clinical Results," *IEEE Transactions on Ultrasonics, Ferroelectrics, and Frequency Control*, vol. 66, no. 3, pp. 527–540, 2018.

[9] G. Matrone, A. S. Savoia, G. Caliano, S. Member, and G. Magenes, "The Delay Multiply and Sum Beamforming Algorithm in Ultrasound B - Mode Medical Imaging," *IEEE Trans. Med. Imaging*, vol. 34, no. 4, pp. 1–10, 2015.

[10] P. C. Li and M. L. Li, "Adaptive imaging using the generalized coherence factor," *IEEE Transactions on Ultrasonics, Ferroelectrics, and Frequency Control*, vol. 50, no. 2, pp. 128–141, 2003.

[11] J. Camacho, M. Parrilla, and C. Fritsch, "Phase coherence imaging," *IEEE Transactions on Ultrasonics, Ferroelectrics, and Frequency Control*, vol. 56, no. 5, pp. 958–974, 2009.

[12] D. Hyun, G. E. Trahey, and J. Dahl, "A GPU-based real-time spatial coherence imaging system," in *Medical Imaging 2013: Ultrasonic Imaging, Tomography, and Therapy*, vol. 8675, Mar. 2013, p. 86751B.

[13] J. P. Åsen, J. I. Buskenes, C.-I. C. Nilsen, A. Austeng, and S. Holm, "Implementing Capon Beamforming on a GPU for Real-Time Cardiac Ultrasound Imaging." *IEEE Transactions on Ultrasonics, Ferroelectrics and Frequency Controlltrasonics*, vol. 61, no. 1, jan 2014.

[14] B. Y. S. Yiu and A. C. H. Yu, "GPU-based minimum variance beamformer for synthetic aperture imaging of the eye," *Ultrasound in Medicine and Biology*, vol. 41, no. 3, pp. 871–883, 2015.

[15] T. Su, D. J. Yao, D. Y. Li, and S. Zhang, "Ultrasound parallel delay multiply and sum beamforming algorithm based on gpu," in *2nd IET International Conference on Biomedical Image and Signal Processing (ICBISP 2017)*, May 2017, pp. 1–4.

[16] E. Boni, A. C. Yu, S. Freear, J. A. Jensen, and P. Tortoli, "Ultrasound open platforms for next-generation imaging technique development," *IEEE Transactions on Ultrasonics, Ferroelectrics, and Frequency Control*, vol. 65, no. 7, pp. 1078–1092, 2018.

[17] J. Joseph. N.J. EMS Agency Reviews New Whole-Body Ultrasound Device. [Online]. Available: https://emsworld.com/article/1221833/nj-ems-agency-reviews-new-whole-body-ultrasound-device

[18] Butterfly Network Inc. Butterfly IQ. [Online]. Available: https://www.butterflynetwork.com

[19] General Electric Healtcare, Vingmed Ultrasound. Vscan Family. [Online]. Available: http://www3.gehealthcare.com/en/products/categories/ultrasound/vscan_family

[20] Siemens Medical Solutions USA, Inc. ACUSON Freestyle Ultrasound System. [Online]. Available: https://usa.healthcare.siemens.com/ultrasound/ultrasound-point-of-care/acuson-freestyle-ultrasound-system

[21] Clarius. Clarius. [Online]. Available: https://www.clarius.me

[22] Koninklijke Philips N.V. Lumify. [Online]. Available: https://www.lumify.philips.com/

[23] J. Kortbek, J. A. Jensen, and K. L. Gammelmark, "Sequential beamforming for synthetic aperture imaging," *Ultrasonics*, vol. 53, no. 1, pp. 1–16, 2013.

[24] M. C. Hemmsen, T. Kjeldsen, L. Lassen, C. Kjær, B. Tomov, J. Mosegaard, and J. A. Jensen, "Implementation of synthetic aperture imaging on a hand-held device," *2014 IEEE International Ultrasonics Symposium (IUS) Proceedings*, pp. 2177–2180, 2014.

[25] T. Di Ianni, M. Hemmsen, P. Llimós Muntal, I. H. H. Jørgensen, and J. Jensen, "System-level Design of an Integrated Receiver Front-end for a Wireless Ultrasound Probe," *IEEE Transactions on Ultrasonics, Ferroelectrics, and Frequency Control*, vol. 63, no. 11, pp. 1935–1946, 2016.

[26] T. Di Ianni, C. Armando, V. Hoyos, C. Ewertsen, T. K. Kjeldsen, J. Mosegaard, M. B. Nielsen, and J. A. Jensen, "A Vector Flow Imaging Method for Portable Ultrasound Using Synthetic Aperture Sequential Beamforming," *IEEE Transactions on Ultrasonics, Ferroelectrics, and Frequency Control*, vol. 64, no. 11, pp. 1655–1665, 2017.

[27] T. Di Ianni, T. Kjeldsen, C. Hoyos, J. Mosegaard, and J. Jensen, "Real-time implementation of synthetic aperture vector flow imaging in a consumer-level tablet," *IEEE International Ultrasonics Symposium, IUS*, vol. 2, pp. 1–4, 2017.

[28] M. Tanter and M. Fink, "Ultrafast imaging in biomedical ultrasound," *IEEE Transactions on Ultrasonics, Ferroelectrics, and Frequency Control*, vol. 61, no. 1, pp. 102–119, 2014.

[29] G. Montaldo, M. Tanter, J. Bercoff, N. Benech, and M. Fink, "Coherent plane-wave compounding for very high frame rate ultrasonography and transient elastography." *IEEE Transactions on Ultrasonics, Ferroelectrics, and Frequency Control*, vol. 56, no. 3, pp. 489–506, Mar. 2009.

[30] J. Y. Lu, "Experimental study of high frame rate imaging with limited diffraction beams." *IEEE transactions on ultrasonics, ferroelectrics, and frequency control*, vol. 45, no. 1, pp. 84–97, 1998.

[31] D. Garcia, L. L. Tarnec, S. Muth, E. Montagnon, J. Porée, and G. Cloutier, "Fourier f - k Migration for Plane Wave Ultrasound Imaging : Theoretical Framework," *IEEE Trans on Ultrasonics, Ferroelectrics, and Frequency Control*, vol. 60, no. 9, pp. 2141–2144, 2012.

[32] C. Chen, G. A. Hendriks, R. J. van Sloun, H. H. Hansen, and C. L. de Korte, "Improved Plane Wave Ultrasound Beamforming by Incorporating Angular Weighting and Coherent Compounding in Fourier Domain," *IEEE Transactions on Ultrasonics, Ferroelectrics, and Frequency Control*, vol. 65, no. 5, pp. 749–765, 2018.

[33] Apple Inc. Accelerate Framework. [Online]. Available: https://developer.apple.com/documentation/accelerate

[34] T. Chernyakova and Y. Eldar, "Fourier-domain beamforming: The path to compressed ultrasound imaging," *IEEE Transactions on Ultrasonics, Ferroelectrics, and Frequency Control*, vol. 61, no. 8, pp. 1252–1267, 2014.

[35] C. L. Palmer, O. M. H. Rindal, S. Holm, and A. Austeng, "Realtime plane-wave software beamforming with an iPhone," *IEEE International Ultrasonics Symposium, IUS*, pp. 1–4, 2016.

[36] H. Hewener and S. Tretbar, "Mobile ultrafast ultrasound imaging system based on smartphone and tablet devices," *2015 IEEE International Ultrasonics Symposium, IUS 2015*, pp. 1–4, 2015.

[37] P. Kaczkowski, "Bandwidth Sampling Data Acquisition with the Vantage System for High Frequency Transducers," *Verasonics Inc. White Paper*, 2016.

[38] S. Caldwell. Apple's promotion is going to change how we use our devices. [Online]. Available: https://www.imore.com/promotion

[39] ESnet and Lawrence Berkeley National Laboratory. iPerf. [Online]. Available: www.https://iperf.fr

[40] Google Inc., Mountain View, CA, USA. Protocol buffers. [Online]. Available: https://developers.google.com/protocol-buffers/

[41] IETF Zeroconf Working Group. Zero Configuration Networking (Zeroconf). [Online]. Available: www.https://Zeroconf.org

[42] Apple Inc. Swift. [Online]. Available: https://developer.apple.com/swift/
[43] ——. Metal. [Online]. Available: https://developer.apple.com/metal/
[44] K. G. Shin and P. Ramanathan, "Real-Time Computing: A New Discipline of Computer Science and Engineering," *Proceedings of the IEEE*, vol. 82, no. 1, pp. 6–24, 1994.
[45] Andrei Frumusanu. The iPhone XS & XS Max Review: Unveiling the Silicon Secrets). [Online]. Available: https://www.anandtech.com/show/13392/the-iphone-xs-xs-max-review-unveiling-the-silicon-secrets/7
[46] Wi-Fi Alliance. Wi-Fi Direct. [Online]. Available: https://www.wi-fi.org/discover-wi-fi/wi-fi-direct
[47] ——. How fast is Wi-Fi Direct? [Online]. Available: https://www.wi-fi.org/knowledge-center/faq/how-fast-is-wi-fi-direct
[48] K. Dickie, "White Paper: Wireless Ultrasound," *White Paper Clarius*, pp. 1–4, 2019. [Online]. Available: https://clarius.com/education/white-papers/wireless-ultrasound
[49] A. C. Estes. The Future of Wireless Everything. [Online]. Available: https://gizmodo.com/the-future-of-wireless-everything-1794814613

Cameron Lowell Palmer was born in Dallas, Texas, USA in 1974. He received his B.Sc. and M.Sc. degrees in Computer Science from the University of North Texas, Denton, Texas. Currently, he is pursuing the Ph.D. degree with the Department of Circulation and Medical Imaging, NTNU. His research interests include medical applications of augmented reality, real-time mobile beamforming, and automatic quantitative evaluation of diagnostic imagery.

Ole Marius Hoel Rindal was born in Hamar, Norway in 1990. He received the M.S degree in computer science (signal processing) in 2014 from the University of Oslo, Oslo, Norway. Since 2014 he has been working on his PhD at the University of Oslo, working with medical ultrasound beamforming techniques. He also holds a position at the Centre for Elite Sports Research, at the Norwegian University of Science and Technology, Trondheim, Norway, doing research on signal processing on inertial measurement units used in cross-country skiing. His research interest includes signal processing, medical image formation, image processing, machine learning, physiological and biomechanical aspects of cross-country skiing.

Paper IV

Double Adaptive Plane-Wave Imaging

Ole Marius Hoel Rindal and Andreas Austeng

Published in *IEEE International Ultrasonics Symposium, IUS,* (2016), 1–4. doi: 10.1109/ULTSYM.2016.7728906

IV

Paper V

Signal Coherence and Image Amplitude With the Filtered Delay Multiply and Sum Beamformer

Fabrice Prieur, Ole Marius Hoel Rindal and Andreas Austeng

Published in *IEEE Transactions on Ultrasonics, Ferroelectrics, and Frequency Control,* (2018), 65 (7): 1133–1140. doi: 10.1109/TUFFC.2018.2831789.

This paper was among Editor's Selection of Articles on Receive Beamforming in IEEE Transactions on Ultrasonics, Ferroelectrics, and Frequency Control - February 2019 Edition.

V

Paper VI

The Dark Region Artifact in Adaptive Ultrasound Beamforming

Ole Marius Hoel Rindal, Alfonso Rodriguez-Molares and Andreas Austeng

Published in *IEEE International Ultrasonics Symposium, IUS,* (2017), 1–4.
doi: 10.1109/ULTSYM.2017.8092255

VI

Erratum: On page 118 in the left column it should be "... estimate the spatial covariance matrix". There is a typo spelling coherence instead of covariance.

Paper VII

The Effect of Dynamic Range Alterations in the Estimation of Contrast

Ole Marius Hoel Rindal, Andreas Austeng, Ali Fatemi and Alfonso Rodriguez-Molares

Accepted for publication in *IEEE Transactions on Ultrasonics, Ferroelectrics, and Frequency Control*, (2019), 1–11. doi: 10.1109/TUFFC.2019.2911267.

VII

The effect of dynamic range alterations in the estimation of contrast

Ole Marius Hoel Rindal, *Student Member IEEE*, Andreas Austeng, *Member IEEE*, Ali Fatemi, *Student Member IEEE* and Alfonso Rodriguez-Molares, *Member IEEE*

***Abstract*—Many adaptive beamformers claim to produce images with increased contrast, a feature that could enable a better detection of lesions and anatomical structures.**

Contrast is often quantified using the contrast ratio (CR), and the contrast to noise ratio (CNR). The estimation of CR and CNR can be affected by dynamic range alterations (DRA), such as those produced by a trivial gray-level transformation. Thus, we can form the hypothesis that contrast improvements from adaptive beamformers can, partly, be due to dynamic range alterations.

In this paper we confirm this hypothesis. We show evidence on the influence of DRA on the estimation of CR and CNR, and on the fact that several methods in the state-of-the-art do alter the dynamic range.

To study this phenomenon, we propose a dynamic range test (DRT) to estimate the degree of DRA and we apply it to 7 beamforming methods. We show that CR improvements correlate with DRT with R^2-adj=0.88 in simulated data and R^2-adj=0.98 in experiments. We also show that DRA may lead to increased CNR values, under some circumstances.

These results suggest that claims on lesion detectability, based on CR and CNR values, should be revised.

Keywords*—Adaptive beamforming, Dynamic range, Contrast Metrics, Capon's Minimum Variance, Eigenspace Based Minimum Variance, Filtered-Delay-Multiply-And-Sum, Coherence Factor, Generalized Coherence Factor, Phase Coherence Factor.

I. Introduction

THE popularization of software beamforming has brought numerous techniques that, by clever manipulation of channel data, are able to exceed the contrast and resolution provided by conventional delay-and-sum (DAS) beamforming. We refer as adaptive beamforming to any technique where the signal values alter the way the beamformed signal is constructed, for instance when the element weights are determined from the variance of the signal.

Seminal work on adaptive beamforming dates back to the 1960s, where optimal element weights were derived for a given signal direction to minimize the influence of jamming signals in radio communication systems [1]–[4].

Adaptive beamforming was first applied to medical ultrasound at the end of the 1980s to compensate for phase aberration artifacts produced by tissue inhomogeneities [5], [6], and about a decade later to reduce the contribution of off-axis targets [7]–[11]. Since then, the number of articles on adaptive beamforming has increased exponentially [12].

Among the alleged benefits of adaptive techniques is that of producing increased contrast, a feature that is often associated with higher lesion detectability. Extraordinary increases in contrast ratio (CR), and in contrast to noise ratio (CNR), with respect to DAS, are reported in the literature [13]–[18].

Another way of increasing image contrast is by altering the dynamic range (DR) of the beamformed images. This is achieved, for instance, by applying a gray-level transformation of the image intensity values which can stretch or compress the dynamic range. Gray-level-transforms have traditionally been used in commercial scanners to emphasize certain characteristics of the investigated tissues. This operation does not provide new information or better lesion detection, but it can increase the apparent contrast of the image. This has been known for some time, and it has previously been stated that "any nonlinear postprocessing [...] would be merely cosmetic", and that it "does not affect the intrinsic detectability of low contrast lesions, [...] at least for the ideal observer" and only "slight gains for real observers" [19]. However, these findings seems to be forgotten in the modern ultrasound community. And the question then arises on whether some of the alleged benefits of adaptive beamforming could be explained by a DR transformation that is unaccounted for. If that is the case, then some of the reported values for CR and CNR in the literature should be revised.

In [20] we proposed a phantom to measure the output dynamic range produced by any beamforming algorithm. Using synthetic data, we showed that some adaptive algorithms seem to transform the DR, which in turn affected the estimated CR values. Here we extend the analysis to CNR, include 4 additional adaptive beamforming techniques, include the effect on vertical gradients, and validate the result with experimental data. We also define a dynamic range test (DRT) that makes it possible to quantify the degree of DR alterations.

In Section II we present the algorithms under study. In Section III we review the current contrast quality metrics, present the DR phantoms used both in simulation and in experiments, describe data processing, and introduce the dynamic range test. Results are presented in Section IV and discussed in Section V. Conclusions and further work are included in Section VI.

II. Theory

Without loss of generality let us assume a linear array of M elements, laying on the x-axis, pointing towards the positive

Rindal and Austeng are affiliated with the Research Group for Digital Signal Processing and Image Analysis, Department of Informatics, University of Oslo, Oslo, Norway (e-mail: omrindal@ifi.uio.no).

Fatemi and Rodriguez-Molares are affiliated with the Department of Circulation and Medical Imaging, Norwegian University of Science and Technology, Trondheim, Norway.

Manuscript received June 12th, 2018; revised January 8th and March 13th, 2019.

This article has been accepted for publication in a future issue of this journal, but has not been fully edited. Content may change prior to final publication. Citation information: DOI 10.1109/TUFFC.2019.2911267, IEEE Transactions on Ultrasonics, Ferroelectrics, and Frequency Control

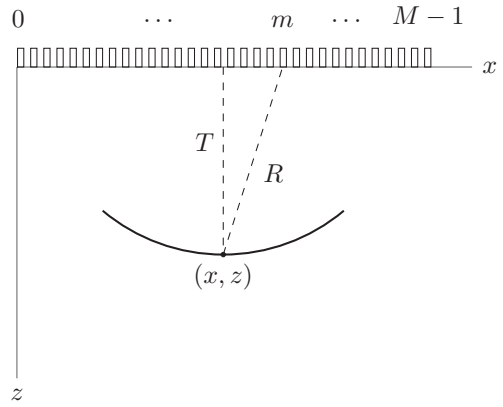

Fig. 1: Geometrical illustration of the posed scenario.

direction of the z-axis, as illustrated in Fig. 1. The domain, with characteristic sound speed c_0, is illuminated by a generic transmit beam, either planar, converging or diverging. Let us denote the signal received by element m as $h_m(t)$. Let us denote as T the distance from the origin of the transmitted wave to the point (x, z), and as R the distance from (x, z) to the location of element m. If we apply the propagation delay, $\Delta t = (T+R)/c_0$, we obtain the signal value at (x, z) received by element m,

$$s_m = h_m(t)|_{t=\Delta t}\,, \tag{1}$$

also referred to as *pixel value*. Note that we drop the spatial coordinates (x, z). The symbol s_m refers to the pixel value at an arbitrary location (x, z), unless otherwise specified.

A. Delay-and-sum (DAS)

The conventional DAS implementation is the coherent combination of the pixel values as received by all elements, yielding

$$b_{\text{DAS}} = \sum_{m=0}^{M-1} w_m s_m, \tag{2}$$

where w_m is the receive apodization, a static term often determined from the F-number and the pixel depth z. Equation (2) can be written in algebraic form as

$$b_{\text{DAS}} = \boldsymbol{w}^H \boldsymbol{s}, \tag{3}$$

where $\boldsymbol{s} = [s_0\ s_1\ \ldots\ s_{M-1}]$ is a vector containing the pixel value for every channel in the system.

B. Capon's Minimum Variance (MV)

Capon's Minimum Variance (MV) technique calculates a data dependent set of weights $\boldsymbol{w}$ while maintaining unity gain in the steering direction [21]. This is posed as a minimization problem by

$$\begin{aligned} \min_{\boldsymbol{w}}\ E\left\{|b_{\text{DAS}}|^2\right\} &= \boldsymbol{w}^H \boldsymbol{R} \boldsymbol{w} \\ \text{subject to } \boldsymbol{w}^{\boldsymbol{H}} \boldsymbol{a} &= \mathbf{1}, \end{aligned} \tag{4}$$

where $\mathbf{R} \equiv E\left\{\boldsymbol{s}\boldsymbol{s}^H\right\}$ is the spatial covariance matrix, E is the expected value operator, and the steering vector $\boldsymbol{a} = \mathbf{1}$ because it is assumed that all signals are already delayed. The solution to (4) can by found by the method of Lagrange multipliers, yielding

$$\boldsymbol{w}_{\text{MV}} = \frac{\boldsymbol{R}^{-1}\boldsymbol{a}}{\boldsymbol{a}^H \boldsymbol{R}^{-1} \boldsymbol{a}}. \tag{5}$$

The spatial covariance matrix is unknown, but it can be estimated for point (x, z), assuming a linear array, by [21]

$$\hat{\boldsymbol{R}}(x,z) = \frac{\sum_{k=-K}^{K} \sum_{l=0}^{M-L} \overline{\boldsymbol{s}}_l(x, z-k)\, \overline{\boldsymbol{s}}_l^H(x, z-k)}{(2K+1)(M-L+1)}, \tag{6}$$

where $(2K+1)$ is the number of axial samples, L is the length of the subarray, and

$$\overline{\boldsymbol{s}}_l(x,z) = \left[s_l(x,z) \quad s_{l+1}(x,z) \quad \ldots \quad s_{l+L-1}(x,z)\right]^T. \tag{7}$$

The subarray averaging improves robustness. To further improve robustness, and numerical stability, diagonal loading is added to the estimated covariance matrix by $\hat{\boldsymbol{R}}(x,z) = \hat{\boldsymbol{R}}(x,z) + \epsilon\mathbf{I}$, where $\mathbf{I}$ is the identity matrix, and

$$\epsilon = \frac{\Delta}{L} tr\{\hat{\boldsymbol{R}}(x,z)\},$$

where $tr\{\}$ is the trace operator.

The beamformed image is then computed as

$$b_{\text{MV}} = \frac{1}{M-L+1} \sum_{l=0}^{M-L} \boldsymbol{w}_{\text{MV}}^H\, \overline{\boldsymbol{s}}_l. \tag{8}$$

C. Eigenspace-Based Minimum Variance (EBMV)

The MV can be extended into EBMV. In 2010, Asl et al. [22] was the first to apply it to beamforming for medical ultrasound. They utilized the eigenstructure of the covariance matrix aiming to obtain a better suppression of off-axis signals. The covariance matrix is estimated with (6) and eigendecomposed as

$$\hat{\boldsymbol{R}}_{\text{DL}} = \boldsymbol{V}\boldsymbol{\Lambda}^{-1}\boldsymbol{V}^H, \tag{9}$$

where $\boldsymbol{\Lambda} = [\lambda_1, \lambda_2, ..., \lambda_L]^T$ are the eigenvalues in descending order, and $\boldsymbol{V} = [\boldsymbol{v}_1, \boldsymbol{v}_2, ...\boldsymbol{v}_L]$ are the corresponding eigenvectors. The signal subspace $\boldsymbol{E}_s$ can be constructed using the eigenvectors corresponding to the largest eigenvalues,

$$\boldsymbol{E}_s = [\boldsymbol{v}_1, ..., \boldsymbol{v}_E], \tag{10}$$

where E is the number of eigenvectors creating the signal subspace. Finally, the EBMV weight is obtained by projecting the conventional MV weights onto the constructed signal subspace

$$\boldsymbol{w}_{\text{EBMV}} = \boldsymbol{E}_s \boldsymbol{E}_s^H \boldsymbol{w}_{\text{MV}}. \tag{11}$$

The beamformed image is then computed as

$$b_{\text{EBMV}} = \frac{1}{M-L+1} \sum_{l=0}^{M-L} \boldsymbol{w}_{\text{EBMV}}^H\, \overline{\boldsymbol{s}}_l, \tag{12}$$

with $\overline{\boldsymbol{s}}_l$ defined as in (7).

D. Filtered-delay-multiply-and-sum (F-DMAS)

F-DMAS for medical ultrasound beamforming was introduced by Matrone et al. in 2015 [23]. The technique aims to increase image quality by multiplying the RF signals before summation. Namely, the signed square root signal is defined as

$$g_{ij} = \text{sign}\,(s_i s_j)\sqrt{|s_i s_j|}, \tag{13}$$

where sign$(\cdot)$ denotes the sign function. The beamformed signal $b_{\text{F-DMAS}}$ is then computed as

$$b_{\text{F-DMAS}} = \left[\sum_{i=0}^{M-2}\sum_{j=i+1}^{M-1} g_{ij}\cdot\right]_{\text{BPF}}, \tag{14}$$

where $[\cdot]_{\text{BPF}}$ denotes the band pass filtering of the signal inside the brackets. Note that (13) is the multiplication of two signals with identical center frequency f_c, and hence it will have two frequency components: one at 0, and one at $2f_c$. Band pass filtering is applied to remove the DC component.

E. Coherence Factor (CF)

The CF was first introduced by Mallart and Fink in 1994 [24], as the ratio between the coherent and incoherent energy across the aperture:

$$\text{CF} = \frac{\left|\sum_{m=0}^{M-1} s_m\right|^2}{M\sum_{m=0}^{M-1}|s_m|^2}. \tag{15}$$

The CF has been used as an adaptive weight to increase image quality [25] as;

$$b_{\text{CF}} = \text{CF}\, b_{\text{DAS}}. \tag{16}$$

F. Generalized Coherence Factor (GCF)

In 2003 Li et al. generalized the coherence factor as [25]

$$\text{GCF} = \frac{\sum_{n<M_0}|S_n|^2}{\sum_{n=-\frac{M}{2}}^{\frac{M}{2}-1}|S_n|^2}, \tag{17}$$

where S is the M-point Fourier spectra over the aperture of the delayed channel data,

$$S_n = \sum_{m=0}^{M-1} s_m e^{-j2\pi(m-M/2)d\frac{n}{Md}}, \tag{18}$$

where $n \in [-\frac{M}{2}, \frac{M}{2}-1]$ is the spatial frequency index where M is assumed to be even, d is the pitch of the array, and M_0 is an arbitrary constant within $[0, \frac{M}{2}-1]$ that specifies the low spatial frequency region, thus going from $-M_0$ to M_0. Note that if $M_0 = 0$ the GCF simplifies to the CF.

The beamformed image is computed by multiplying the DAS image with GCF

$$b_{\text{GCF}} = \text{GCF}\, b_{\text{DAS}}. \tag{19}$$

G. Phase Coherence Factor (PCF)

The PCF was introduced by Camacho et al. in 2009 [26] as

$$\text{PCF} = \max\left\{0, 1 - \frac{\gamma}{\sigma_0}p\right\}, \tag{20}$$

where γ is a parameter to adjust the sensitivity of PCF to out-of-focus signals, $\sigma_0 = \pi/\sqrt{3}$ is the nominal standard deviation of a uniform distribution between $-\pi$ and π, and p is given by

$$p = \min\left\{\sigma\left(\boldsymbol{\phi}\right), \sigma\left(\boldsymbol{\phi}^A\right)\right\}, \tag{21}$$

where $\boldsymbol{\phi} = [\phi_1\ \phi_2 \ldots \phi_M]$ is the instantaneous phase across the aperture, and $\sigma(\boldsymbol{\phi})$ is its standard deviation. To avoid phase wrapping discontinuity a set of auxiliary phases $\boldsymbol{\phi}^A = [\phi_1^A\ \phi_2^A \ldots \phi_M^A]$ is computed as

$$\phi_m^A = \begin{cases}\phi_m + \pi & \text{if } \phi_m < 0,\\ \phi_m - \pi & \text{otherwise.}\end{cases} \tag{22}$$

The beamformed image is computed using PCF as an adaptive weight

$$b_{\text{PCF}} = \text{PCF}\, b_{\text{DAS}}. \tag{23}$$

H. Gray level transformation (GLT)

For completeness we include a gray level transformation (GLT) to illustrate how a trivial transformation of the DR can affect the estimation of contrast. In particular, beamformed images are transformed using a sigmoid function (S-curve):

$$\hat{p}(B) = \frac{1}{1+e^{-\alpha(B-\beta)}} \tag{24}$$

$$p(B) = \frac{\hat{p}(B) - \max\left(\hat{p}(B)\right)}{\epsilon}, \tag{25}$$

where the coefficients α, β and ϵ are defined in Section III-D, and where $B = 20\log_{10}(|b_{\text{DAS}}|)$. The plot of the S-curve is shown in Fig. 2.

Notice that the suggested S-curve compresses the signal intensity in the [-30, 0] dB interval, effectively making the light regions more uniform, and stretches the DR from -30 dB and downwards, effectively making the dark regions even darker.

III. Materials and Methods

A. Image quality metrics

No clear consensus exists yet on how to measure the contrast of ultrasound images. Perhaps the most widespread definition [14], [23], [27] is the one in [28],

$$\text{CR} = \frac{\mu_{\text{ROI}}}{\mu_{\text{B}}}, \tag{26}$$

where $\mu = E\left\{|b|^2\right\}$ is the expected value of the power of the beamformed signal, in linear scale, over a certain region; and where ROI and B denote, respectively, a region of interest and a background region. If the signal power is proportional to the back-scattering coefficient, which is the case for speckle signals beamformed with DAS, then CR is proportional to the

This article has been accepted for publication in a future issue of this journal, but has not been fully edited. Content may change prior to final publication. Citation information: DOI 10.1109/TUFFC.2019.2911267, IEEE Transactions on Ultrasonics, Ferroelectrics, and Frequency Control

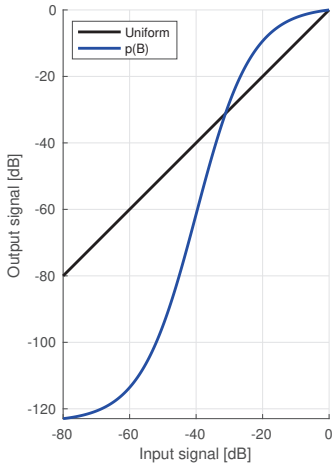

Fig. 2: Gray-level-transform (GLT) S-curve (24) in *log space*.

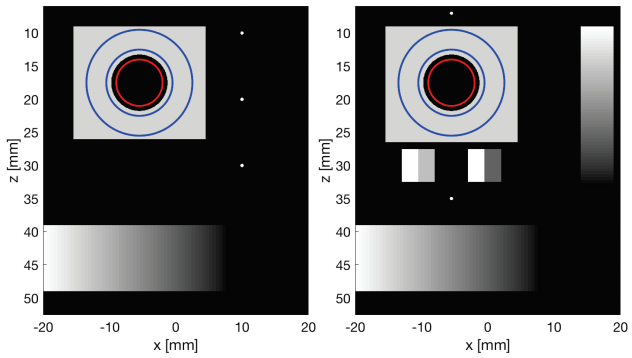

(a) Experimental (b) Simulated

Fig. 3: Experimental and simulated dynamic range phantoms shown with 60 dB dynamic range.

ratio of the particle concentration in both regions. CR, often referred to as contrast ratio, can be expressed in logarithmic scale as,

$$\mathrm{CR}[\mathrm{dB}] = 10\log_{10}\mathrm{CR}. \tag{27}$$

Detection probability not only depends on the mean value of the signal power but also on its variance. An alternative measure of contrast can be found in [29], a measure that became later known as the contrast-to-noise ratio

$$\mathrm{CNR} = \frac{|\mu_{\mathrm{ROI}} - \mu_{\mathrm{B}}|}{\sqrt{\sigma^2_{\mathrm{ROI}} + \sigma^2_{\mathrm{B}}}}, \tag{28}$$

where $\sigma = \sqrt{E\left\{(|b|^2 - \mu)^2\right\}}$ is the standard deviation of the power of the beamformed signal, in linear scale. CNR is an estimate of the detection probability of a lesion. In particular for the case of circularly-symmetric Gaussian distributed signals, which is the case of speckle signals beamformed with DAS, CNR is bounded to the interval $[0, 1]$. This metric has been used by many authors [14], [16], [23], [27].

Even though the expressions (26) and (28) were originally proposed to be applied to signal power in natural units, many authors have chosen to insert log-compressed values in them, effectively defining the alternative metrics:

$$\mathrm{CR}_{\mathrm{LC}}[\mathrm{dB}] = |\tilde{\mu}_{\mathrm{ROI}} - \tilde{\mu}_{\mathrm{B}}|, \tag{29}$$

where $\tilde{\mu} = E\left\{20\log_{10}(|b|)\right\}$ is the expected value of the log-compressed values within the ROI and B region, and

$$\mathrm{CNR}_{\mathrm{LC}}[\mathrm{dB}] = \frac{|\tilde{\mu}_{\mathrm{ROI}} - \tilde{\mu}_{\mathrm{B}}|}{\sqrt{\tilde{\sigma}^2_{\mathrm{ROI}} + \tilde{\sigma}^2_{\mathrm{B}}}}, \tag{30}$$

where $\tilde{\sigma} = \sqrt{E\left\{(20\log_{10}(|b|) - \tilde{\mu})^2\right\}}$ is the standard deviation of the log-compressed signal within the ROI and B region. We include the subindex LC to denote the metrics computed on log-compressed values.

Although (29) is similar to (27), they are not identical since $10\log_{10}\left(E\left\{|b|^2\right\}\right) \neq E\left\{20\log_{10}(|b|)\right\}$. CNR and $\mathrm{CNR}_{\mathrm{LC}}$ take completely different values, and cannot be directly compared. Although both are thought to be estimates of the lesion detection probability, $\mathrm{CR}_{\mathrm{LC}}$ can take values larger than 1, even for speckle signal beamformed with DAS. Several authors [13], [16], [22], [30], [31] have chosen (29) and (30) to quantify contrast.

In some articles [14], [15], [17], [25], [26], [32] it is not explicit whether logarithmic or natural units have been used. In some others variations of the classical definitions are used [17], [22], [31].

B. Experimental data

One element synthetic transmit aperture imaging (STAI) datasets are used. 204 STAI dataset were recorded with a Verasonics Vantage 256 system (Verasonics, Kirkland, WA, USA) and an L-11 linear array (128 element, 300 µm-pitch) transmitting at 5.28 MHz. The probe was mounted on a 3D position system Physik Instrumente (Physik Instrumente (PI) GmbH Co. KG, Karlsruhe, Germany) with a minimum incremental motion of 0.1 µm.

Several tissue mimicking targets were made following the instructions in Annex II of IEC60601-2-37 [33] and cut into the following shapes

1) T1: A 20 × 17 mm block with a 8.5 mm diameter circular hole,
2) T2: a 2 × 10 mm block.

In addition a 200 µm nylon line was used as wire target.

The targets were placed in a water tank at 23°C. The 3D positioning system allowed us to control the target relative position respect to the probe. Multiple datasets were recorded separately, in particular

1) A dataset was recorded with T1 centered at (-5.5, 17.5) mm;
2) 200 datasets were recorded with T2 placed at $z = 44$ mm depth with x raging from -20 to 20 mm to be combined into the lateral gradient;

This article has been accepted for publication in a future issue of this journal, but has not been fully edited. Content may change prior to final publication. Citation information: DOI 10.1109/TUFFC.2019.2911267, IEEE Transactions on Ultrasonics, Ferroelectrics, and Frequency Control

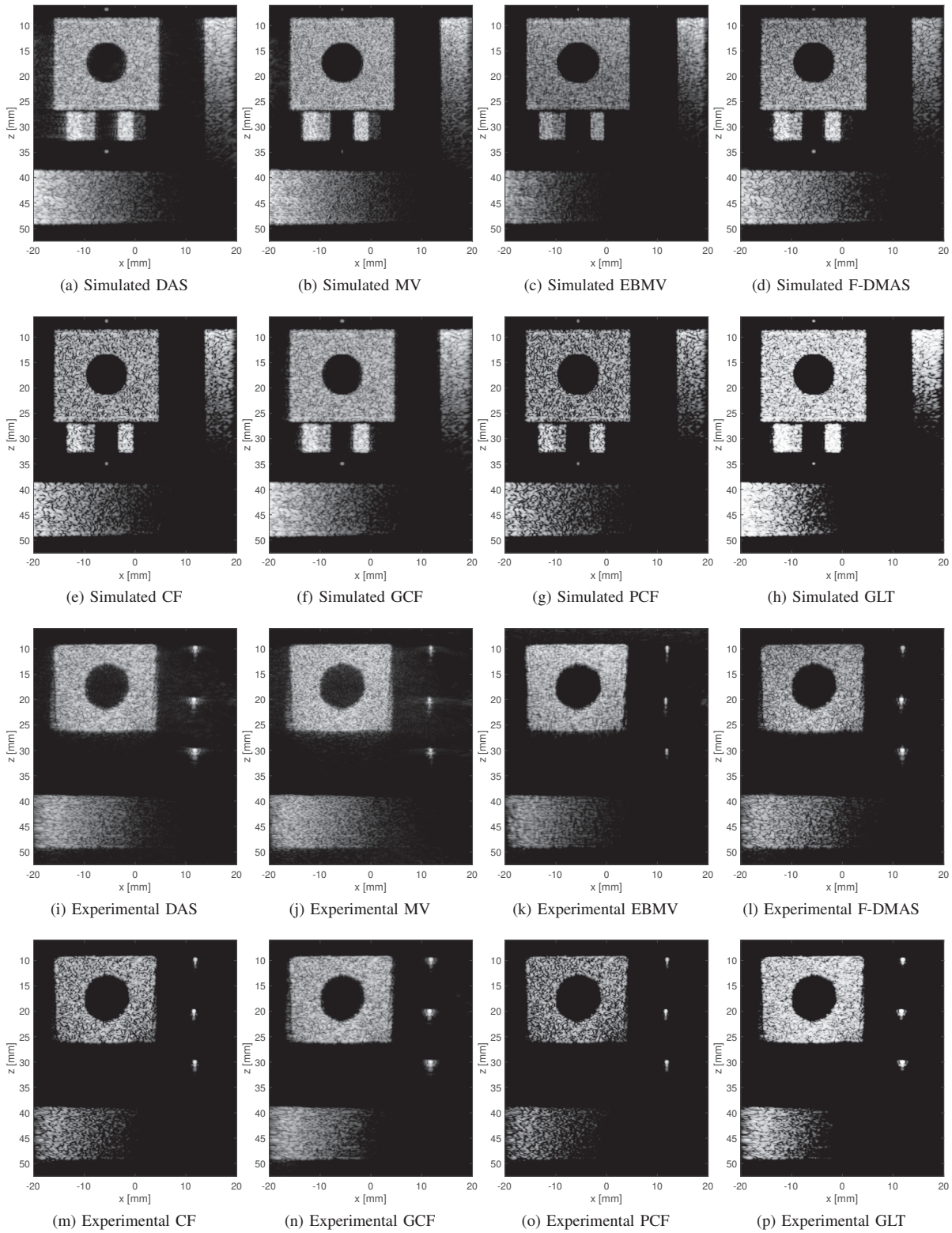

(a) Simulated DAS (b) Simulated MV (c) Simulated EBMV (d) Simulated F-DMAS

(e) Simulated CF (f) Simulated GCF (g) Simulated PCF (h) Simulated GLT

(i) Experimental DAS (j) Experimental MV (k) Experimental EBMV (l) Experimental F-DMAS

(m) Experimental CF (n) Experimental GCF (o) Experimental PCF (p) Experimental GLT

Fig. 4: Images of the simulated phantom (a-h) and the experimental phantom (i-p) for all beamformers under study. The images are shown with 60 dB dynamic range.

This article has been accepted for publication in a future issue of this journal, but has not been fully edited. Content may change prior to final publication. Citation information: DOI 10.1109/TUFFC.2019.2911267, IEEE Transactions on Ultrasonics, Ferroelectrics, and Frequency Control

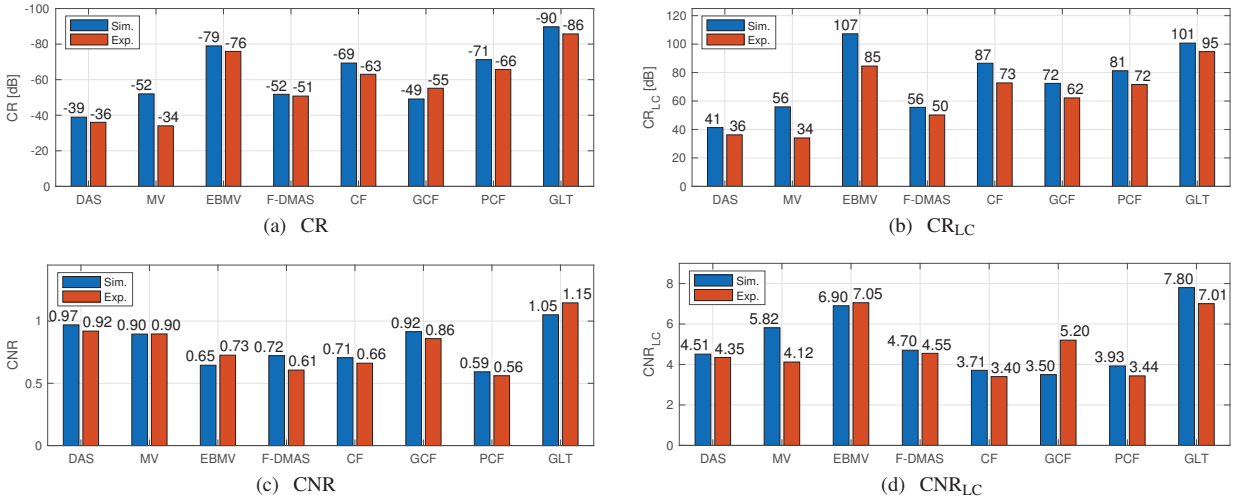

Fig. 5: Measured contrast of the simulated and the experimental hypoechoic cyst at (-5.5, 17.5) mm using all contrast metrics as defined in Section III-A.

3) 3 additional datasets were recorded with the wire target at $x = 12$ mm and depth $z = [10, 20, 30]$ mm.

The 204 datasets were normalized in amplitude and combined into a single dataset via weighted addition of RF channel data. Weights were selected so as to produce a final gradient of 1.8 dB/mm, covering the normalized range $[0, -50]$ dB from -14 to 14 mm. Note that this operation is done on RF channel data, and hence before any beamforming operation. The gradient from $[0, -50]$ dB, -14 to 14 mm was selected to avoid unwanted effects from the edges of the image, and ensure that the gradient was linear. The ROI used for contrast estimation is shown in Fig. 3a circumscribed by the red circle, while the background area is shown between the two blue circles. The experimental dataset is available for download from http://www.USTB.no/publications/dynamic_range/.

C. Simulated data

A dataset was generated using Field II [34], [35]. A 128 element, 300 µm-pitch linear probe was simulated transmitting a 2.5 cycle Gaussian-modulated sinusoidal pulse with a center frequency of 5.13 MHz. Element height was set to $\lambda/2$ to produce a uniform field of view and rule out the effect of elevation focusing [36].

A phantom was designed to match the experimental dataset as close as possible. The simulated phantom is shown in Fig. 3b, consisting of point targets, a hypoechoic cystic region, and two bands with monotonically decreasing speckle intensity:

1) a 10 mm wide lateral gradient at z = 44 mm depth, of 1.8 dB/mm covering a normalized scattering intensity range of $[0, -50]$ dB from x = -14 mm to x = 14 mm; and
2) a 5 mm wide axial gradient at x = 16.5 mm in the azimuth direction, of 1.8 dB/mm covering a normalized scattering intensity range of $[0, -50]$ dB from z = 10 to z = 39 mm. The axial gradient is not present in the experimental data.

In addition, and different from the experimental dataset, four rectangular speckle regions are placed at z = 30 mm depth with intensities 0, -10, 0, and -35 dB to help the discussion of the results. We ensure well developed speckle [37] using 650 scatterers per mm^3. The scatters are placed on a 2D plane using Gaussian random amplitude to mimic positions in elevation. The ROI used for the contrast estimation is circumscribed by the red circle in Fig. 3b, while the background region is that between the two blue circles. The simulated dataset can be downloaded from http://www.USTB.no/publications/dynamic_range/.

D. Data processing

Both the simulated and experimental datasets were beamformed with the UltraSound ToolBox (USTB) [38] using a dynamic expanding aperture with F-number 1.75 and a rectangular window, both in transmit and receive.

All the transmit signals were delayed and combined, to produce globally focused images. The beamformers described in Section II were applied only on the receive channels.

Some of the algorithms have user-settable parameters. For MV, L was set to 50% of the active receive channels, $K = 1.5\lambda$, and a diagonal loading factor of $\Delta = 1/100$ was used as suggested in [21]. The number of eigenvectors used in EBMV was selected adaptively using the eigenvectors with eigenvalues larger than $\delta = 0.5$ times the maximum eigenvalue as suggested in [22]. For GCF the value $M_0 = 2$ was used as suggested in [25]. For PCF $\gamma = 1$ was chosen as suggested in [26]. For the S-curve in the GLT algoritm we used $\alpha = 0.12, \beta = -40$ and $\epsilon = 0.008$.

The sound speed in the simulation was 1540 m/s, while for the experimental dataset 1470 m/s was used. All images were compensated to obtain uniform speckle intensity

This article has been accepted for publication in a future issue of this journal, but has not been fully edited. Content may change prior to final publication. Citation information: DOI 10.1109/TUFFC.2019.2911267, IEEE Transactions on Ultrasonics, Ferroelectrics, and Frequency Control

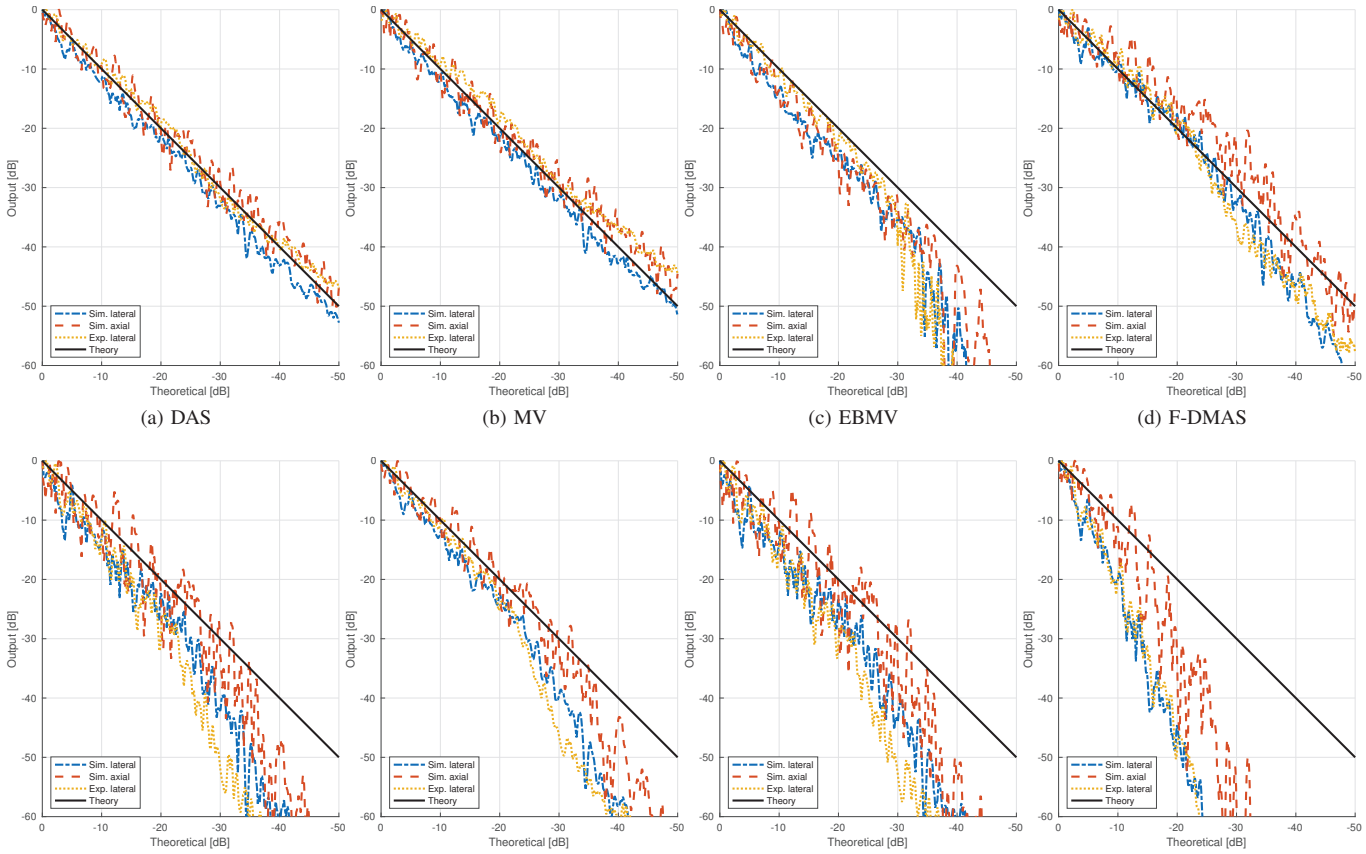

(a) DAS (b) MV (c) EBMV (d) F-DMAS

(e) CF (f) GCF (g) PCF (h) GLT

Fig. 6: The normalized average response of both the axial and lateral gradient for the simulation and the lateral gradient for the experimental data plotted against the theoretical response. The simulated axial gradient is measured between z = 10 to z = 38 mm, while the simulated and experimental lateral gradient is measured between x = -14 to x = 14 mm.

in the whole field of view. This was done differently in the simulated and experimental data. In the simulation an analytical compensation was used that accounted for the focal depth and element directivity. Details on this compensation are given in [36] together with data and code. In the experiment, the compensation was carried out empirically. An uniform block of Agar was imaged, with fully developed speckle, and the estimated intensity field was spacially averaged and inverted. Both processes could be seen as a software time gain compensation performed on a uniform reference.

The beamforming grid was 1024 $\times$ 2048 pixels to cover the demands of F-DMAS in the axial direction, since F-DMAS produce a frequency component at $2f_c$, and of MV in the lateral direction [39]. The code used to beamform the images and reproduce all the results in this manuscript is available at http://www.USTB.no/publications/dynamic_range/ for MATLAB (The MathWorks, Natick, MA, USA).

E. Dynamic Range Test (DRT)

With gradients in both the simulated and experimental dataset, we can define a *dynamic range test* (DRT) as

$$\text{DRT} = \frac{\Delta}{\Delta_0}, \tag{31}$$

where Δ denotes the gradient of a given beamforming method, estimated via linear regression, and Δ_0 denotes the theoretical gradient, as fixed in the simulated and experimental data. DRT measures how many dB the output dynamic range deviates from the theoretical, for each dB of the input dynamic range.

For the simulated dataset we have both an axial and a lateral gradient and DRT can be estimated for both. For simplicity, the reported DRT value will be the average of the DRT in the axial and lateral direction. For the experimental dataset DRT is estimated in the lateral gradient.

The datasets and code to perform the test are available at http://www.USTB.no/publications/dynamic_range/.

This article has been accepted for publication in a future issue of this journal, but has not been fully edited. Content may change prior to final publication. Citation information: DOI 10.1109/TUFFC.2019.2911267, IEEE Transactions on Ultrasonics, Ferroelectrics, and Frequency Control

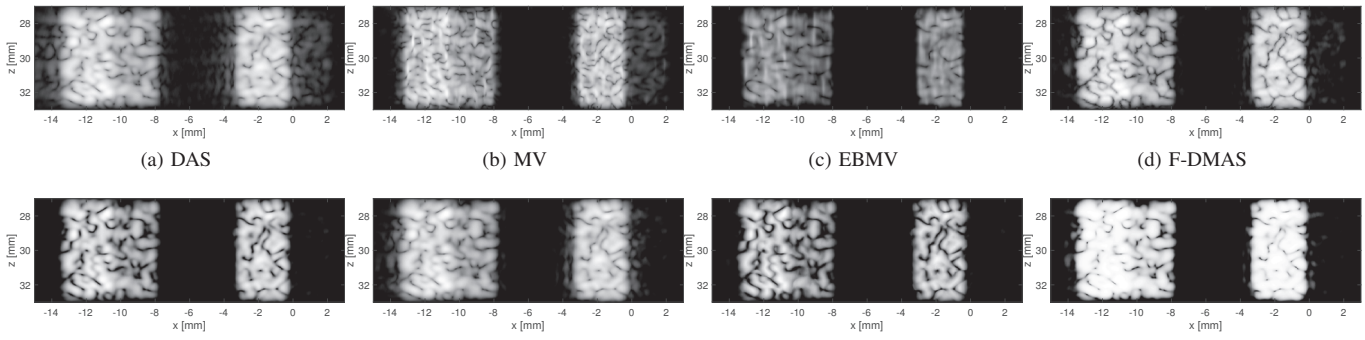

(a) DAS (b) MV (c) EBMV (d) F-DMAS

(e) CF (f) GCF (g) PCF (h) GLT

Fig. 7: Enlarged images of part of the simulated image containing speckle regions with two smaller speckle regions with a difference in echogenicity of 10 dB, left, and 35 dB, right. The images are shown with 60 dB dynamic range. Notice, that the speckle region between x = -0.5 to x = 2 mm is present in the DAS and MV image, partly visible in the F-DMAS, GCF and GLT image but completely gone for EBMV, CF, and PCF image.

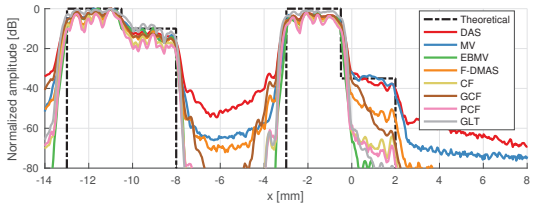

Fig. 8: The average lateral response through the speckle regions shown in Fig. 7

IV. Results

The images produced by all the methods in Section II are shown in Fig. 4, for both simulated (Fig. 4a-4h), and experimental (Fig. 4i-4p) data.

Fig. 5 shows the contrast of the hypoechoic cyst, for both simulated and experimental data, using the metrics in Section III-A and for all methods under study. As expected we observe a good correlation between CR and CR_{LC} for all methods and data type, while CNR and CNR_{LC} are not obviously correlated.

The method showing the highest CR and CR_{LC} is GLT followed by EBMV, CF, or PCF. GLT also shows the best CNR, followed by DAS and GCF. GLT has the highest CNR_{LC} followed by EBMV, and MV.

To study how each of the studied methods altered the DR, the mean intensity profile along the gradients was computed, and it is shown in Fig. 6. Simulated and experimental data are plotted in the same figure against the ground truth.

In general we see a good agreement between simulated and experimental results. As expected DAS follows the ground truth closely. MV shows also a good agreement, while EBMV abruptly drops at -30 dB. F-DMAS shows a slight compression of the DR within 0 and -25 dB, and DR stretching from -25 dB and downwards. The other adaptive beamformers (CF, GCF, and PCF) show a similar output dynamic range that stretches the dynamic range from -20 dB and downwards.

To illustrate how DR transformations can affect the visibility of clinically relevant structures we included four speckle regions in the simulated phantom, with backscattering intensity of 0, -10, 0, and -35 dB, shown in Figs. 7a-7h in a 60 dB dynamic range. The average lateral response through the speckle regions are shown in Fig. 8. The four speckle regions are easily observed in the DAS, and MV images. The visibility of the -35 dB region is significantly reduced in the F-DMAS, GCF, and GLT images; while the region is completely removed in the EBMV, CF, and PCF images.

For completeness we have included examples of the full dynamic range test defined in Section III-E for DAS, EBMV and CF for the simulated dataset in Fig. 9a-9c and the experimental dataset in Fig. 9d-9f. The region used to estimate the gradient is indicated with the dashed color in the B-mode image, and plotted in the subplot with the corresponding color. The theoretical and estimated gradient are in the subplot. In Fig. 9g the DRT values, the ratio between the estimated and the theoretical gradient, is plotted for all beamformers.

V. Discussion

All the studied adaptive beamformers produce higher contrast ratio than DAS as measured by (26) or (29), with the exception of MV which only improves the contrast in the simulated case. However, one can get an arbitrarily high contrast using the trivial GLT, as shown in Figs. 5a and 5b. This proves that higher CR does not necessarily mean better image quality or better lesion detection.

Using the classical definition of contrast to noise ratio given in (28), we observe that GLT holds the highest value. Again this proves the point that a trivial transformation of DR can lead to increased CNR values.

If the definition in (30) is used, GLT have a slightly higher value than EBMV. This proves that DR transformations can alter the estimation of CNR, and that a higher CNR does not necessarily mean better lesion detectability.

This article has been accepted for publication in a future issue of this journal, but has not been fully edited. Content may change prior to final publication. Citation information: DOI 10.1109/TUFFC.2019.2911267, IEEE Transactions on Ultrasonics, Ferroelectrics, and Frequency Control

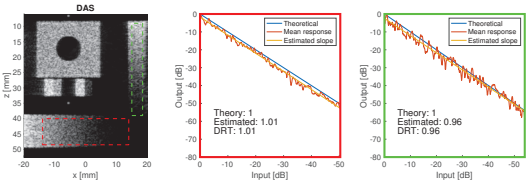

(a) Simulated DAS

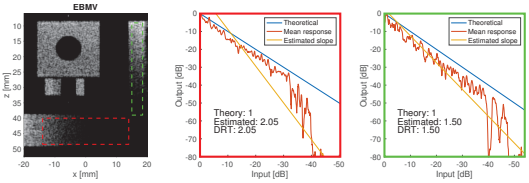

(b) Simulated EBMV

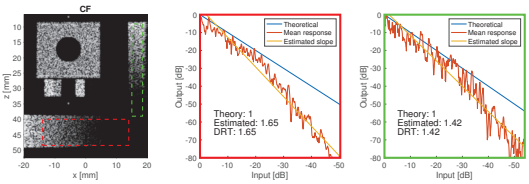

(c) Simulated CF

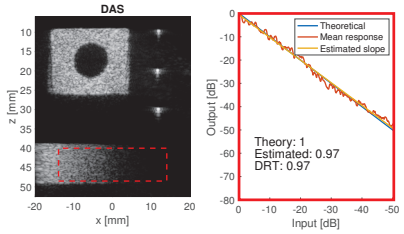

(d) Experimental DAS

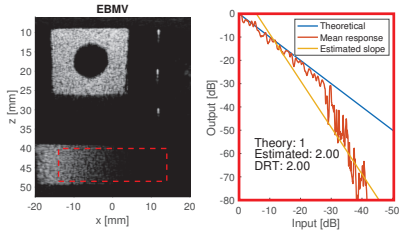

(e) Experimental EBMV

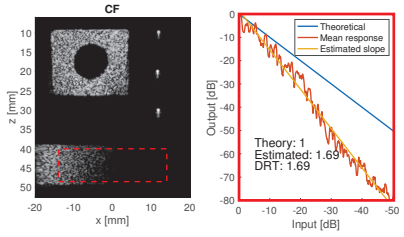

(f) Experimental CF

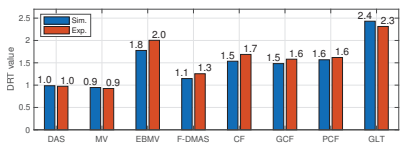

(g) DRT values for all beamformers

Fig. 9: Examples of the dynamic range test (DRT) defined in Section III-E. (a) to (c) show DAS, EBMV and CF on the simulated dataset, while (d) to (f) are on experimental data. (g) shows the resulting DRT value for all beamformers.

Using the suggested DRT we observe that EBMV, F-DMAS, CF, GCF, PCF and GLT all produce DR stretching. This is evident from Fig. 6 where we observe that only the DAS and MV follow the linear drop of the horizontal intensity gradient. The test reveals the DR transformation curves associated with each technique: EBMV has an abrupt drop between -30 and -35 dB; while F-DMAS, CF, GCF, PCF and GLT have a parabolic curve that stretches the region below -20 dB. We observe that the gradient of the curve is notably smaller for F-DMAS, which fits the findings in [40]. From the examples of the DRT in Fig. 9, and the resulting gradients in Fig. 6, we can observe that the resulting gradients for most of the beamformers seems to be of higher orders than a linear line. However, a linear line is suitable as an intuitive indicator to determine if a beamformer is alternating the DR. And thus, the DRT values, plotted in Fig. 9g, provides a quantitative indication of the DR alteration of the beamformer. It should also be mentioned that the selected dynamic range of the gradient will affect the resulting DRT values, and that we chose the largest dynamic range possible while still maintaining a linear gradient in the experimental data.

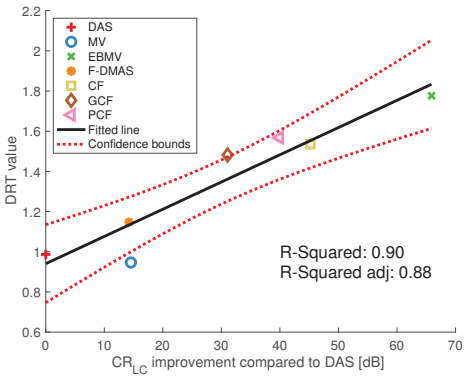

(a) Simulation

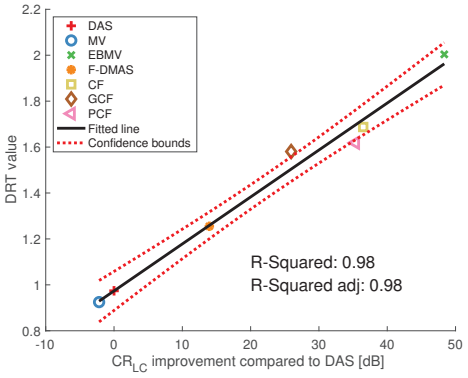

(b) Experiment

Fig. 10: The improvement in CR_{LC} compared to DAS plotted against the dynamic range test value which is the ratio between the estimated and the theoretical gradient. The results from the simulated data in (a) and the experimental in (b).

This article has been accepted for publication in a future issue of this journal, but has not been fully edited. Content may change prior to final publication. Citation information: DOI 10.1109/TUFFC.2019.2911267, IEEE Transactions on Ultrasonics, Ferroelectrics, and Frequency Control

We observe that the increase in $\mathrm{CR_{LC}}$ with respect to that of DAS seems to be correlated with the amount of DR stretching as measured by the DRT. Fig. 10 shows the DRT value, for all the methods except GLT, versus the $\mathrm{CR_{LC}}$ improvement compared to DAS. We observe that R^2-adj=0.88 (0.72 when including the GLT) for simulated data and R^2-adj=0.98 (0.98 when including the GLT) for experimental data. That indicates that CR enhancement in the tested algorithms may be merely due to DR stretching. The GLT curve was chosen to fit the experimental results, and this choice probably explains the lower R^2-adj for the simulated data.

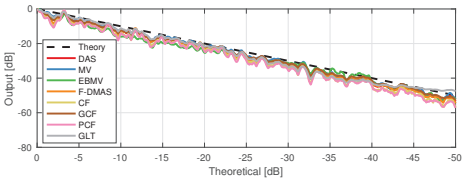

(a) Simulated lateral gradient after calibration

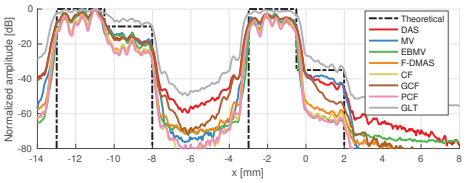

(b) Average lateral response through the speckle regions after calibration.

Fig. 11: The simulated lateral gradient after calibration is plotted in (a), (b) is the response through the speckle regions as in Fig. 8 but after calibration.

In [20] we suggested that DR transformations could be compensated by a calibration of the beamformed images, using the gradient response. In [20] we tested this approach on several algorithms and observed a dramatic reduction in CR improvement. However, even though known phantoms can be calibrated, adaptive beamformers can produce DR transformations that are dependent on the structures in the image. In other words, the DR transformation curve of an adaptive beamformer is often image-dependent: it can differ from patient to patient, from organ to organ, or even between areas of the same image. This is illustrated in Fig. 11. In Fig. 11a, the estimated gradient is shown for all methods after compensation, producing perfect linear slopes as expected. However, if we observe the intensity of the block along the depth $z = 30$ mm, in Fig. 11b, we see that the calibrated signals still differ from the theoretical for some of the methods.

This can be explained. The pixel intensity produced by coherent-based methods, such as CF, PCF, and GCF is highly dependant on the ratio of coherent to incoherent energy, which in turn depends on the slope of the gradient. In gradients that change slowly, along the lateral direction, this ratio will be larger than in gradients that change more abruptly. And hence, it becomes then impossible to find a single calibration curve for the whole image, and for the whole algorithm.

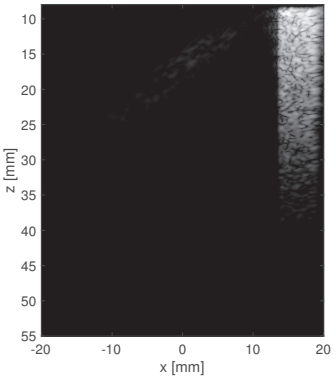

(a) DAS

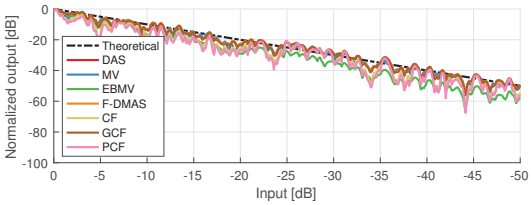

(b) Axial gradient

Fig. 12: The DAS image of the simulated phantom with all other elements of the phantom removed but the axial gradient in (a). In (b) the average response of the axial gradient, when only the axial gradient is present in the image, is plotted for all beamformers.

Consider the phantom in Fig. 12a where only the axial gradient is included. Fig. 12b shows the DR transformation curves for DAS, CF, GCF, F-DMAS, MV, EBMV, and PCF. Notice that, in this case, all beamformers leave the output DR almost unaltered. We must then conclude that it is the presence of the other structures, in the lateral direction, that induces DR stretching. Based on these two results we now believe, contrary to in [20], that compensating for that effect is extremely difficult, if not impossible.

Even though we cannot correct DR transformations it is important to be aware of its consequences. The images in Fig. 7 and 8 illustrated that DR stretching can lead to some information not being displayed, an information that could be clinically relevant. In most cases that information could be recovered if the image is displayed using a different dynamic scale, but that will also reduce the apparent visual contrast that seems to correlate with the increase in C and CNR values.

We showed that DR transformation makes any estimation of CR and CNR questionable, and given that some adaptive beamformers transform the output DR, it follows that claims on lesion detectability based on CR and CNR estimates should be revised. We have introduced datasets and code making it possible to investigate whether and how much a beamforming method is alternating the DR.

The results presented here expose a dangerous weakness of our image quality metrics. This weakness must be remediated.

We must lay the groundwork upon which we build the new techniques. A new metric for contrast must be sought, one that is immune to dynamic range transformations, and help us assess the relevance of present and future beamforming techniques.

VI. Conclusion

We propose a dynamic range test to estimate the output dynamic range of any beamforming algorithm. This test, comprising data and code, is made publicly available through the UltraSound ToolBox (USTB, http://www.USTB.no/dynamic_range_test/), allowing anyone to check if an algorithm transforms the output DR of the beamformed images.

We applied the proposed test to several state-of-the-art algorithms: DAS, MV, EBMV, F-DMAS, CF, GCF and PCF. We show that some state-of-the-art beamformers alter the DR either by compressing it, by stretching it, or by a combination of both. The amount of dynamic range alteration, as measured by the dynamic range test, correlates the CR improvement with R^2-adj=0.88 for the simulated data and R^2-adj=0.98 for the experimental data.

Our results show that improvements in CR and CNR can, for some beamformers, be explained by a stretching of the dynamic range. Thus, claims on lesion detectability based on the CR and CNR metrics should be revised, and metrics immune to dynamic range alterations should be sought.

Acknowledgment

This research was supported by the Center for Innovative Ultrasound Solutions (CIUS) and the Research Council of Norway, Project Code 237887.

References

[1] F. Bryn, "Optimum Signal Processing of Three-Dimensional Arrays Operating on Gaussian Signals and Noise," *The Journal of the Acoustical Society of America*, vol. 34, no. 3, pp. 289–297, 1962.

[2] B. Widrow, P. E. Mantey, L. J. Griffiths, and B. B. Goode, "Adaptive antenna systems," *Proceedings of the IEEE*, vol. 55, no. 12, pp. 2143–2159, 1967.

[3] S. Applebaum, "Adaptive arrays," *IEEE Transactions on Antennas and Propagation*, vol. 24, no. 5, pp. 585–598, Sep 1976.

[4] J. Capon, "Optimum weighting functions for the detection of sampled signals in noise," *IEEE Transactions on Information Theory*, vol. 10, no. 2, pp. 152–159, April 1964.

[5] S. W. Flax and M. O'Donnell, "Phase-aberration correction using signals from point reflectors and diffuse scatterers: basic principles," *IEEE Transactions on Ultrasonics, Ferroelectrics, and Frequency Control*, vol. 35, no. 6, pp. 758–767, Nov 1988.

[6] L. Nock, G. E. Trahey, and S. W. Smith, "Phase aberration correction in medical ultrasound using speckle brightness as a quality factor," *The Journal of the Acoustical Society of America*, vol. 85, no. 5, pp. 1819–1833, 1989.

[7] J. A. Mann and W. F. Walker, "A constrained adaptive beamformer for medical ultrasound: initial results," in *2002 IEEE Ultrasonics Symposium, 2002. Proceedings.*, vol. 2, Oct 2002, pp. 1807–1810 vol.2.

[8] M. Sasso and C. Cohen-Bacrie, "Medical Ultrasound Using The Fully Adaptive Beamformer," *IEEE International Conference on Acoustical Speech and Signal Processing, 2015. Proceedings (ICAASP 05).*, vol. 2, no. 4, pp. 489–492, 2005.

[9] F. Viola and W. Walker, "Adaptive signal processing in medical ultrasound beamforming," *Proceedings IEEE Ultrasonics Symposium*, vol. 4, no. c, pp. 1980–1983, 2005.

[10] Z. Wang, J. Li, and R. Wu, "Time-delay- And time-reversal-based robust Capon beamformers for ultrasound imaging," *IEEE Transactions on Medical Imaging*, vol. 24, no. 10, pp. 1308–1322, 2005.

[11] J. Synnevåg, A. Austeng, and S. Holm, "Minimum variance adaptive beamforming applied to medical ultrasound imaging," in *IEEE Ultrasonics Symposium, 2005.*, vol. 2, Sept 2005, pp. 1199–1202.

[12] "Scopus document search results," https://www.scopus.com, accessed: 2018-02-21.

[13] N. Q. Nguyen and R. W. Prager, "A spatial coherence approach to minimum variance beamforming for plane-wave compounding," *IEEE Transactions on Ultrasonics, Ferroelectrics, and Frequency Control*, vol. PP, no. 99, pp. 1–1, 2018.

[14] J. Zhao, Y. Wang, J. Yu, W. Guo, S. Zhang, and S. Aliabadi, "Short-lag spatial coherence ultrasound imaging with adaptive synthetic transmit aperture focusing," *Ultrasonic Imaging*, vol. 39, no. 4, pp. 224–239, 2017, pMID: 28068874.

[15] B. Zhuang, R. Rohling, and P. Abolmaesumi, "Accumulated angle factor-based beamforming to improve the visualization of spinal structures in ultrasound images," *IEEE Transactions on Ultrasonics, Ferroelectrics, and Frequency Control*, vol. 65, no. 2, pp. 210–222, 2018.

[16] J. Shin and L. Huang, "Spatial prediction filtering of acoustic clutter and random noise in medical ultrasound imaging," *IEEE Transactions on Medical Imaging*, vol. 36, no. 2, pp. 396–406, 2017.

[17] E. Ozkan, V. Vishnevsky, and O. Goksel, "Inverse problem of ultrasound beamforming with sparsity constraints and regularization," *IEEE Transactions on Ultrasonics, Ferroelectrics, and Frequency Control*, vol. PP, no. 99, pp. 1–1, 2018.

[18] T. Szasz, A. Basarab, and D. Kouam, "Beamforming through regularized inverse problems in ultrasound medical imaging," *IEEE Transactions on Ultrasonics, Ferroelectrics, and Frequency Control*, vol. 63, no. 12, pp. 2031–2044, 2016.

[19] S. W. Smith, R. F. Wagner, J. M. Sandrik, and H. Lopez, "Low Contrast Detectability and Contrast/Detail Analysis in Medical Ultrasound," *IEEE Transactions on Sonics and Ultrasonics*, vol. 30, no. 3, pp. 164–173, 1983.

[20] O. M. H. Rindal, A. Austeng, H. Torp, S. Holm, and A. Rodriguez-Molares, "The dynamic range of adaptive beamformers," *IEEE International Ultrasonics Symposium, IUS*, no. 1, pp. 1–4, 2016.

[21] J.-F. Synnevåg, A. Austeng, and S. Holm, "Benefits of minimum-variance beamforming in medical ultrasound imaging," *Ultrasonics, Ferroelectrics and Frequency Control, IEEE Transactions on*, vol. 56, no. 9, pp. 1868–1879, 2009.

[22] B. M. Asl and A. Mahloojifar, "Eigenspace-based minimum variance beamforming applied to medical ultrasound imaging," *IEEE Transactions on Ultrasonics, Ferroelectrics, and Frequency Control*, vol. 57, no. 11, pp. 2381–2390, 2010.

[23] G. Matrone, A. S. Savoia, and G. Magenes, "The Delay Multiply and Sum Beamforming Algorithm in Ultrasound B-Mode Medical Imaging," *IEEE Transactions on Medical Imaging*, vol. 34, no. 4, pp. 940–949, 2015.

[24] R. Mallart and M. Fink, "Adaptive focusing in scattering media through sound-speed inhomogeneities: The van Cittert Zernike approach and focusing criterion," *The Journal of the Acoustical Society of America*, vol. 96, no. 6, p. 3721, 1994.

[25] P. C. Li and M. L. Li, "Adaptive imaging using the generalized coherence factor," *IEEE Transactions on Ultrasonics, Ferroelectrics, and Frequency Control*, vol. 50, no. 2, pp. 128–141, 2003.

[26] J. Camacho, M. Parrilla, and C. Fritsch, "Phase coherence imaging," *IEEE Transactions on Ultrasonics, Ferroelectrics, and Frequency Control*, vol. 56, no. 5, pp. 958–974, 2009.

[27] M. A. Lediju, G. E. Trahey, B. C. Byram, and J. J. Dahl, "Short-lag spatial coherence of backscattered echoes: Imaging characteristics," *IEEE*

Transactions on Ultrasonics, Ferroelectrics, and Frequency Control, vol. 58, no. 7, pp. 1377–1388, 2011.

[28] S. Smith, H. Lopez, and W. Bodine, "Frequency independent ultrasound contrast-detail analysis," *Ultrasound in Medicine & Biology*, vol. 11, no. 3, pp. 467 – 477, 1985.

[29] M. Patterson and F. Foster, "The Improvement and quantitative assessment of b-mode images produced by an annular array/cone hybrid," *Ultrasonic Imaging*, no. 5, pp. 195–213, 1983.

[30] S. Mehdizadeh, A. Austeng, T. F. Johansen, and S. Holm, "Eigenspace based minimum variance beamforming applied to ultrasound imaging of acoustically hard tissues," *IEEE Transactions on Medical Imaging*, vol. 31, no. 10, pp. 1912–1921, 2012.

[31] S. Krishnan, K. W. Rigby, and M. O'Donnell, "Improved estimation of phase aberration profiles," *IEEE Transactions on Ultrasonics, Ferroelectrics, and Frequency Control*, vol. 44, no. 3, pp. 701–713, 1997.

[32] T. Szasz, A. Basarab, and D. Kouamé, "Strong reflector-based beamforming in ultrasound medical imaging," *Ultrasonics*, vol. 66, pp. 111–124, 2016.

[33] "Medical electrical equipment - Part 2-37: Particular requirements for the basic safety and essential performance of ultrasonic medical diagnostic and monitoring equipment," International Electrotechnical Commission, Geneva, CH, International Standard, Aug. 2007.

[34] J. A. Jensen and N. B. Svendsen, "Calculation of Pressure Fields from Arbitrarily Shaped, Apodized, and Excited Ultrasound Transducers," *IEEE Transactions on Ultrasonics, Ferroelectrics and Frequency Control*, vol. 39, no. 2, pp. 262–267, jan 1992.

[35] J. A. Jensen, "Field: A program for simulating ultrasound systems," *Medical & Biological Engineering & Computing*, vol. 34, pp. 351–353, 1996.

[36] O. M. H. Rindal. (2018) Achieving uniform field of view (fov) in synthetic aperture imaging (stai) in field ii simulations. [Online]. Available: http://www.ustb.no/examples/uniform-fov-in-field-ii-simulations/

[37] R. F. Wagner, M. F. Insana, and S. W. Smith, "Fundamental Correlation Lengths of Coherent Speckle in Medical Ultrasonic Images." *IEEE Transactions on Ultrasonics, Ferroelectrics, and Frequency Control*, vol. 35, no. 1, pp. 34–44, 1988.

[38] A. Rodriguez-Molares, O. M. H. Rindal, O. Bernard, A. Nair, M. A. L. Bell, H. Liebgott, A. Austeng, and L. Løvstakken, "The UltraSound ToolBox," *Ultrasonics Symposium (IUS), 2017 IEEE International*, pp. 1–4, 2017.

[39] J. P. Åsen, A. Austeng, and S. Holm, "Capon Beamforming and Moving Objects - An Analysis of Lateral Shift-Invariance," *IEEE Transactions on Ultrasonics, Ferroelectrics and Frequency Control*, vol. 61, no. 7, pp. 1152–1160, 2014.

[40] F. Prieur, O. M. H. Rindal, and A. Austeng, "Signal coherence and image amplitude with the filtered-delay-multiply-and-sum beamformer," *IEEE Transactions on Ultrasonics, Ferroelectrics, and Frequency Control*, pp. 1–1, 2018.

Ole Marius Hoel Rindal (S'14) was born in Hamar, Norway in 1990. He received the M.S degree in computer science (signal processing) in 2014 from the University of Oslo, Oslo, Norway. Since 2014 he has been working on his PhD at the University of Oslo, working with medical ultrasound beamforming techniques. He also holds a position at the Centre for Elite Sports Research, at the Norwegian University of Science and Technology, Trondheim, Norway, doing research on signal processing on inertial measurement units used in cross-country skiing. His research interest includes signal processing, medical image formation, image processing, machine learning, physiological and biomechanical aspects of cross-country skiing.

Andreas Austeng (S'97-M'01-SM'16) received the M.S. degree in physics and the Ph.D. degree in computer science from the University of Oslo, Oslo, Norway, in 1996 and in 2001, respectively. Since 2001 he has been working at the Department on Informatics, University of Oslo, as a Postdoctoral Research Fellow, an Associate Professor, and currently as a Professor with the Digital Signal Processing and Image Analysis Group. His research interests include signal processing for acoustical imaging and algorithms that aim to improve the quality of information extracted from images.

Ali Fatemi received his M.Sc. degree in Medical Technology in 2015 from the Norwegian University of Science and Technology (NTNU) with focus on ultrasound imaging. Since 2016 he has been Ph.D. candidate at the department of Circulation and Medical Imaging (ISB) of NTNU, researching on clutter generation mechanisms in cardiac ultrasound images and application of adaptive beamforming in cardiac ultrasound.

Alfonso Rodriguez-Molares received the M.Sc. degree in telecommunications and the Ph.D. degree in signal processing and communication from the University of Vigo, Vigo, Spain, in 2006 and 2011, respectively. He is Associate Professor and Senior Engineer with the Ultrasound Laboratory, Norwegian University of Science and Technology, Trondheim, Norway. He has coauthored over 15 papers in peer-reviewed journals, and holds two patents. His research interests include medical ultrasound, adaptive beamforming, acoustic propagation in heterogeneous media, and numerical acoustics.

Paper VIII

The Influence of Speckle Statistics on Contrast Metrics in Ultrasound Imaging

Stine M. Hverven, Ole Marius Hoel Rindal, Alfonso Rodriguez-Molares and Andreas Austeng

Published in *IEEE International Ultrasonics Symposium, IUS,* (2017), 1–4. doi: 10.1109/ULTSYM.2017.8091875

VIII

Paper IX

The Generalized Contrast-to-Noise ratio

Alfonso Rodriguez-Molares, Ole Marius Hoel Rindal, Jan D'hooge, Svein-Erik Måsøy, Andreas Austeng, Muyinatu A. Lediju Bell and Hans Torp

Manuscript prepared for submission to *IEEE Transactions on Ultrasonics, Ferroelectrics, and Frequency Control*, 1-12.

IX

Paper X

Hypothesis of Improved Visualization of Microstructures in the Interventricular Septum with Ultrasound and Adaptive Beamforming

Ole Marius Hoel Rindal, Svend Aakhus, Sverre Holm and Andreas Austeng

Published in *Ultrasound in Medicine and Biology,* (2017), 43 (10): 2494–2499.
doi: 10.1016/j.ultrasmedbio.2017.05.023.

Ultrasound in Med. & Biol., Vol. 43, No. 10, pp. 2494–2499, 2017

0301-5629/$ - see front matter

http://dx.doi.org/10.1016/j.ultrasmedbio.2017.05.023

● *Technical Note*

HYPOTHESIS OF IMPROVED VISUALIZATION OF MICROSTRUCTURES IN THE INTERVENTRICULAR SEPTUM WITH ULTRASOUND AND ADAPTIVE BEAMFORMING

Ole Marius Hoel Rindal,* Svend Aakhus,† Sverre Holm,* and Andreas Austeng*
* University of Oslo, Oslo, Norway; and † Norwegian University of Science and Technology, Trondheim, Norway

(*Received* 3 *March* 2017; *revised* 24 *May* 2017; *in final form* 27 *May* 2017)

Abstract—In this work, *in vivo* ultrasound cardiac images created with Capon's minimum variance adaptive beamformer are compared with images acquired with the conventional delay-and-sum beamformer. Specifically, we provide three views of a human heart imaged through the parasternal short-axis, the parasternal long-axis and the apical four-chamber views. The minimum variance beamformer produced images with improved lateral resolution, resulting in better resolved speckle structure and improved edges, especially on close investigation of the interventricular septum. These improvements in image quality might possibly improve the visualization of microstructures in the human heart. (E-mail: omrindal@ifi.uio.no) © **2017 World Federation for Ultrasound in Medicine & Biology.**

Key Words: **Minimum variance beamforming, Capon beamforming, Ultrasound imaging, Cardiac imaging.**

INTRODUCTION

B-Mode ultrasound imaging has seen significant improvements in image quality over the years. A major step up was the shift from analog to digital beamforming. A similar improvement was due to better transducers resulting in higher frequencies and larger bandwidths (Szabo 2014). More bandwidth led the way to yet another improvement with the introduction of tissue harmonic imaging (Kornbluth et al. 1998; Spencer et al. 1998).

Today, we are witnessing yet another step up in image quality resulting from increased computer power. It allows beamforming to be performed in flexible software implementations. Software beamforming has led to the breakthrough of ultrafast imaging (Montaldo et al. 2009). It also allows much more flexibility leading to manifold of new methods. Adaptive beamformers, in which the processing of the data adapts to the data recorded, have received much of the attention. Capon's minimum variance (MV) beamforming (Capon 1969) was one of the first such techniques to be applied to medical ultrasound by Mann and Walker (2002). The benefits of the MV beamformer are first and foremost improved lateral resolution (Synnevåg et al. 2009) and somewhat increased contrast (Rindal et al. 2014).

The computational load of the MV beamformer is orders of magnitude higher than that for conventional delay-and-sum (DAS) beamforming. However, Åsen et al. (2014) successfully demonstrated that the MV beamformer satisfies real-time processing requirements for a cardiac application when implemented on a graphical processing unit. The focus of their work was mainly on the implementation details; the image quality of the cardiac image was only briefly investigated.

In this work, our hypothesis is that the MV beamformer improves lateral resolution with possible improvements in visualization of microstructures in the human heart. We illustrate this by comparing *in vivo* images of a human heart obtained with MV and DAS beamforming. Different heart diseases alter the myocardial microstructures differently. For example, the microstructure of fibrosis in cardiomyopathies will differ from that in ischemic heart disease. Therefore, better visualization of cardiac microstructure may help the clinician to reach the correct diagnosis for a given patient.

In this article, we give a short introduction to the data acquisition and beamforming algorithms and then present three different views of the interventricular septum and discuss our findings.

Address correspondence to: Ole Marius Hoel Rindal, PB 1080 Blindern, 0316 Oslo, Norway. E-mail: omrindal@ifi.uio.no

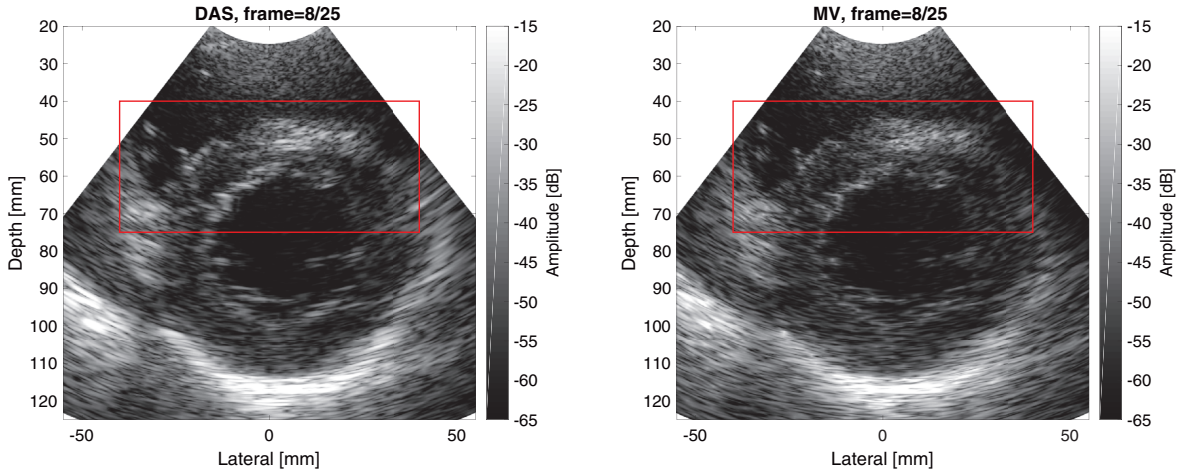

Fig. 1. Parasternal short-axis views obtained with delay-and-sum beamforming (DAS) and minimum variance beamforming (MV). The increased resolution in the MV image results in a better resolved speckle pattern, especially in the interventricular septum. Also, note the improved edge between the left ventricle and the interventricular septum. The *red box* denotes the zoomed-in region of the interventricular septum shown in Figure 2.

METHOD

Data acquisition

Channel data were acquired using the Verasonics Vantage 256 system (Verasonics, Kirkland, WA, USA) with the Verasonics P4-2v 64-element, 0.3-mm pitch, phased array probe transmitting with a center frequency at 3 MHz and sampled at four times the center frequency. Each image is created from 101 focused transmit beams, covering a sector scan from $-37.5°$ to $37.5°$. We reconstructed the images using the fundamental frequency. The transmit focus was placed at 52 mm for parasternal views and at 67 mm for the apical four-chamber view. We imaged the heart of a healthy volunteer from our laboratory, after written consent had been acquired.[1] The ultrasound images were acquired by a trained professional using the transthoracic technique with the subject positioned in left decubitus position. Images on the parasternal and apical imaging planes were obtained. The channel data were stored and the images were made with the beamforming in MATLAB (The MathWorks, Natick, MA, USA).

Delay-and-sum beamforming

In conventional DAS beamforming, every sample along a depth line sums up the delayed received signals from every element:

$$S_{\mathrm{DAS}}[z] = \sum_{m=0}^{M-1} w_m y_m[z] = \boldsymbol{w}^H \boldsymbol{Y}[z] \tag{1}$$

Here, M is the number of elements, z is every depth sample, y_m is the correctly delayed signal from element m, and w_m is a pre-defined weight. The delays are calculated as in von Ramm and Smith (1983). The matrix $\boldsymbol{Y}$ is a matrix consisting of the correctly delayed channel data, and $\boldsymbol{w}$ is the apodization. In this study, we used uniform

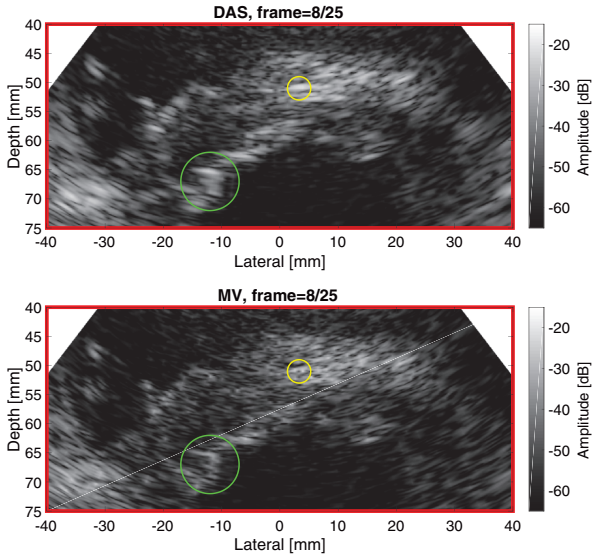

Fig. 2. Zoom of the interventricular septum in the parasternal short-axis view. The small (*yellow*) circle indicates a good example of improved lateral resolution in the minimum variance beamforming (MV) image compared to the delay-and-sum beamforming (DAS) image, whereas the larger (*green*) circle indicates an example of where the edge between the left ventricle and the interventricular septum has been improved.

[1] This study received a *Letter of Exemption* from the Regional Committee for Medical & Health Research Ethics in Norway with Institutional Review Board Reference No. IRB00001870 REK because they "found the Research Project to be outside the remit of the Act on Medical and Health Research (2008)."

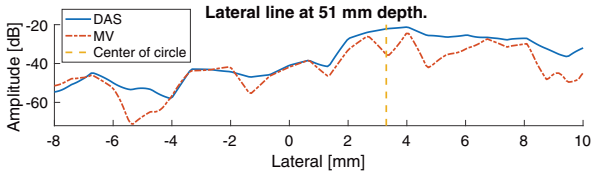

Fig. 3. Lateral line at 51-mm depth through the smaller (*yellow*) circle plotted in Figure 2. The plot illustrates the improved lateral resolution achieved by minimum variance beamforming (MV). The speckle blob in the delay-and-sum beamforming (DAS) image is clearly resolved into two scatterers.

apodization for DAS because this gives the best resolution.

Minimum variance beamforming

In Capon's MV beamforming technique (Capon 1969), we calculate a data-dependent weight set to use in the summation. The weight set is the one that minimizes the output power, but maintains gain equal to one in the steering direction;

$$\min_{\boldsymbol{w}} E\left\{|S[z]|^2\right\} = \boldsymbol{w}^H \boldsymbol{R} \boldsymbol{w} \tag{2}$$

$$\text{subject to } \boldsymbol{w}^H \boldsymbol{a} = 1 \tag{3}$$

The solution is

$$\boldsymbol{w} = \frac{\boldsymbol{R}^{-1}\boldsymbol{a}}{\boldsymbol{a}^H \boldsymbol{R}^{-1}\boldsymbol{a}}\,, \tag{4}$$

with steering vector $\boldsymbol{a} = \mathbf{1}$ because the data are already delayed. One weight set is calculated for every sample of every line in the image. The challenge is to estimate the spatial covariance matrix $\boldsymbol{R} \equiv E\{\boldsymbol{Y}\boldsymbol{Y}^H\}$. We use a robust implementation of Capon's MV beamformer as described by Synnevåg et al. (2009) with the following parameters: subarray size of $L = 32, 9$ ($K = 4$) depth samples for estimating the spatial covariance matrix $\boldsymbol{R}$, and a diagonal loading factor of $D = 1/100$.

Image creation

The beamforming is followed by magnitude squared envelope detection. Then we normalize the image to the maximum value from one of the frames in the same recorded view before the final logarithmic compression and scan conversion. The dynamic range is indicated next to the displayed image.

RESULTS

The results are presented as images made with both the DAS and the MV beamformers. Figure 1 and Supplementary Video S1 (online only, all supplementary videos available at http://dx.doi.org/10.1016/j.ultrasmedbio.2017.05.023) depict the parasternal short-axis view, with Figure 2 and Supplementary Video S2 zoomed in on the interventricular septum. The lateral line at 51-mm depth, at the center of the smallest (*yellow*) circle in Figure 2, is plotted in Figure 3. Figure 4 and Supplementary Video S3 depict the parasternal long-axis view, with Figure 5 and Supplementary Video S4 zoomed in on the interventricular septum. Figure 6 and Supplementary Video S5 are from the apical four-chamber view, with Figure 7 and Supplementary Video S6 zoomed in on the interventricular septum. Figure 8 and Supplementary Video S7 are zoomed in on the mitral valve. Note that the image of the mitral valve is from a different frame than that from which the images in Figures 6 and 7 are taken. Two different frames were chosen because one highlighted the difference in speckle structure in the interventricular septum, and the second

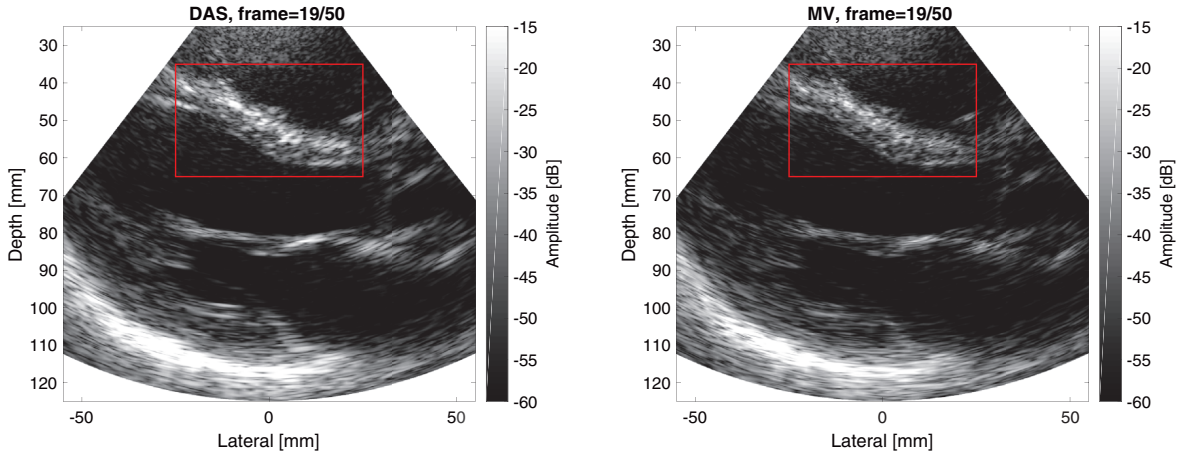

Fig. 4. Parasternal long-axis views obtained with delay-and-sum (DAS) and minimum variance (MV) beamforming, also illustrating improved resolution in the MV image by a better resolved speckle pattern. The *red box* denotes the zoomed-in region of the interventricular septum shown in Figure 5.

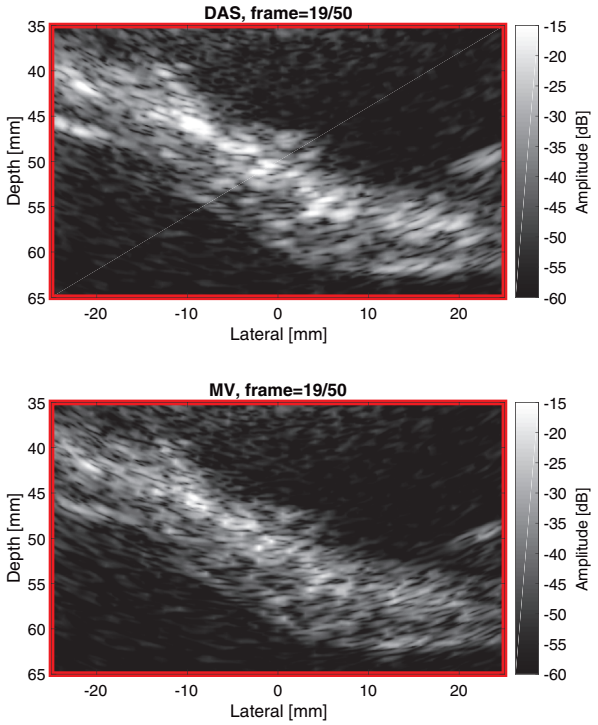

Fig. 5. Zoom of the interventricular septum in the parasternal long-axis view. The better resolved speckle pattern obtained with minimum variance beamforming (MV) compared to delay-and-sum beamforming (DAS) is especially seen in the interventricular septum.

highlighted the mitral valve's shape. The general observation from all the images shown, also indicated by the plotted lateral line in Figure 3, is that the MV beamformer exhibits superior lateral resolution compared with the DAS beamformer. These results are discussed in detail in the next section.

DISCUSSION

Our claim is that the MV beamformer produces images with improved lateral resolution resulting in a better resolved speckle structure and better defined edges. We support this claim by discussing and comparing images produced with both the DAS beamformer and the MV beamformer from three different views of a heart: parasternal short-axis, parasternal long-axis and apical four-chamber views.

When comparing the DAS and MV images from the parasternal short-axis view in Figure 1, we observe that the increased resolution of the MV beamformer results in a better resolved speckle structure, especially when closely investigating the zoomed in image of the interventricular septum in Figure 2. An example is highlighted with the smallest (*yellow*) circle at 51-mm depth and approximately 3-mm lateral position. When looking at the DAS image for this particular region, we see one large speckle blob. However, when looking at the MV image, we see that this large blob has been resolved into two separate scatterers. This is also illustrated by plotting the lateral line through this specific point in Figure 3. When comparing the DAS and MV lateral lines, we see that the MV beamformer has a dip of approximately 10 dB at a lateral position equal to 3 mm, resulting in the two separate scatterers shown in the image.

We also observe that the edge between the interventricular septum and the left ventricle, especially at depths from 62 to 72 mm and lateral positions from −17 to

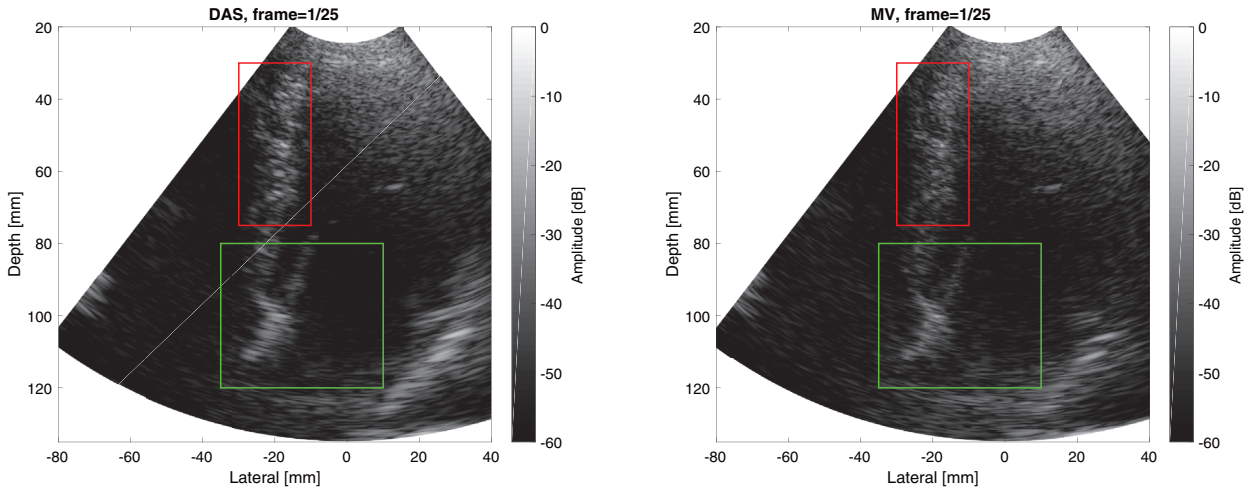

Fig. 6. Apical four-chamber view for both delay-and-sum (DAS) and minimum variance (MV) beamforming, where the improved lateral resolution of the MV beamformer is reflected by the better resolved speckle pattern and narrower mitral valve. The *red box* denotes the zoomed-in region of the interventricular septum shown in Figure 7, and the *green box* denotes the zoomed-in region of the mitral valve in Figure 8.

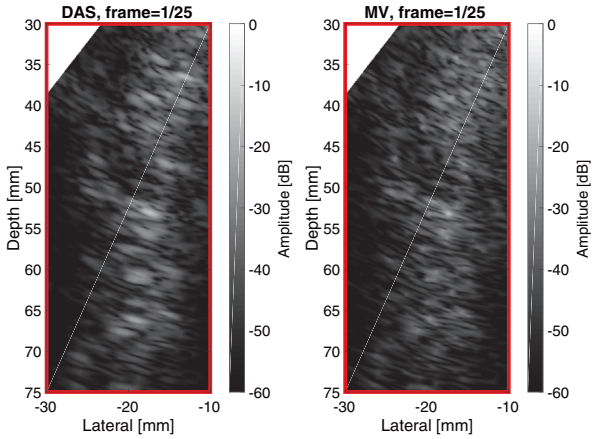

Fig. 7. Zoom of the interventricular septum in the apical four-chamber view highlighting the better resolved speckle structure obtained with minimum variance beamforming (MV) compared to delay-and-sum beamforming (DAS).

−7 mm, indicated by the largest (*green*) circle in Figure 2, is better resolved because the larger speckle blobs on the edge are resolved into smaller scatterers in the MV image. The improved edge is in agreement with the findings of Rindal et al. (2014). However, it is worth pointing out that the edge between the interventricular septum and the left ventricle does not seem to be improved in the MV image compared with the DAS image in Figure 8.

From the images of the parasternal long-axis view in Figure 4, we also observe that the MV beamformer gives a better resolved speckle structure. This is particularly clear when we investigate the speckle pattern in the interventricular septum, which is zoomed on in Figure 5.

Our final example is the apical four-chamber view in Figure 6, with the zoomed-in image of the interventricular septum in Figure 7. In the image, we once again observe that the MV beamformer gives a better resolved speckle structure in the interventricular septum. In Figure 8 is a zoomed-in image of the mitral valve. When investigating the valve, we see that both the valve and the septum are much narrower because of the improved lateral resolution. We also see the better resolved speckle structure, for example, resolving the large speckle blob in the DAS image at depth 106 mm and lateral position −20 mm into two scatterers in the MV image.

CONCLUSIONS

We used the MV beamforming technique on *in vivo* cardiac ultrasound data creating images from three different views of a heart: the parasternal short-axis, parasternal long-axis and apical four-chamber views. The images reveal that the improved resolution of the MV beamforming technique produces images with improved lateral resolution, resulting in a better resolved speckle structure compared with that of conventional DAS beamforming. Myocardial microstructure, that is, the architecture of cardiomyocytes, connective tissue fibers, blood vessels and neural tissue, contributes to the reflected ultrasound data. Further studies are needed to identify the efficiency of MV compared with DAS in terms of identifying pathological alterations in this microstructure.

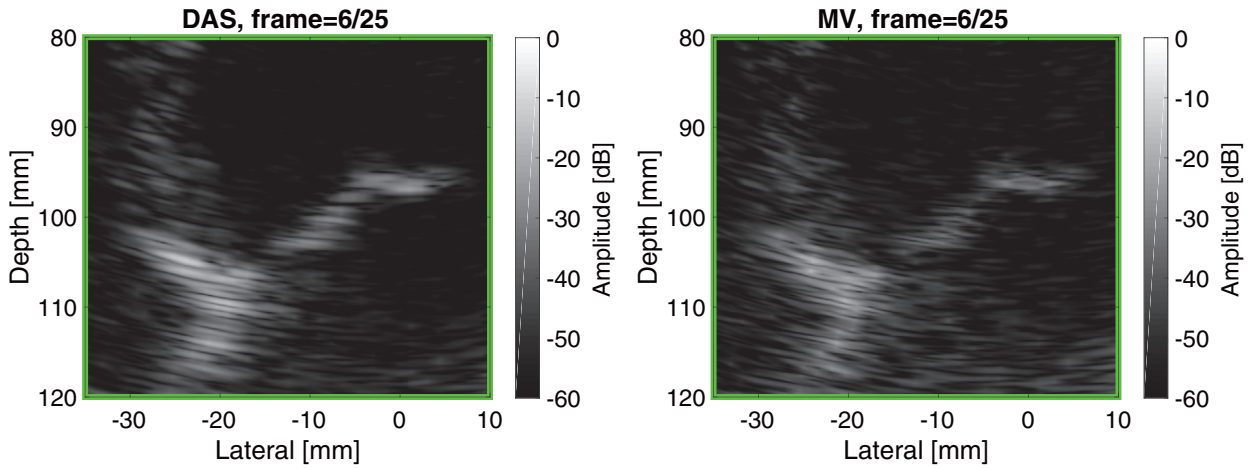

Fig. 8. Zoom of the mitral valve in the apical four-chamber view. Note that this is from a frame different from that for Figures 6 and 7. Both the valve and septum are narrower in the minimum-variance beamforming (MV) image because of the improved lateral resolution. Note also that the speckle blob in the delay-and-sum beamforming (DAS) image at depth 106 mm and lateral position −20 mm is resolved into two scatterers in the MV image.

SUPPLEMENTARY DATA

Supplementary data related to this article can be found at http://dx.doi.org/10.1016/j.ultrasmedbio.2017.05.023.

REFERENCES

Åsen JP, Buskenes JI, Nilsen CIC, Austeng A, Holm S. Implementing Capon beamforming on a GPU for real-time cardiac ultrasound imaging. IEEE Trans Ultrason Ferroelectr Freq Control 2014;61:76–85.

Capon J. High-resolution frequency-wavenumber spectrum analysis. Proc IEEE 1969;57:1408–1418.

Kornbluth M, Liang DH, Paloma A, Schnittger I. Native tissue harmonic imaging improves endocardial border definition and visualization of cardiac structures. J Am Soc Echocardiogr 1998;11:693–701.

Mann J, Walker W. A constrained adaptive beamformer for medical ultrasound: Initial results. Proc IEEE Int Ultrason Symp 2002;2:1807–1810.

Montaldo G, Tanter M, Bercoff J, Benech N, Fink M. Coherent plane-wave compounding for very high frame rate ultrasonography and transient elastography. IEEE Trans Ultrason Ferroelectr Freq Control 2009;56:489–506.

Rindal OMH, Åsen JP, Holm S, Austeng A. Understanding contrast improvements from Capon beamforming. Proc IEEE Int Ultrason Symp 2014;1694–1697.

Spencer KT, Bednarz J, Rafter PG, Korcarz C, Lang RM. Use of harmonic imaging without echocardiographic contrast to improve two-dimensional image quality. Am J Cardiol 1998;82:794–799.

Synnevåg JF, Austeng A, Holm S. Benefits of minimum-variance beamforming in medical ultrasound imaging. IEEE Trans Ultrason Ferroelectr Freq Control 2009;56:1868–1879.

Szabo TL. Diagnostic ultrasound imaging: Inside out. San Diego, CA: Academic Press; 2014.

von Ramm OT, Smith SW. Beam steering with linear arrays. IEEE Trans Biomed Eng 1983;30:438–452.

Appendices

Appendix A

Deriving the two-way resolution

The one way angular resolution at -6dB can be approximated by (Harris 1978)

$$\theta_{6dB} \approx \frac{1.21\lambda}{D}, \tag{A.1}$$

where D is the size of the full array aperture and λ is the wavelength.

We will now derive an expression for the two-way resolution. Assuming point sources and that the same sized array is used on both transmit (tx) and receive (rx). We know that the two-way beampattern can be calculated by taking the square of the one way beampattern (Johnson and Dugdeon 1993)

$$W_{\text{two way}} = W_{tx}W_{rx} = W^2_{\text{one way}}. \tag{A.2}$$

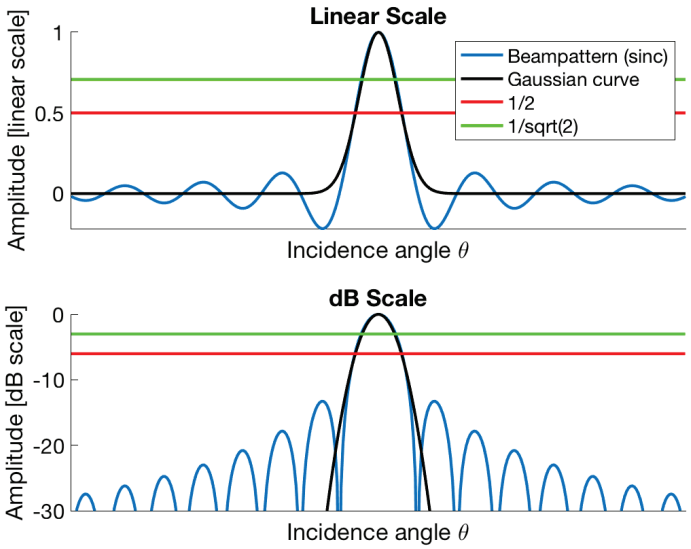

Figure A.1: The beampattern, a *sinc*, for some array with size D for some wavelength λ together with a Gaussian with zero mean and some standard variation σ. In the top we have plotted the beampattern and the Gaussian in linear scale, while we in the bottom have plotted them in dB scale. We have also indicated $1/2$ and $1/\sqrt{2}$ in the linear scale, resulting at ≈ -6dB and ≈ -3dB in the dB scale.

From Figure A.1, we see that the central part of the mainlobe of the beampattern can be approximated by a Gaussian curve. In Figure A.1 we have plotted the beampattern, a *sinc*, for some array with size D for some wavelength λ together with a normalized Gaussian with zero mean and some standard variation σ. In the top of Figure A.1 we have plotted the beampattern and the Gaussian

curve in linear scale, while we in the bottom have plotted them in dB scale. We have also indicated $1/2$ and $1/\sqrt{2}$ in the linear scale, resulting at ≈ -6dB and ≈ -3dB in the dB scale.

Using a normalized Gaussian curve we can find the half width, h, of the mainlobe at $\frac{1}{2}$ in linear scale (corresponding to -6dB) by

$$\begin{aligned} \frac{1}{2} &= e^{\frac{-h^2}{2\sigma^2}} \\ \ln\left(\frac{1}{2}\right) &= \frac{-h^2}{2\sigma^2} \\ &\Downarrow \\ h^2 &= -2\ln\left(\frac{1}{2}\right)\sigma^2 = 2\ln(2)\sigma^2. \end{aligned}$$

While at the $\frac{1}{\sqrt{2}}$ (corresponding to -3dB) we find the half width, g, of the mainlobe by

$$\frac{1}{\sqrt{2}} = e^{\frac{-g^2}{2\sigma^2}} \tag{A.3}$$

$$\ln\left(\frac{1}{\sqrt{2}}\right) = \frac{-g^2}{2\sigma^2} \tag{A.4}$$

$$\Downarrow \tag{A.5}$$

$$g^2 = -2\ln\left(\frac{1}{\sqrt{2}}\right)\sigma^2 = \ln(2)\sigma^2. \tag{A.6}$$

The g and h is only half the width of the mainlobe, and thus to get the full width we need to multiply with 2. The relationship between the θ_{-3dB} and θ_{-6dB}, but in linear scale, is then

$$\frac{2g}{2h} = \frac{2\sqrt{\ln(2)\sigma^2}}{2\sqrt{2\ln(2)\sigma^2}} = \frac{1}{\sqrt{2}}. \tag{A.7}$$

Finally, using that $W_{\text{two way}} = W^2_{\text{one way}}$, then $W_{\text{two way } 6dB} = W_{\text{one way } 3dB}$ as illustrated in Figure A.2.

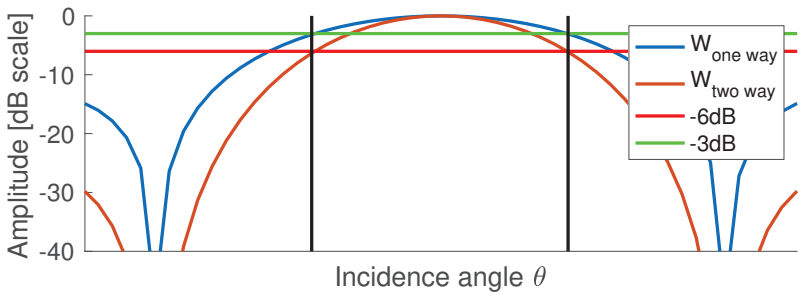

Figure A.2: The one-way and two-way beampattern plotted indicating that $W_{\text{two way } 6dB} = W_{\text{one way } 3dB}$.

We get

$$\theta_{6dB \text{ two way}} = \frac{1}{\sqrt{2}}\theta_{3dB \text{ one way}} = \frac{1}{\sqrt{2}}\frac{1.21\lambda}{D}, \tag{A.8}$$

and if we use a small angle approximation at depth z

$$x_{\text{res two way}} = \frac{1}{\sqrt{2}}x_{\text{res one way}} = \frac{1.21\lambda z}{\sqrt{2}D}. \tag{A.9}$$